STUDIA UNIVERSITATIS
BABEŞ-BOLYAI

SPECIAL ISSUE

EUROPEAN SCHOOL ON MAGNETISM

"New Magnetic Materials and their Functions"

and Workshop on advanced magnetic materials

September 9th - 18th 2007, Cluj-Napoca, Romania

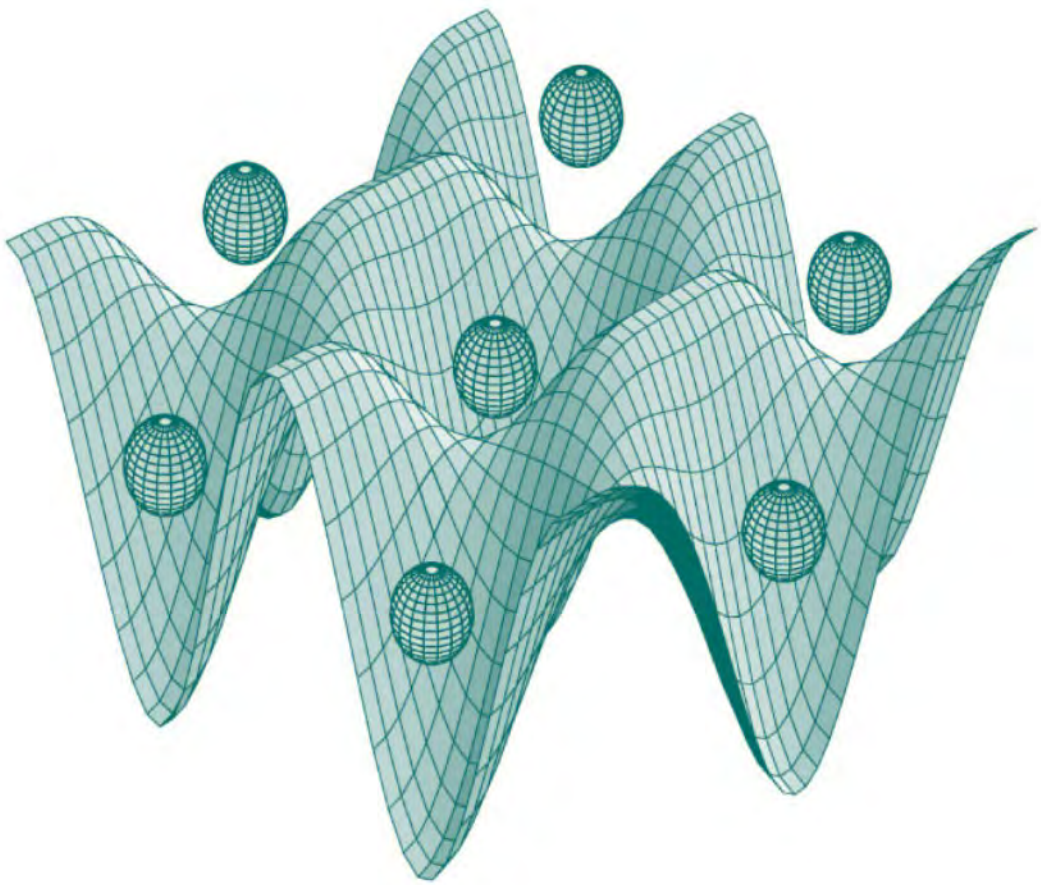

PHYSICA

1/2007

ESM

2007

European School on Magnetism

New Magnetic Materials and their Functions

September 9-18th 2007, Cluj-Napoca, Romania

Main Topics

Magnetism and transport properties, Soft and hard magnetic materials and their applications, magnetic recording, Nanoparticles, Multiferroic materials, Nanostructured materials Magnetisation processes and coercivity, Magnetocaloric effect and materials, Magnetostrictive effect and shape memory materials, Magnetic materials with special functions, Magneto-optic effect, Magneto-optic microscopy and materials, New topics in technologies and their applications, Magnetic Micro-Electro-Mechanical Systems, Giant Hall Effects and Hall effect, Exchange-bias, Giant Magneto Resistance, Tunnel Magneto Resistance

Workshop on advanced magnetic materials

Organisers

Babes-Bolyai University Cluj-Napoca

Université Joseph Fourier, Grenoble

CNRS, Grenoble

Institut National Polytechnique de Grenoble

CEA, Grenoble

Conference site: Babes-Bolyai University Cluj-Napoca, Romania

Registration deadline set: June 1st, 2007 ***http://esm.neel.cnrs.fr/***

Scientific Committee

M. Barandiaran (Bilbao, Spain)
E. Brück (Amsterdam, The Netherlands)
E. Burzo (Cluj-Napoca, Romania)
O. Cugat (Grenoble, France)
D. Givord (Grenoble, France)
O. Gutffleisch (Dresden, Germany)
R. Ibarra (Zaragoza, Spain)
O. Isnard (Grenoble, France)
W. Kappel (Bucharest, Romania)
J. Kirschner (MPI Halle, Germany)
A. Maziewski (Białystok, Poland)
D. Sander (Halle, Germany)
L. Schultz (IFW Dresden)
H. Szymczak (Warsow, Poland)
J. M. de Teresa (Zaragoza, Spain)
D. Stoeffler (Strasbourg, France)

Organising Committee

L. Buda-Prejbeanu (Grenoble, France)
E. Burzo (Cluj-Napoca, Romania)
E. Dorolti (Cluj-Napoca, Romania)
O. Isnard (Grenoble, France)
V. Pop (Cluj-Napoca, Romania)
R. Tetean (Cluj-Napoca, Romania)
J.C. Toussaint (Grenoble, France)

European Partners

MPI Halle Germany

IFW Dresden Germany

University of Saragossa, Spain

Academy of Sciences Warsaw, Poland

Van der Waals–Zeeman Instituut

Université Louis Pasteur Strasbourg, France

The organisers would like to acknowledge the financial and logistic support from the following institutions:

Babeş-Bolyai University Cluj-Napoca, România

Université Joseph Fourier, Grenoble, France

Centre National de la Recherche Scientifique, Grenoble

Institut National Polytechnique de Grenoble

Commissariat à l'Energie Atomique, Grenoble

Romanian Ministry of Education and Research

Région Rhône-Alpes, France

Ambassade de France en Roumanie

Centre Culturel Français de Cluj-Napoca

IFW Dresden, Germany

MPI Halle, Germany

University of Saragossa, Spain

Academy of Sciences, Warsaw, Poland

Van der Waals–Zeeman Instituut, Universiteit van Amsterdam, The Netherlands

ANUL LII **2007**

S T U D I A

UNIVERSITATIS BABEŞ – BOLYAI

PHYSICA

1

Desktop Editing Office: 51ST B.P. Hasdeu, no. 24 Cluj-Napca, Romania, phone +40 264-40.53.52

CONTENT – SOMMAIRE – INHALT

I. INTRODUCTORY LECTURES

II. SOFT AND HARD MAGNETIC MATERIALS AND THEIR APPLICATIONS

III. NANOPARTICLES

IV. AROUND MAGNETIC RECORDING

V. MAGNETIC MATERIALS WITH SPECIAL FUNCTIONS

VI. ADVANCED MAGNETIC MATERIAL

PREFACE

Since the beginning of the 90s, several scientific and teaching collaborations have been engaged between French laboratories and Universities and Babeş-Bolyai University Cluj-Napoca, Romania. Physics is one of the fields in which common teaching and research activities were strongly developed. Many professors from French Universities (Université Joseph Fourier, de Grenoble, Institut National Polytechnique de Grenoble, Université Claude Bernard de Lyon, Université Louis Pasteur de Strasbourg, Université Paris 12, Université de Rouen, etc) have given lectures at Babeş-Bolyai University. In the frame of our collaboration, more than 50 Romanian students followed training courses as master or PhD students in these universities. On the other hand professors from Babeş-Bolyai University have performed teaching and research in French partners Universities. Furthermore several French students joined as trainees the Babeş-Bolyai University.

The scientific and didactic collaboration was reinforced by recurrent organisation, at every two years, of summer schools since 1997 (http://esm.neel.cnrs.fr). The topics were mainly in solid state physics and magnetism: *Nanomagnetism* (1997), *High performance permanent magnets* (1999), *Spectroscopic analysis* (2001), *Magnetism of nanoscopic systems and hybrid structures* (2003) and *New experimental approaches in magnetism* (2005). For the first schools the participants (professors and students) were mainly from Romania and France. Progressively the school was open for professors and students coming from other European universities. Beginning with 2003 summer school, besides of Babeş Bolyai University and Joseph Fourier University we had a lot of European partners (Germany, Spain, Poland, The Netherlands, France) and the French-Romanian summer school becomes **European School on Magnetism**.

The scientific theme of the 2007 school is "*New Magnetic Materials and their Functions*" with a satellite workshop concerning "*Advanced magnetic materials*". The extraordinary dynamic in the field of the magnetic materials imposes a constant effort in order to form and inform our students (the engineer and researcher for "tomorrow") in the elaboration, properties and the applications of new materials. So a large panorama will be given to the students on the actually and emergent themes of the research on the new magnetic materials from their functionality to the applications. The workshop symposium will give possibility to the senior scientist to present and discuss the new results in advanced magnetic materials. Particularly we have in mind both the fundamental (the deeply understanding of the physical phenomena) and the applicative researches (high performance permanent magnets, ultra soft magnetic materials, magnetocaloric materials, multiferroic materials, shape memory materials, magnetic materials with biological applications, magnetic captors, spin electronic, high density magnetic recording, etc).

Organising committee

STUDIA UNIVERSITATIS BABEŞ-BOLYAI, PHYSICA, LII, 1, 2007

FUNDAMENTAL PROPERTIES

EKKES BRÜCK*

As we know, electron states in atoms are characterized by 4 quantum numbers: n (=0, 1, ..), l (=0, 1, .., n-1), m_l (=-l ,-l+1, .., l) and m_s (=-1/2, +1/2).
The latter three determine the magnetic response to an applied magnetic field. In isolated atoms, the individual magnetic moments within one shell add up, according to Hund's rules, to the total magnetic moment of the shell, characterized by the quantum number J. For the 4f-shell this yields a reasonable description of the observed moments, even in the metallic state (local model).

In the absence of interaction the magnetization M of a material is given by the field derivative of Helmholtz free energy A.

$$M = -\left(\frac{\partial A}{\partial H}\right)_T = Ng\mu_B J \, \mathrm{B_J}(x) \tag{1}$$

where $x = g\mu_B JH/(kT)$ is known as Lande's-factor, μ_B is the Bohr magneton, k is the Boltzmann constant, H is the magnetic field, T is the absolute temperature, and N is the numbers of the magnetic moments and

$$\mathrm{B_J}(x) = \frac{2J+1}{2J}\coth\left(\frac{2J+1}{2J}x\right) - \frac{1}{2J}\coth\left(\frac{1}{2J}x\right)$$

is the Brillouin function that varies between 0 and 1 for x = 0 and x = ∞, respectively. When $x << 1$, Eq. (1) becomes the Curie law (Buschow et al. 2003),

$$M = \frac{CH}{T}, \tag{2}$$

where $C = Ng^2\mu_B^2 J(J+1)/3k$ is the Curie constant. This equation gives the well known inverse proportionality of the magnetic susceptibility χ = M/H.
When the argument of the Brillouin function is very large, thus either at low temperatures and or high magnetic field, the magnetization will saturate to the maximal value M_S

* Van der Waals–Zeeman Instituut, Universiteit van Amsterdam, Valckenierstr. 65, 1018 XE Amsterdam, The Netherlands

$$M_S = Ng\mu_B J \tag{3}$$

When the distance between magnetic moments is small, the Pauli exclusion principle, which states that two identical fermions may not have the same quantum states, results in interaction between magnetic moments. Heisenberg introduced a model to describe this exchange interaction on microscopic scale. The Heisenberg exchange Hamiltonian may be written in the form

$$H_{exch} = -\sum_{i<j} 2J_{ij}\mathbf{S}_i \cdot \mathbf{S}_j, \tag{4}$$

where the summation extends over all magnetic moment pairs in the crystal lattice. For positive values of the exchange constant J_{ij} one finds parallel alignment else antiparallel. Ferromagnetism is observed for positive exchange interactions below a critical temperature.

The exchange interaction can be described as effective field acting on the moments. This field is produced by the surrounding magnetic moments and called the molecular field. As the size of the surrounding moments is proportional to the magnetization, the molecular field H_m is written as

$$H_m = N_W M \tag{5}$$

with N_W the Weiss-field constant. This constant was already introduced in the early 20th century long before the development of quantum physics. The total magnetic field experienced by a magnetic material is thus the sum of the externally applied field H_0 and the internal field

$$H = H_0 + H_m \tag{6}$$

and equation 2 needs to be rewritten as

$$M = \frac{C}{T}(H_0 + N_W M). \tag{7}$$

Thus, in the presence of ferromagnetic interaction much lower fields are sufficient to saturate the magnetization. The magnetic susceptibility is given by

$$\chi = \frac{C}{T - N_W C} = \frac{C}{T - T_C}. \tag{8}$$

This is the Curie-Weiss law, where T_C is the Curie temperature. Below the Curie temperature spontaneous magnetization is observed. For most materials, the phase transition from the paramagnetic state to the ferromagnetic state is found to be of second order. This means that the temperature dependence of the first derivative of the free energy (S, M, V) is continuous and only the second derivative of the free energy (specific heat C_H, χ, thermal expansion α) is discontinuous.

In 3d-metals the adjacent atoms break the symmetry to an extent that the orbital quantum number is no longer a good quantum number. Moreover, hybridization leads to energy bands in which the spin quantum number S is best describing the properties (itinerant model). In this model, the value of S is no longer necessarily a whole number. In itinerant systems equations 1, 2, 3 and 8 also hold when we substitute J by S.

Magnetism in 3d metals is well described by the Stoner band model, that distinguishes spin up and spin down bands:

$$E_{\uparrow}(k) = E(k) - \frac{I_S n_{\uparrow}}{N}$$
$$E_{\downarrow}(k) = E(k) - \frac{I_S n_{\downarrow}}{N} \tag{9}$$

with I_S the Stoner parameter that describes the energy change due to electron spin correlations. Ferromagnetism occurs when the density of states at the Fermi level $D(E_F)$ is exceeding some critical value which is expressed by the Stoner condition

$$\tilde{D}(E_F) I_s > 1 \tag{10}$$

where $\tilde{D}(E_F)$ is the normalized density per spin and volume.
N.B. Exchange energy in 3d metals ≈ 30meV

REFERENCES

Buschow, K. H. J. and F. R. de Boer (2003). "Physics of Magnetism and Magnetic Materials." New York, Kluwer Academic / Plenum Publishers

STUDIA UNIVERSITATIS BABEŞ-BOLYAI, PHYSICA, LII, 1, 2007

RARE EARTH-TRANSITION METAL COMPOUNDS: MAGNETISM AND APPLICATIONS

E. BURZO*

The rare-earth or yttrium (R) – transition metal (M) compounds form closely packed structures which may be regarded as arrangement of spheres having different dimensions. The necessity of maximum packing, taking into account geometrical and energetic restrictions, leads to an ordered arrangement, with well defined stoichiometry, in which the atoms are distributed on specific crystallographic sites. For example in Sm-Co series, Sm_3Co, Sm_9Co_4, $SmCo_2$, $SmCo_3$, Sm_2Co_7, $SmCo_5$ and Sm_2Co_{17} compounds, were reported. In the corresponding iron system only $SmFe_2$, $SmFe_3$ and Sm_2Fe_{17} were shown [1]. Ternary compounds, as example $R_2Fe_{14}B$ or $R_{n+1}Co_{3n+5}B_{2n}$, are also of interest. Substitutions at the rare-earth and transition metal sites are possible, in a certain amounts.

From magnetic point of view, when transition metals and R are magnetic, the magnetic moments of the two sublattices are parallely aligned, while in case of heavy rare-earths (Gd to Tm), there is an antiparallel coupling. From this general rule, there are exceptions as in cerium compounds. In case of $SmCo_5$, there is a change from ferromagnetic behaviour to a ferrimagnetic one as the temperature increase. Spin reorientations are frequently shown, characteristic for systems whose atoms have competing anisotropies (uniaxial and planar). The magnetic interactions between rare-earths and transition metals can be best described by 4f-5d-3d exchange path [2]. The 4f electrons of rare-earths (except Ce) have a small spatial extent and generally one can assume that they are well localized. On the other hand, the M metals show a wide spectrum of magnetic behaviours. This enclose well established magnetism in which the magnetic ordering temperatures are high, up to an exchange enhanced paramagnetism, crossing the situation in which ordered M moments collapse. Thus, the analysis of the magnetic behaviour of the R-M or R-M-B compounds can give very usefull information on the transition metals, whose magnetic properties are not well known. Thus, in first part we discuss the basic properties of these compounds, focusing mainly on the magnetic behaviour of M (M = Fe,Co,Ni) elements and then, their technical uses will be presented.

The exchange enhanced paramagnets as those based on $LaNi_5$, YNi_5, $LuCo_2$, YCo_2, at low temperatures, show on exchange enhanced paramagnetism. At $T > 10$ K, the magnetic susceptibilities χ, can be described by a T^2 dependence $\chi = \chi_0 (1+aT^2)$. At

* Faculty of Physics, Babes-Bolyai University Cluj-Napoca, Romania

temperatures higher than a characteristic value T*, the χ^{-1} vs T follows a Curie-Weiss behaviour, similar as in case of localized moments – Fig. 1 [3]. The XPS studies, at RT show the presence of holes in Ni3d band of $LaNi_5$-based compounds. The temperature dependences of the magnetic susceptibilities were analysed in $Y(Co,Ni)_2$ in the model of spin fluctuations [4], assuming a Gaussian distribution – Fig. 1 [3]. Replacing the nonmagnetic rare earth or yttrium by a magnetic R atom, in the above systems, a magnetic moment will be induced on Co or Ni atoms, beginning with a critical value of the exchange field [5] – Fig. 2. Then, the transition metal moments increase linearly with the exchange field and finally saturated, as shown for example in $R_{n+1}Co_{3n+5}B_{2n}$ system [6]. The same behaviour was seen in RCo_2-based compounds [5,7,8]. Band structure calculations performed on $Gd(Co,Ni)_2$ system showed, that in a good approximation, a local environment may describe the composition dependence of the transition metal moments in which Co moment is little modified if there is at least a critical number ($n_c = 3$) of atoms in a cluster. Values of $H_{cr} \cong 70$ T were estimated for transition from nonmagnetic to magnetic state of cobalt. In case of nickel, a value of $H_{cr} \cong 40(10)$ T was suggested [9]. The high field measurements on YCo_2 [10] evidenced the same type of transition [10]. Also, a linear dependence of the cobalt moment on the exchange field of $(3 \cdot 10^2)^{-1}$ μ_B/T was shown [11] and confirmed by high field measurements [12]. Iron shows a more localized behaviour. The dependence of the iron moment on the exchange field is of $(18 \cdot 10^2)^{-1}$ μ_B/T. As seen in Fig. 3, there is a rather good agreement between the computed values according to the above relation, and the variation of iron moments. The exchange splitting of M3d band is proportional to the exchange field.

The measurements made in a large temperature range, including the paramagnetic one show that are large difference in the ratio $r = S_p/S_o$, between the number of transition metals spin determined from Curie constants, S_p, and those obtained from saturation data S_o, as previously evidenced by the Rhodes-Wohlfarth curve. The ratio r, as function of reciprocal of exchange fields acting on M atoms, decreases as the exchange fields increase, approaching to r = 1, a value characteristic for a localized moment – Fig. 4. This behaviour can be analysed considering the effect of exchange field on M atoms as well as the partial quenching of spin fluctuation by exchange field.

The bands structure calculations showed that the R5d band polarizations can be described by a linear relation $M_{5d} = M_{5d}(0) + aG$ where G is De Gennes factor and $M_{5d}(0)$ is the value of R5d band polarization at G = 0. As example, in Fig. 5 are given the data obtained in RM_2 compounds. The first term, is due to short range exchange interactions of R atoms with the M ones situated in the first coordination shell, while the second is due to 4f-5d interactions. In compounds where there are lattice sites, having different environments, the $M_{5d}(0)$ is determined by the number of atoms (and their moments) situated in the first coordination shell – Fig. 6.

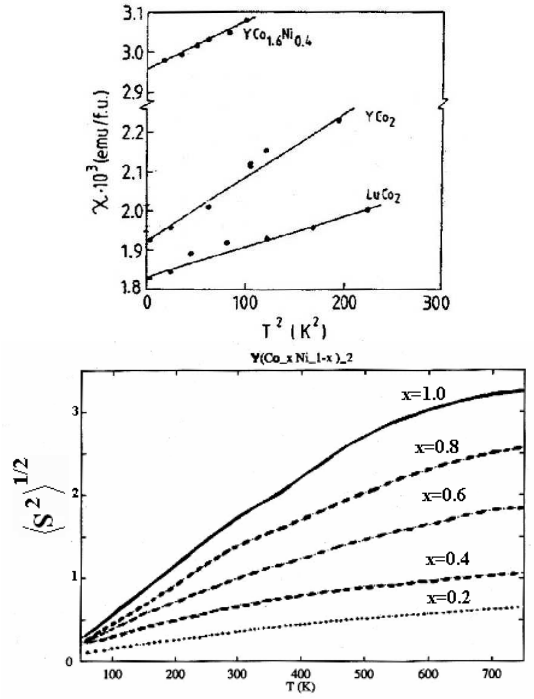

Fig. 1.

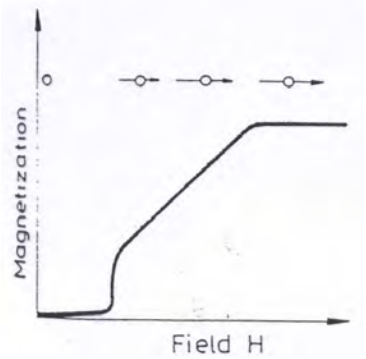

Fig. 2.

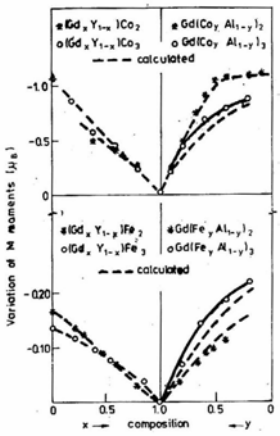

Fig. 3.

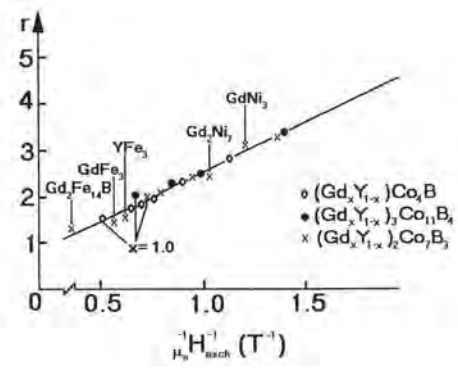

Fig. 4.

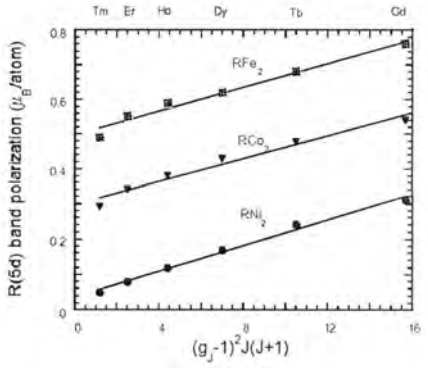

Fig. 5.

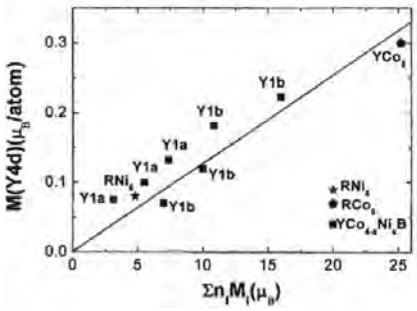

Fig. 6.

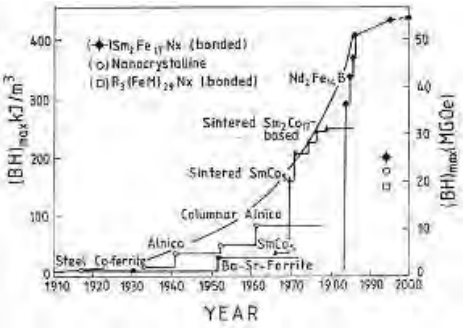

Fig. 7.

The rare-earth-transition metal compounds have interesting physical properties involving technical applications. Some of them will be surveyed:

Permanent magnets. The evolution of the maximum energy product in the last century showed an exponential increase, described by the relation (BH/max = 9.6 exp [(year-1910)/δ] with δ = 20 years – Fig. 7. The remarkable evolution has been determined by the use of R-M or R-M-B intermetallic compounds where R is generally a light rare-earth. The $SmCo_5$ and $Sm(Co,Fe,Zr,Cu)_7$ permanent magnets have a good thermal stability determined by their high Curie temperatures (T_c > 1000 K) [13]. Since both Sm and Co are expensive, the researches have been directed for development of cheaper permanent magnets, based on iron, as Nd-Fe-B [14]. Since of the low Curie temperatures, of $Nd_2Fe_{14}B$, hard magnetic phase, many studies were developed to improve their thermal stability, as alloying and

changing microstructure. The nanocomposite magnets based on Nd-Fe-B were also realized. These are formed from two magnetic phases one hard, as $Nd_2Fe_{14}B$ and another soft as α-Fe or Fe_3B [15]. The remanent induction and coercive fields of $Nd_5Fe_{70.5}Co_5M_1B_{18.5}$ nanocrystalline alloys are given in Fig. 8. Certain M additives, in combination with Co, significantly improves the squareness of the hysteresis loops and the intrinsic coercivity [16]. Nanocrystalline metastable alloys $SmFe_{9-y}Si_yC$ show also high coercive fields [17] – Fig. 9. The high coercivities of these samples originate from the P6/mmm type structure of the 1/9 metastable phases.

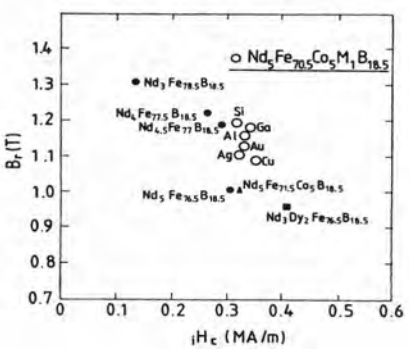

Fig. 8.

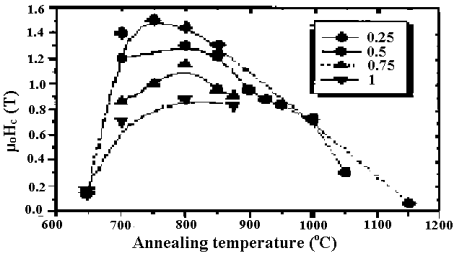

Fig. 9.

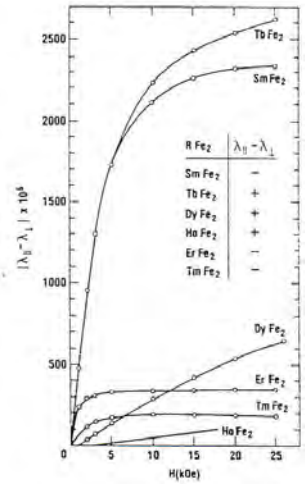

Fig. 10.

Magnetostrictive materials. The non-S state rare-earths al low temperatures, have high magnetostriction, λ. The λ value, at 4.2 K, are ≅ $9 \cdot 10^{-3}$ for Tb and $2.5 \cdot 10^{-3}$ for Ho. Since of low Curie temperatures of R metals, these cannot be used in magnetostrictive devices working at RT. In the RFe_2 Laves phase compounds, on the support of exchange interactions involving iron, the Curie temperatures increase up to 600-700 K. Thus, the large magnetostriction, characteristic to R metals at low temperatures, are translated at higher temperatures as shown in Fig. 10 [18].

Magnetocaloric materials. Magnetocaloric effect (MCE) has been evidenced in rare-earth compounds. Under adiabatic conditions, the change in magnetic entropy is compensated by an equal and inverse change in lattice entropy which causes a variation in the temperature of materials. A variety of intermetallic compounds were studied in order to achieve alloys having a large MCE, at RT, for magnetic refrigerators or at smaller temperatures for liquefaction of nitrogen, hydrogen or helium. The large MCE can be obtained for materials having large magnetic moment and also a sharp drop of the magnetization with increasing temperature, associated with the magnetic phase transition. Some examples are given in Fig. 11 [19].

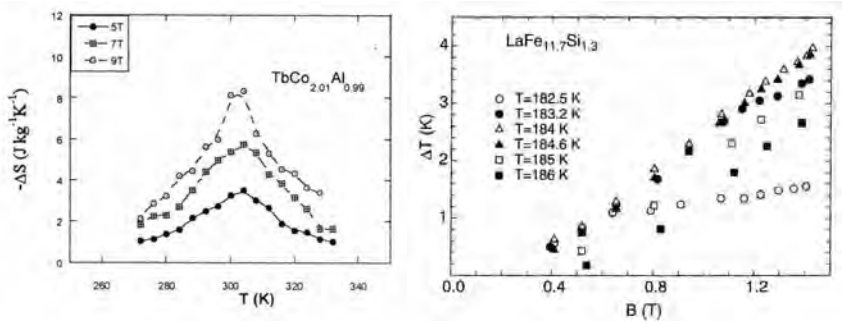

Fig. 11.

Hydrogen storage. Some intermetallic compounds can absorb a hugue hydrogen content as shown in Fig. 12, for $LaNi_5$. Pure $LaNi_5$ – shows an absorption plateau pressure of a few bars at ambient. There is a complete reversibility between formation and decomposition with a hysteresis between the corresponding equilibrium pressures. An α-phase solid solution precedes the β-$LaNi_5H_6$ hydride. The system requires an activation stage which involves decrepitation into small particles [20]. One of the most interesting use of intermetallic hydrides has been as a carrier of hydrogen fuel for motor vehicles.

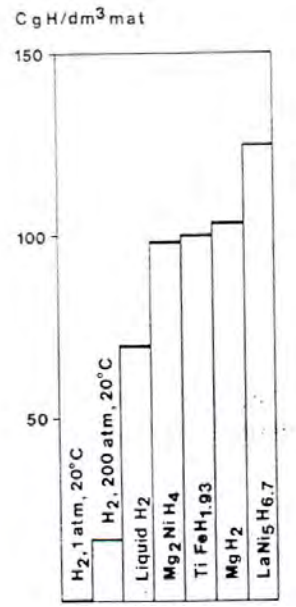

Fig. 12.

REFERENCES

1. E. Burzo, A. Chelkovski and H.R. Kirchmayr, Landolt Börnstein Handbuch, vol. III/19d2, Springer Verlag, 1990
2. I.A. Campbell, J. Phys. F: Metal Phys. 2, L97 (1972)
3. L. Chioncel, E. Burzo, R. Tetean and V. Pop, Mol. Cryst. Liquid Crystals 417, 513 (2004); E. Burzo, S. Chiuzbaian, M. Neumann, L. Chioncel, J. Phys. Condens. Matter 14, 8057 (2002)
4. T. Moriya, J. Magn. Magn. Mater 14, 1 (1979)
5. E. Burzo et al, Phys. Stat. Solidi (b) 65, K 145 (1974); Rev. Roum. Phys. 23,689 (1978); J. Less Common Met. 77, 251 (1981)
6. E. Burzo et al, Rev. Roum. Phys. 33, 57 (1988); J. Less Common Met. 155 281 (1989); J. Magn. Magn. Mater 140-144, 2013 (1995)
7. N.N. Duc et al, J. Magn. Magn. Mater 104-107, 1252 (1992)
8. E. Burzo and L. Chioncel, J. Opt. Adv. Mat. 6, 917 (2004)

9. E. Burzo, L. Chioncel, I. Costina, S. Chiuzbaian, J. Phys. Condens. Matter 14, 8057 (2002)
10. T. Goto et al, J. Magn. Magn. Mater 90-91, 700 (1991)
11. E. Burzo, Solid State Commun. 14, 1295 (1974)
12. N.P. Thuy, N.M. Hong, J.P. Liu, X. Li, J.J.M. Frause, F.R. de Boer, Physica B 177, 270 (1992)
13. K.J. Strnat, Handbok of Magnetic Materials, vol. 4 (1988), p. 131
14. M. Sagawa et al, J. Appl. Phys. 55, 2083 (1984)
15. E. Burzo, Rep. Progr. Phys. 61, 1099 (1998)
16. H. Kanekiyo, M. Uehara and S. Hirosawa, IEEE Trans. Magn. 29, 2863 (1993)
17. C. Djega-Mariadassou et al, Phys. Rev. B68, 024406 (2003)
18. A.E. Clark in Ferromagnetic Materials, vol. 1, Ed. E.P. Wohlfart, North Holland, 1980
19. A.M. Tishin, Handbook of Magnetic Materials, Esevier 1999, p. 395; R. Tetean, E. Burzo and I.G. Deac, J. Opt. Adv. Mat. 8, 501 (2006)
20. L. Shlapbach (Editor) Hydrogen in Intermetallic Compounds Springer Verlag, Topics in Applied Physics, vol. 63 and 64, 1992

STUDIA UNIVERSITATIS BABEŞ-BOLYAI, PHYSICA, LII, 1, 2007

SOFT MAGNETIC MATERIALS AND APPLICATIONS

OLIVIER GEOFFROY*

Fields of applications of prior importance for Magnetic Materials can be crudely distinguished as follows: Transformation of Energy, Actuation, Sensors (including Tags and RFID), Recording, … Operating materials are magnetically soft, hard, or characterised by coupling properties (transport properties, magnetostriction, magnetooptic, magnetocaloric, shape memory…). This brief presentation will focus on soft materials, other aspects being treated in dedicated topics.

Soft materials are used to drive the magnetic flux, to concentrate it in the air gaps, for shielding. The first point to be considered is the permeability μ, obeying the general formulation $1/\mu = 1/\mu_{qs}+1/\mu_{dyn}$. Different parameters act on the value μ_{qs} measured under quasi-static excitation or on its dynamical part μ_{dyn}. Related questions will be treated in parallel with the application fields.

1. Transformation of Energy at low frequency (f < 1 kHz)

The transformation of energy at low frequency (≈ 50 Hz) involves different kinds of sources, that is Mechanical ⇆ Electrical (Motors, actuators, generators) or Electrical ⇆ Electrical (transformers).

1 1. Mechanical ⇆ Electrical

The torque is the result of the interaction of the field produced by the moving part (rotor in a rotating machine) and the static part (stator). Fields can be produced by magnets or coils associated with soft magnetic materials. Scaling rules show that for little power (P ≈ 100 W) magnets are more powerful than coils, the coil generation more interesting for big machines.

Soft materials are used to reinforce in the air gap the fields generated by coils by the way of a mirror effect (the soft material forbids the penetration of the excitation field inside it and as a result reinforces H outside, that is inside the air gap). By this way the magnetic forces exerted are increased. The mirror effect is based on the assumption of high permeability, that is no magnetic saturation. This leads for machines big enough to the volumic maximum available torque

$\Gamma \approx J_s^2\, e/R$ $\quad J_s$ = Saturation Magnetization $\quad$ e = air gap $\quad$ R = Rotor radius

* Institut Néel, CNRS - Université Joseph Fourier, BP 166, 38042 Grenoble cedex 9, France

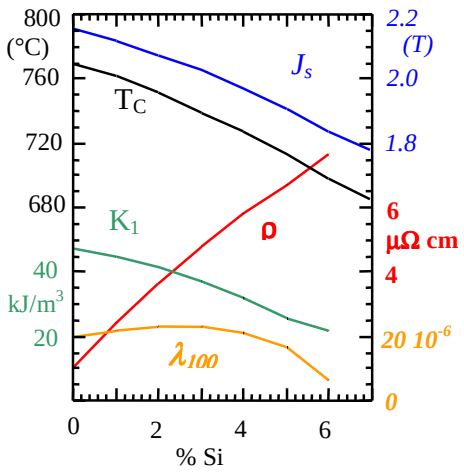

Fig. 1 . influence of Si content on the principal characteristics of FeSi alloys

➡ Need of Material featuring high J_s ➡ Use of **<u>iron based alloys</u>** (**J_{SFe} = 2,2 T**)
Classical design for rotating machines: cylindrical symmetry ➡ The fields are in the plane ⊥ to the axis ➡ The magnetic circuits are made of sheets stacked. The ideal sheet should exhibit planar or cubic texture (in practise, magnetization properties are more or less isotropic with **$\mu_r \approx 5000$**)

! Most of the magneto motive force being developed in the air gap, the relatively low μ of magnetic sheets is not critical.

! The stacked circuits offer the opportunity to control Iron losses due to eddy currents. Total Losses originating from mechanical friction and Joule effect in coils too, Iron contribution is thus of second importance and Electrical Insulation between sheets often simply obtained by superficial oxidation of sheets. The FeSi3% alloys (cf. Fig.1 the evolution of principal parameters with Si) correspond to the best grades (**$\rho_{Fe} = 10\ 10^{-8}\ \Omega m$, $\rho_{FeSi} = 48\ 10^{-8}\ \Omega m$**)

! Specific problem relating to Very Big machines (Production of energy: P > 1 GW): The high velocity (3000 trs/min for the rotor of a two poles machines, 50 Hz), coupled to a large diameter leads to high centrifugal forces. The mechanical resistance is achieved using high tensile strength steel (**R ≈ 550 GPa**) with Cr, Mo, Va, Mn additions to machine a massive rotor (static field in the rotor reference system ➡ no induced currents).

1 2The Electrical ⇆ Electrical conversion

The fields in the core transformer are unidirectional (cf. Fig.2)

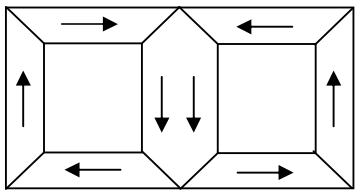

Figure 2. Flux directions in a core transformer

➡ Possibility to use **G**rain **O**riented **S**ilicon **S**teel sheets (see Fig.3) which offer an easy magnetization direction in the plane of the sheet and thus a great increase of permeability (μ_r **> 50 000**) compared to non oriented sheets ($\mu_r \approx 5000$).

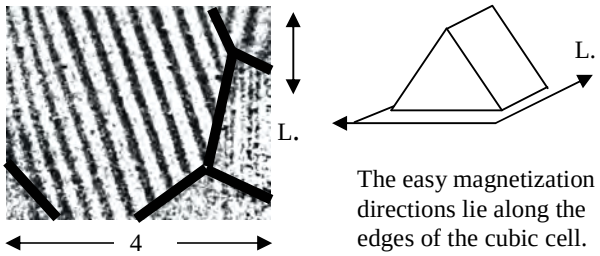

Figure 3. Magnetic domains in a FeSi GOSS imaged by Kerr Effect under a 9 MPa elongating stress and crystallographic orientation with respect to the lamination direction.

Optimization of dynamical Magnetization properties

Classical theory of eddy currents developed at a frequency f in the magnetic sheet of thickness e leads to choose $e \approx \delta = [\rho/(\mu\pi f)]^{1/2}$, where δ denotes the skin depth.

➡ $e_{50Hz} \approx 0.3$ mm, $e_{400Hz} \approx 100$ µm (400 Hz = operating frequency of in board electrical machines).

Classical volumic losses are thus obtained:

$$P_{vclas} / f = \lambda f \quad \lambda = \sigma B_m^2 e^2 \pi^2 / 6 \qquad (1)$$

! Taking into account the domain walls magnetization mechanism leads to the more accurate results:

$\mu_{dyn} = \frac{\pi^2}{16\ \ell\ e\ \sigma}\ \frac{1}{f}$ $P_v = 1{,}628\ P_{vclas}$ 2ℓ / e 2ℓ = width of a domain in the demagnetized state (2)

➡ An elongating stress ($\sigma \approx 10$ MPa) is applied by the mean of the isolating coating allows to eliminates additional unproductive local domains (spikes…), increasing the number of domain walls and improving thus the properties of dynamical Magnetization.

! Due to the great grain sizes ($\Phi \approx 1$ cm) featured by the best grades (Hi B FeSi), additional refining techniques (Laser scratching, Plasma grooving…) are involve to increase the number of domain walls.

! Adding Si to Fe to increase resistivity leads to brittle alloys. As a result, the minimum thicknesses obtained laminating $Si_{3\%}Fe$ are 50 or 100 μm, with a maximum operating frequency towards 400 Hz. Recently, commercial SiFe alloys featuring 6%Si have been proposed, the enrichment being obtained starting from conventional $Si_{3\%}Fe$ by Chemical Vapour Deposition. The main interest in the 6% amount Si is the vanishing λ_{100} and the increase of the resistivity (cf. Fig.1). Those points are of prior importance regarding the increase of the operating frequency in air-crafts electrical devices, especially concerning the problem of acoustic noise generated by in board transformers.

1 3. The Iron Cobalt alloys

The Iron Cobalt alloys are used instead of SiFe alloys when very high specifications are needed. Their main advantages are a large polarization ($\mathbf{J_{S\ FeCo25} = 2.4\ T}$) and a high Curie temperature ($\mathbf{T_{C\ FeCo94} = 1040\ °C}$) . Adding chromium and vanadium allows to reach resistivities to about $\mathbf{40\ 10^{-8}\ \Omega m}$ comparable to the FeSi one. Vanadium also reduces brittleness, allowing laminating until thickness ≈ 0.1 mm. The three main classes used for applications are $Fe_{74.5}Co_{25}Cr_{0.5}$ (noses of electromagnets), $Fe_{49}Co_{49}V_2$ (transformers and rotating machines), Fe_6Co_{94} (electromagnetic pumps for molten metals).

2. Electrical ⇆ Electrical conversion at medium and high frequencies (f > 400 Hz)

According to the skin depth criterion (cf. §112), the materials operating at higher frequencies have to feature higher resistivities or lower thicknesses than conventional SiFe alloys.

2 1. The Iron based amorphous ribbons (f < 100 kHz)

Amorphous magnetic soft alloys were introduced towards 1970. The Fe based alloys are the first member of the family of magnetically soft alloys obtained as ribbons by quenching. Co based amorphous and nanocrystalline alloys belong to the same family.

The elaboration requires glass formers (B, Hf…), leading to typical atomic composition $Fe_{81}B_{13.5}Si_{3.5}C_2$. In addition, very high cooling rate ($dT/dt > 10^6$ K/s) is needed to prevent crystallisation: This is achieved by the Planar flow casting process, where the liquid metal is falls on a rotative cooled cooper wheel (cf. topic dedicated to soft nanocristalline melt spun ribbons) . Ribbons of several centimetres width (until 20 cm) are obtained.
Ribbons are then annealed ($T_a \approx 400$ °C) to get ride of internal stress due to the quenching process.
The same elaboration process leads to some common characteristics featured by the all members of the family, that is

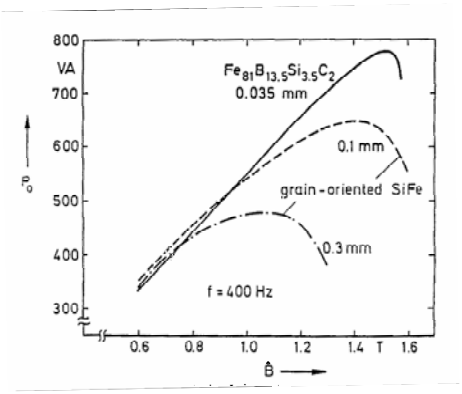

Figure 4. comparaison of the power featured by different transformers with wounded cores of same sizes made with different materials

* Operating Temperature ≈ **150 °C** limited by the Curie Temperature ($T_C \approx 300$ °C)
* Ribbon thickness **e ≈ 20-30 µm**
* Electrical resistivity **ρ ≈ 140 10^{-8} Ω**

} ➡ According to (2), good candidates for medium frequencies applications

A specificity of Fe based alloys is the high Polarisation induction **$J_S \approx 1{,}75$ T**. As a result, Fe based alloys can be compared to FeSi (**J_s = 2.06 T**) and, very attractive regarding losses, appear to be more interesting for transformers when the operating frequency increases (cf. Fig. 4). Depending on the annealing process, the density of domain walls can be varied and Fe based alloys can be used up to **100 kHz**. More expensive than the FeSi alloys, their use for low frequency (50-60 Hz) is until now restricted to regions characterised by a high cost of electrical energy (USA, Australia…)

2 2. The soft ferrites

The soft ferrites belong to two different families:

- The Spinels feature a cubic crystal structure type and a general formula MO, Fe_2O_3, M = divalent metallic ion (Mn^{2+}, Fe^{2+}, Ni^{2+}, Zn^{2+}, Mg^{2+}, Li^{2+}…). The small amount of magnetic ions and a ferrimagnetic coupling between neighbouring Fe^{3+} and M^{2+} leads to low Polarization induction (**$J_{SMn\text{-}Zn} \approx 0.5$ T**). In addition, indirect coupling of magnetic ions leads to low Curie temperatures (**$T_{CMn\text{-}Zn} \approx 240$ °C**)

The main interest of those compounds is their very high resistivity ($\rho_{MnZn} \approx$ **1-10 Ωm,** $\rho_{NiZn} \approx 10^5$ **Ωm**). This allows, starting from powder, to elaborate massive magnetic cores (moulding followed by sintering) operating up to **f = 1 MHz** for Mn-Zn and up to **f = 100 MHz** for Ni-Zn ferrites. This industrial process is very convenient for mass product, leading to very cheap cores.

- The ferrimagnetic garnets with the $Mn_3Al_2Si_3O_{12}$ structure and general formula ($5Fe_2O_3$ $3T_2O_3$) where T = rare earth element or Yttrium, Yttrium ferrite garnet commonly named YIG. The saturation polarization is lower than for spinels (**J_S < 0.2 T**) but their resistivity very high (until 10^{10} **Ωm**), the dissipative mechanism due to rotation damping of spins. As a result, ferrimagnetic garnets are extremely suitable for microwaves applications **(100 MHz < f < 100 GHz).**

3. Highest permeabilities and vanishing anisotropies alloys

The highest permeabilities are needed for applications such as magnetic shielding, low voltage circuits breakers (low frequency) or filtering. The quasi-static permeability is given by

$$\mu_{qs} \approx J_S / \sqrt{b + K_1 + K_u + 3/2\ \lambda\sigma} \qquad (3)$$

Where K_1 = magnetocristalline anisotropy, K_u = induced anisotropy, $3/2\ \lambda\sigma$ = magnetoelastic anisotropy (λ = magnetostriction, σ = stress supported). b corresponds to a magnetostatic energy associated to inhomogeneities. To obtain a high permeability (**μ_r > 300 000**), it is necessary first of all to control perfectly the metallurgical process to get ride of the b term, and secondly to minimize the various anisotropies in (3). Dealing with magnetoelastic effects, this implies $\lambda < 10^{-6.}$
Three kinds of materials fulfil the purpose in view, that is $Ni_{80}Fe_{15}Mo_5$ permalloys (**$J_S \approx$ 0.8 T**), Co based amorphous (**$J_S \approx$ 0.7 T**) and soft nanocristalline ribbons (**$J_S \approx$ 1.3 T**).

The vanishing K_1 is in Co based amorphous and soft nanocristalline ribbons a consequence of the structural disorder state, the vanishing λ obtained through composition (cf. topic dedicated to soft nanocristalline melt spun ribbons). One can notice that although its disorded state, Fe based amorphous do not belong to this family due to their high λ (**$\approx 30\ 10^{-6}$**)

Thought its crystalline state, it is possible to obtain vanishing K_1 in NiFe alloys by an accurate heat treatment (≈ 500 °C) which induces a short range order sufficient to bring K_1 to 0 for composition around 75% Ni. It is observed that λ_{100} and λ_{111} vanishes towards the same composition (cf. Fig. 5). Adding a small amount of Molybdenum allows to make λ_{100}, λ_{111} and K_1 vanish together. In addition, Mo increases ρ to 55 10^{-8} Ωm, which becomes comparable to ρ_{FeSi}.

Due to their higher Polarization saturation and low cost compared to permalloys and Co based amorphous, nanocristalline ribbons seem to be called to take a major part in the applications field.

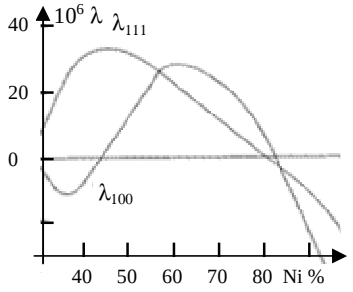

Fig. 5. evolution of λ_{100} and λ_{111} for NiFe alloys

4. Special hysteresis cycles and induced anisotropy

A very interesting characteristic featured by vanishing anisotropies alloys (cf. § 13) is the possibility to tailor the shape of the hysteresis cycle by the mean of induced anisotropy K_u. The shape is characterised by the ratio B_r/B_{max} (B_r = remanent induction). $B_r/B_{max} > 0.9$ => rectangular cycles; $B_r/B_{max} < 0.25$ => flat cycles.
Rectangular cycles alloys are obtained annealing the alloy under a longitudinal magnetic field (cf. fig.6 of topic dedicated to soft nanocristalline melt spun ribbons). they are of main interest for Magnetic amplifiers, fluxgates sensors…

Flat cycles alloys obtained by the means of K_u feature coherent rotation magnetization instead of domain walls displacements magnetization mechanism (cf. Fig.6). As a result, the coercitivity is nil and a nearly perfectly linear behaviour can be observed (cf. Fig.7). In addition, the dynamical behaviour is improved, leading to low losses and excellent quality factors, point of prior importance for filtering components. The way to induce K_u depends of the permeability needed:

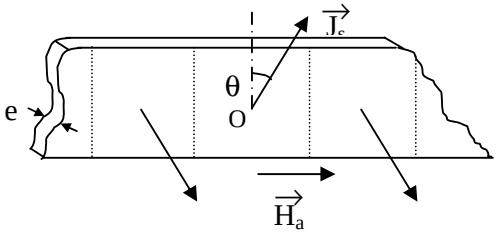

Figure 6. coherent magnetization rotation in a sample featuring transversal domains

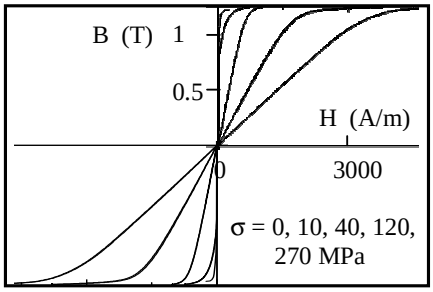

Figure 7. effect of an elongating stress applied during the cristallisation flash annealing on a soft nanocristalline alloy

- For unipolar electronics (pulse transformers, homopolar ground fault circuits breakers …), high permeabilities ($5\,000 < \mu_r < 100\,000$) are needed. With $\mu_r = J_S^2 / (2\,\mu_0\,K_u)$, such levels are obtained for $4 < K_u < 80$ J/m^3, annealing the alloy under a transverse magnetic field.
- For energy storage (Fly-back transformers …), lower permeabilities are needed. The range $200<\mu_r<1000$ is obtained annealing under elongating stress. The very low range $10<\mu_r<200$ is obtained by other ways.

5. Low permeabilities and composites

The way to obtain an apparent low permeability with a magnetic circuit made from a high permeability material is to make an airgap. The latter introduces radiation harmful for the neighbouring devices, and even more for the inductance coil the turns of which are located near the airgap, especially under high operating frequencies.

This can be avoided considering circuits made from compressed soft magnetic powders in a non magnetic matrix: the magnetic poles that appear at the particle/matrix interface warrant a weak relative permeability of the compressed material, so that the air gap is no more necessary. On the other hand, the particles being electrically insulated from each other (by the binder and if necessary by an insulating layer on the particles them-selves), iron alloys powder with high J_S can be used. Depending on the frequency range and permeability needed, commercial powders are made of iron, carbonyl iron, $Fe_{50}Ni_{50}$ or $Fe_{17}Ni_{81}Mo_2$. Recently, powders obtained by mechanical allowing have been studied (cf. dedicated topic).

STUDIA UNIVERSITATIS BABEŞ-BOLYAI, PHYSICA, LII, 1, 2007

COHERENT TRANSPORT AND SPIN EFFECTS IN QUANTUM DOTS

BOGDAN R. BUŁKA[*]

The lecture is a review of recent results on coherent electronic transport in quantum dots, especially on a role of the spin. In macroscopic metallic systems, an introduction of magnetic impurities leads to the Kondo effect, which is a spin-flip process of a localized spin at the impurity caused by resonant interactions with spins of conducting electrons [1]. In the last decade the Kondo effect has been intensively investigated in nanostructures [2-5]. Electronic transport in such the systems shows different features than those in the macroscopic system, where the characteristic feature is an increase of the resistivity with lowering a temperature. The effect is due to an increase of the relaxation time, an increase a role of spin-flip processes. In contrast in the quantum dot, the conductance increases and reaches the value $2e^2/h$ at T=0, which means that electrons are then perfectly transmitted [6].

After the introduction of the Kondo resonance, we will consider more complex systems of quantum dots (QD), where the Fano resonance can occur as well. The examples are presented in Fig. 1. The Fano resonance is a common quantum mechanical phenomenon and it is well known in various branches of condensed matter physics, as a special kind of interference process between a localized state and a subsystem of continuum of states. The combined Kondo-Fano effect was observed recently in transport through in various systems of QDs [7]. The experiments show that quantum interference and electronic correlations play a crucial role in transport. The first experiment showing quantum interference in nanoscale was on a metallic ring, where the Aharonov-Bohm effect was observed. Advanced lithography technology enables to produce metallic rings with QDs. In such the system, there is interplay between the phase shift of the electronic waves traversing the arms of the ring and that one caused y the Kondo effect.

[*] Institute of Molecular Physics, Polish Academy of Sciences, ul. M. Smoluchowskiego 17, 60-179 Poznań, Poland, *bulka@ifmpan.poznan.pl*

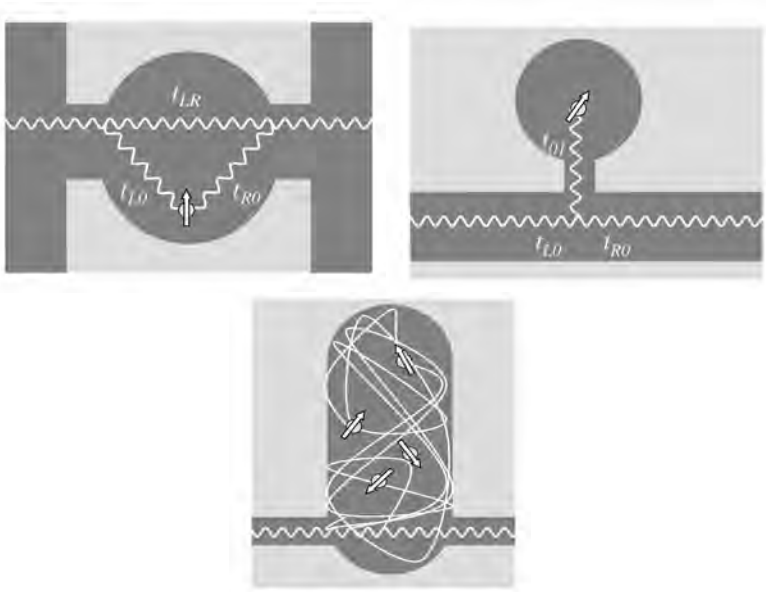

Fig. 1. Schematic presentation of a QD dot strongly coupled with electrodes (left), a side-attached QD (center) and a large QD with many scatterers (right). In all these systems the Kondo-Fano resonance was observed.

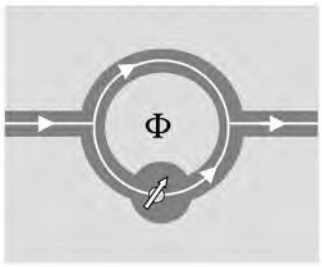

Fig. 2. Metallic ring with a quantum dot, in which the Aharonov-Bohm effect as well as the Kondo resonance can be observed.

We will present a theoretical description of electrical transport in these systems as well [8]. Only essential elements will be shown, technical details interesting for theorists one can find in references or/and discuss them later after the lecture.

In the second part of the lecture we consider the influence of accumulated electrons on the conductance through a two quantum dot (2QD) system. Such a system is the simplest realization of a qubit, an electronic device based on coherently coupled quantum dots. Much experimental effort has been undertaken to construct a 2QD connected with the source and drain electrodes either parallel [9] or in series [10]. The problem is more complex, because one can have two electrons and the single and triplet states have to be taken into account. A coherent coupling of these states with conducting electrons leads to the Kondo resonance [2] involving both the orbital and spin degrees of freedom of electrons [11]. The 2QD system can be considered as two Kondo impurities and described by the two impurity Anderson model [12, 13]. Depending on the relation of the inter-dot coupling J_{AF} to the dot–electrode coupling J_K, one can expect two different ground states. For the strong inter-dot coupling, the ground state is antiferromagnetic the singlet state formed by electrons at two neighboring quantum dots), while in the opposite case, for the strong coupling between the dots and the electrodes, two Kondo singlets are formed between conducting electrons and those localized at the dots [12]. There is a competition between the two configurations, which can be controlled by the interdot coupling. We will show theoretical studies of the transition between these states [14], the role of charge fluctuations and many body excitations, and their influence on the electronic transport.

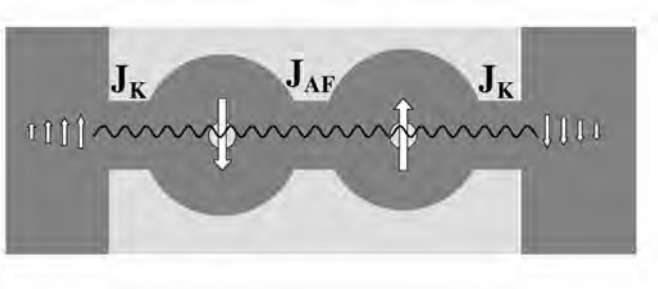

Fig. 3. System of two coupled quantum dots with competition between an antiferromagnetic ordering of the magnetic moments localized at the quantum dots and formation of the Kondo singlet (between the localized moments and spins of conducting electrons in the electrodes). Effective coupling parameters are denoted as J_{AF} and J_K.

Acknowledgements

The work was supported in part by Ministry of Science and Higher Education within a research project, as a part of ESF EUROCORES Programme FoNE by funds from Ministry of Science and Higher Education and EC 6FP (contract N. ERAS-CT-2003-980409), and EC project RTNNANO (contract N. MRTN-CT-2003-504574).

REFERENCES

1. C. Hewson, *The Kondo Problem to Heavy Fermions* (Cambridge University Press -1993)
2. L. Kouwenhoven and L. I. Glazman, Physics World 14, 33 (2001).
3. Goldhaber-Gordon et al., Phys. Rev. Lett. 81, 5225 (1998); D. C. Ralph and R. A. Buhrman, ibid. 72, 3401 (1994); S. M. Cronenwett et al., Science 281, 540 (1998); L. P. Rokhinson, et al., Phys. Rev. B 60, 16 319 (1999).
4. J. Nygard, D. H. Cobden, and P. E. Lindelof, Nature 408, 342 (2000).
5. W. J. Liang, et al., Nature 417, 725 (2002); J. Park, et al., Nature 417, 722 (2002).
6. L. I. Glazman and M. E. Raikh, JETP Lett. 47, 452 (1988); T. K. Ng and P. A. Lee, Phys. Rev. Lett. 61, 1768 (1988); A. Kawabata, J. Phys. Soc. Jpn. 60, 3222 (1991).
7. J. Gores, et al., Phys. Rev. B 62, 2188 (2000); M. Sato, et al., Phys. Rev. Lett. 95, 066801 (2005); A. C. Johnson, et al., Phys. Rev. Lett. **93,** 106803 (2004); K. Kobayashi, et al., Phys. Rev. B 68, 235304 (2003).
8. R. Bułka, P. and Stefański, Phys. Rev. Lett. 86, 5128 (2001); P. Stefański, Solid St. Commun. 128, 29 (2003); P. Stefański, A. Tagliacozzo, B. R. Bułka, Phys. Rev. Lett. 93, 186805 (2004); P. Stefański, A,Tagliacozzo, B. R. Bułka, Solid St. Comm. **135,** 314 (2005); B. R. Bułka, M. Ţolea, and I. V. Dinu, Phys. Rev. B **74**, 205301 (2006).
9. R. H. Blick, at al., Phys. Rev. Lett. **80** 4032 (1998); A. W. Holleitner, et al., Phys. Rev. Lett. **87,** 256802 (2001); A. W. Holleitner, et al., Science **297,** 70 (2002); M. C. Rogge, et al., 2003 Appl. Phys. Lett. **83,** 1163 (2003).
10. H. Jeong, et al., 2001 Science **293,** 2221 (2001); H. Qin, et al., Phys. Rev. B **64,** 241302 (2001); M. Pioro-Ladriere, et al., Phys. Rev. Lett. **91,** 026803 (2003); T. Hayashi, et al., Phys. Rev. Lett. **91,** 226804 (2003); R. H. Blick, et al., Physica E **16,** 76 (2003); M. Pustilnik, et al., Lecture Notes Phys. **579,** 3 (2001); J. R. Petta, et al., Phys. Rev. Lett. **93,** 186802 (2004); W. G. van der Wiel, et al., Rev. Mod. Phys. **75,** 1 (2003).
11. M. Pustilnik, et al., Phys. Rev. Lett. **84,** 1756(2000); M. Pustilnik and L. I. Glazman, Phys. Rev. Lett. **85,** 2993 (2000); Phys. Rev. Lett. **87,** 216601 (2001); Phys. Rev. B **64,** 045328 (2001).
12. W. Izumida, et al., 2001 Phys. Rev. Lett. **87,** 216803 (2001); O. Sakai and W. Izumida, Physica B **328,** 125 (2003).
13. K. Kawamura and T. Aono, Japan. J. Appl. Phys. 36, 3951 (1997); T. Aono, et al., J. Phys. Soc. Japan 67, 1860 (1998); Japan. J. Appl. Phys. 38, 315 (1999); T. Aono and M. Eto, Phys. Rev. B 63, 125327 (2001); R. Ziegler, et al., Phys. Rev. B 62, 1961 (2000); R. Aguado and D. C. Langreth, Phys. Rev. Lett. 85 1946 (2000); R. Lopez, et al., Phys. Rev. Lett. 89, 136802 (2002); P. A. Orellana, et al., Phys. Rev. B 65, 155317 (2002); R. Aguado and D. C. Langreth, Phys. Rev. B 67, 24530 (2003).
14. R. Bulka and T. Kostyrko, Phys. Rev. B 70, 205333 (2004); T. Kostyrko and B. R. Bulka, Phys. Rev. B 71, 235306 (2005); B. R. Bułka, T. Kostyrko, M. T. Tolea and I. V. Dinu, J. Phys. : CM 19, 255211 (2007).

STUDIA UNIVERSITATIS BABEŞ-BOLYAI, PHYSICA, LII, 1, 2007

APPLICATIONS OF HIGH ENERGY DENSITY PERMANENT MAGNETS

W. KAPPEL[*]

ABSTRACT. The permanent magnets have today many applications in the industry and are key components in devices of the electrical engineering, almost 75 % being used in motors, generators and actuators. The limit of the 10 billion Euros in the market of permanent magnets is surpassed in the year 2000 and the world market for permanent magnets will continue to grow strongly at 10 – 15 % annually. Powder technology is, and will remain, the preferred, and for some materials, the only method of hard permanent magnet preparation, and already accounts for over 80 % of the market [1].

The development of the rare earth magnetic materials (starting with 70's) has influenced significant and positively the application of the permanent magnetic materials owing to their large energy product and increased volume efficiency. Fastest growth will be in Nd-F-eB materials, the world production for will reach more than 39,110 t/year [2]. These are high performance magnets based on $Nd_2Fe_{14}B$ compound, whose performances exceeded that of the conventional permanent magnetic materials Alnico and hard ferrites, showing very high energy densities $(BH)_{max}$ of 145 to 400 kJ/m^3 (~ 18 to 50 MGOe) and coercivities over 24 kA/cm (~ 30 kOe).

Permanent magnet applications can be divided, generally, into four categories, as follows:

a. Applications that make use of the tractive and/or repelling force of the magnet, i.e., the attraction between a magnet and a soft magnetic material, such as a piece of iron or steel, or the attraction or repulsion between two magnets, is used to do mechanical work. The following applications are in this category:

- Magnetic separators, magnetic holding devices, such as magnetic latches;
- Magnetic torque drives;
- Magnetic bearing devices.

[*] R&D Institute for Electrical Engineering ICPE-Advanced Research Splaiul Unirii 313, sector 3, Bucharest, Romania
Phone: +40 021 – 346.72.31, fax: +40 021 – 346.82.991, e-mail: kappel@icpe-ca.ro

b. Applications that make use of the magnetic field of the magnet to convert mechanical energy to electrical energy:

- Magnetos;
- Generators and alternators;
- Eddy current brakes (used widely for watt-hour meter damping).

c. Applications that make use of the magnetic field of the magnet to convert electrical energy to mechanical energy:

- Motors;
- Meters;
- Loudspeakers;
- Relays;
- Actuators, linear and rotational.

d. Applications that use the magnetic field of the magnet to direct, shape and control electron or ion beams:

- Magnetic focused cathode – ray tubes;
- Traveling wave tubes
- Magnetrons;
- Ion pumps;
- Cyclotrons.

The purpose of a permanent magnet is to produce flux in the working gap of a device. Obviously, all permanent magnetic material will produce flux, but depending upon the working application, certain materials types, grades and shapes will be more efficient than others. The following is a breakdown by product applications that are most suitable for a material's characteristics:

- The key attributes of cast Alnico are: mechanically strong, cast to a variety of shapes, very temperature stable, can change magnetic orientation and high remanence B_r and magnetic energy $(BH)_{max}$ characteristics compared to ceramic materials.
- The key attributes of sintered Alnico are mechanically strongest of the Alnicos and close tolerances pressing/typically minimum grinding.

but both cast and sintered Alnico have low coercivity H_c when compared to ceramic or rare earth materials.

The general applications for both cast and sintered Alnico are:
Electron tubes, radar, traveling wave tubes;
Separators, holding magnets, coin acceptors, clutches and bearings;
Magnetos, motors, generators, meters, instruments, controls, relays, watt-hour meters (bearings and dampeners);
Automotive sensors, loudspeakers, cow magnets, distributors;
Communications, receivers, telephones, microphones.

Key attributes of the ferrite (ceramic) magnets are: economical high H_c and ${}_JH_c$ compared to Alnico. On the negative side, ceramics are good for simple shapes only, very fragile, require expensive tooling and temperature sensitive (0.2 %/^oC). Generally, the ferrite magnets are used in: d.c. permanent magnet motors used in the automobile industry for blowers, window lifts, windshield wipers, etc., separators to remove ferrous materials from liquid powder and bulk commodities, Magnetic Resonate Imaging (MRI), magnetos used on lawnmowers, outboard motors, DC brushless motors with controllers for speed and direction.

While being quite expensive, Sm-Co magnets are high H_C and ${}_JH_C$, high $(BH)_{max}$, very good temperatures ability and powerful for size, but, on the negative side, Sm-Co alloy is price sensitive, due to the Co supply and demand. Sm – Co is used in the traveling wave tubes, computer ring disc drives, d. c. motors (where temperature stability is vital, such as military use-satellite systems, small military motors), sensors, growing automotive applications and linear actuators.

Key reasons for using Nd-Fe-B permanent magnets are high energy for size, more economical than Sm-Co, good in ambient temperature situations, very high H_c and ${}_JH_c$ output, but, on the negative side of Nd-Fe-B permanent magnets are relatively high price, corrosion that can result in loss of energy and temperature coefficient of 0.13 %/degree centigrade. For the permanent magnets based on Nd-Fe-B alloys, some of the ever-growing list of uses is: linear actuators, speakers, microphone assemblies, magnetic separators, d.c. motors and automotive starters, servo-motors, hammer bank printers, computer rigid disc drives,

The further improvement of current magnetic materials relies on nanostructuring. Likewise, miniaturisation of MEMS requires materials having a high coercivity and remanence in order to maintain high force capability at reduced sizes. Promising candidates in both fields are rare earths magnets such as NdFeB and SmCo. When were prepared as thin films, the materials can be grown with complementary magnetic textures, NdFeB films typically possess a perpendicular magnetic anisotropy with the easy magnetic axis perpendicular to the substrate, whereas for SmCo films the easy axis commonly lies within the film plane. The NdFeB film permanent magnets are important for future advances in microsensors, micromotors and MEMS [3,4]. The miniaturisation of these microdevices requires magnetic thin films with high coercivity and remanent magnetization in order to provide strong forces [5].

REFERENCES

1. *** Powder Metallurgy Foresight Report: The PM industry in the UK – the next ten years, Institute of Materials, (2000) 15 - 30
2. Y. Luo, *Proc. of the 1st Workshop "Magnetism and Metallurgy*", Freiberg, Germany, (2006) 137 – 153
3. H. Kube, E. Saffert, A. Hoffmann, E. Kallenbach, Electrodynamic Linear Drive with Integrated Magnetic Bearing using thin Magnetic Layers, Vortrag MOVIC ´98, Proc. Fourth International Conference on Motion and Vibration Control, ETH Zürich, Schweiz, (1998)
4. H. Kube, V. Zöppig, R. Hermann, A. Hoffmann, E. Kallenbach, Electromagnetic miniactuators and microactuators using thin magnetic layers. Smart Materials and Structures, Proceedings of the 4th European and 2nd MIMR Conference, Harrogate, UK, (1998)
5. Jiang H. *et al., J. Magn. Magn. Mat*., (2001) 224-33

STUDIA UNIVERSITATIS BABEŞ-BOLYAI, PHYSICA, LII, 1, 2007

INFORMATION FROM MAGNETISATION CURVES

VIOREL POP*

The observation and the study of magnetic properties of substances and materials have been a subject of interest since the early days of human civilisation. Nowadays they aroused a huge interest from both fundamental and application point of view. The starting point in the study of magnetic materials can either be the theoretical speculations or the experimental measurements such as: magnetic curves, magnetic susceptibility, neutron diffraction, electron microscopy, spectroscopic studies, magneto-optic measurements, etc. The magnetic curves obtained in different types of magnetic materials, figure 1, represent one of the most used and convenient methods of characterisation in magnetic studies.

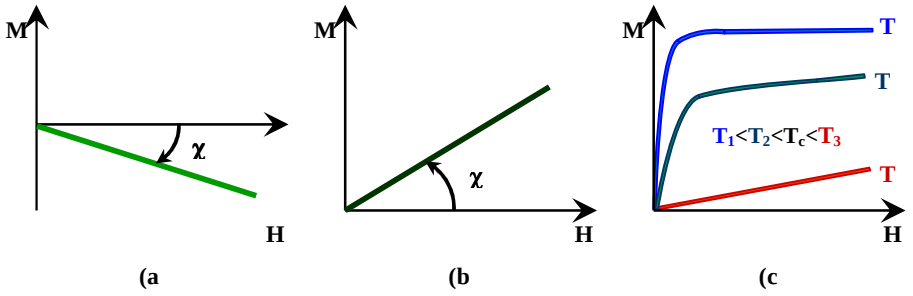

Figure 1. a) diamagnetic materials, b) paramagnetic materials, c) magnetically ordered (ferromagnetic or ferrimagnetic) materials.

We will present some of the scientific information which can be obtained from the study of magnetic curves. In the case of diamagnetic and paramagnetic materials, from the relation (1), the magnetic susceptibility, χ, can be obtained directly from the magnetisation curves, shown in figure 1.

$$\chi = \frac{M}{H} \tag{1}$$

where M is the magnetisation and H is the intensity of the magnetic field.

* Faculty of Physics, Babes-Bolyai University, 4000480 Cluj-Napoca, Romania

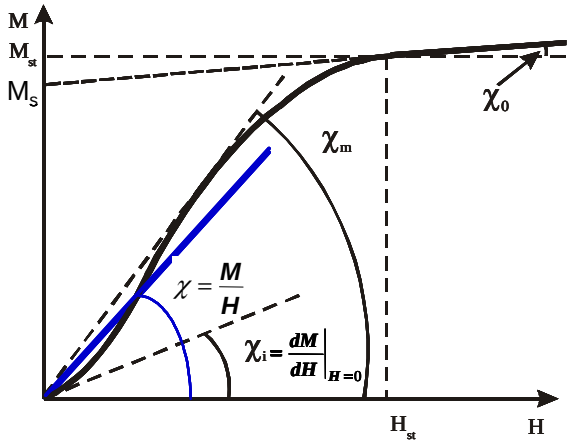

Figure 2. Magnetisation curve

In the case of paramagnetic materials, the Curie constant, *C*, can be obtained from the temperature dependence of the magnetic susceptibility, relations (2). By using (3) it is possible to determine the kinetic moment of the magnetic atoms.

$$\chi = \frac{C}{T} \tag{2}$$

$$C = \frac{N\mu_0}{3k_B} g^2 \mu_B^2 J(J+1) = \frac{N\mu_0}{3k_B} \mu ef^2 \tag{3}$$

where N is the number of magnetic atoms per volume unit, μ_0 is the vacuum permeability, g is known as the Lande factor, μ_B is the Bohr magneton, k_B is the Boltzmann constant and by μ_{eff} we denote the effective magnetic moment.
For ferromagnetic or ferrimagnetic materials, at temperatures smaller than the Curie temperature, T_c, the magnetic curves (figure 2) give information about the following: initial susceptibility χ_i, maximum susceptibility χ_m, field independent susceptibility χ_0, spontaneous magnetisation M_s, saturation field H_{st} and saturation magnetisation M_{st}.

As in the paramagnetic case, from the Curie Weiss (ferromagnetism) or the Néel type (ferrimagnetism) behaviours of magnetic susceptibility vs. temperature at $T>T_c$, we can obtain the effective magnetic moment and the kinetic moment of magnetic atoms, [1-8]. The remanence and coercivity can be studied from hysteresis curves, figure 3. Notice that the surface of the hysteresis loop is a measure of the magnetic energy stocked in to the hard magnetic materials or a measure of the hysteresis losses in soft magnetic materials.

In addition to χ_i, χ_m, χ_0, M_s, H_{st} and M_{st}, the first magnetisation curve, curve OABC in figure 3, gives information concerning the magnetisation processes: pinning or nucleation. Magnetisation curves measured in single crystals, figure 4, give information about the anisotropy: easy axis of magnetisation, anisotropy field, magnetic anisotropy, etc. The metamagnetic transitions can also be well evidenced in magnetisation curves [4]. Magnetisation curves are a very useful instrument of research in the domain of spring-type magnetic materials. The form of the magnetisation and demagnetisation curves contains information about the efficiency of the interphase exchange interactions. For this purpose, the reversibility curves can be used in tandem with the hysteresis curves, figure 5.

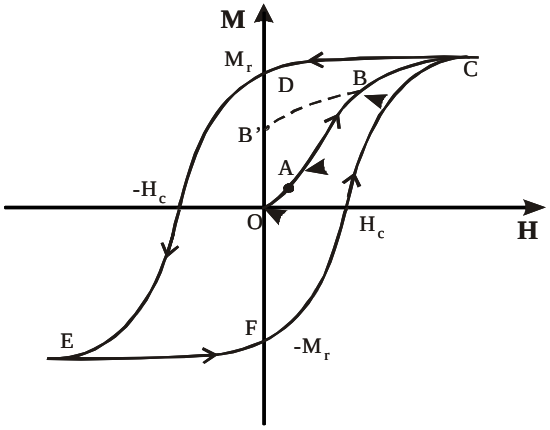

Figure 3. Hysteresis curve

Tacking into account the demagnetisation field, $H_d = - N_d M$ (N_d is the demagnetisation coefficient and M the magnetisation), the internal magnetic field in the measured sample is consequently, if $N_d \neq 0$, we have a smaller slope if we represent M vs. extern field, Ha, figure 6. This slope $\chi/(1+N_d \chi)$ is named external susceptibility [4]. Based on this fact the computation of the spontaneous magnetisation and of the anisotropy field in thin magnetic layers is shown in figure 7.

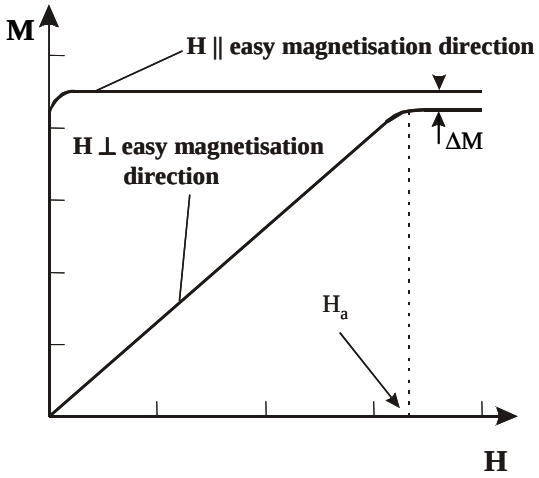

Figure 4. Magnetisation curves in single crystals

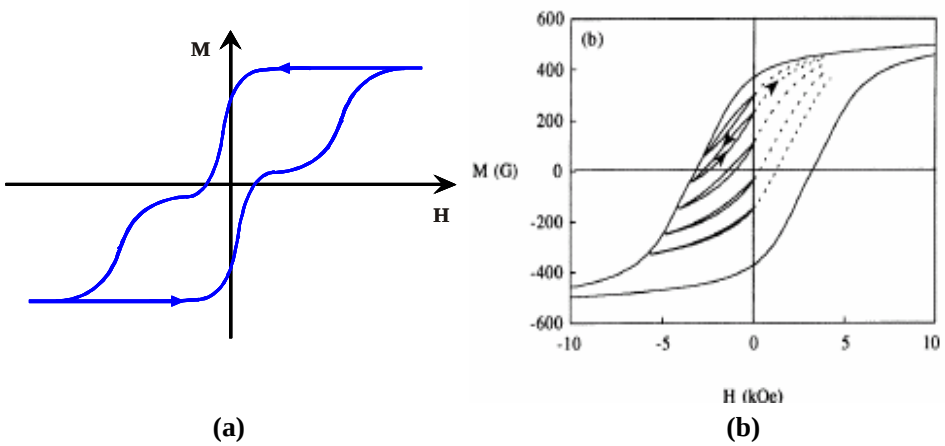

(a) **(b)**

Figure 5. (a) Major hysteresis loop for non coupled magnetic phases and **(b)** major hysteresis loop with a selection of minor re-magnetization curves (broken lines) and recoil loops for well coupled two-phase $Sm_2Fe_{14}Ga_3C_2$/40vol% -Fe [9].

$$\vec{H} = \vec{H}_a + \vec{H}_d \tag{4}$$

and

$$M = \chi \cdot H = \frac{\chi}{1 + N_d \chi} H_a \tag{5}$$

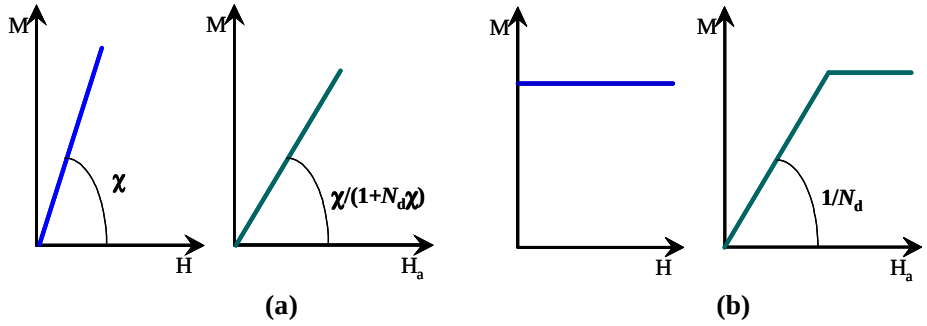

Figure 6. Magnetisation curves vs. external field H_a and internal field H for: **(a)** samples with a finite susceptibility and **(b)** samples with an infinite susceptibility (ideal ferromagnet) [4].

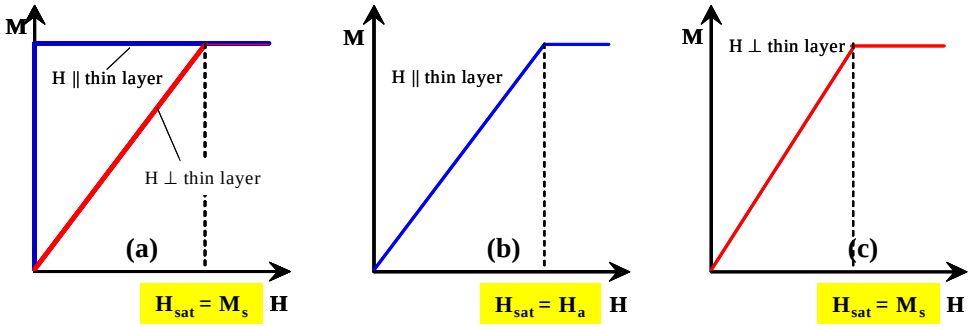

Figure 7. Typical magnetic curves in thin layers: **a)** M_s calculation in samples without magnetocrystalline anisotropy, **b)** and **c)** calculation of H_a and M_s respectively in samples with perpendicular magnetocrystalline anisotropy.

The paramagnetic or diamagnetic susceptibility in samples, with ferromagnetic impurities of concentration c and spontaneous magnetisation M_s, can be computed by the Honda-Oven plot, figure 8. The Arrott plot, figure 9, allows the evaluation of the Curie temperature in ferromagnetic or ferrimagnetic samples. The extended lecture to the school will developed the above examples and will ~~be~~ also taken into account other illustrations.

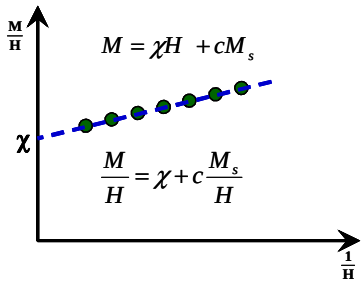

Figure 8. Honda Owen plot.

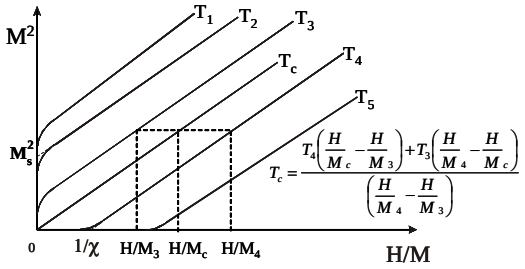

Figure 9. Arrott plot.

REFERENCES

1. Burzo E., Fizica fenomenelor magnetice, Ed. Academiei Române, Bucureşti, vol. I (1979), vol. II (1981), vol. III (1983).
2. Chikazumi S. (asistat de Charap S. H.), Physics of Magnetism, John Wiley & Sons, New York, 1964.
3. Herpin, Théorie du Magnetisme, Presses Universitaires de France, Paris, 1968 ,
4. De Lacheisserie E. (editor), Magnetisme, Presses Universitaires de Grenoble, 1999.
5. Morrish A. H., The Physical Principles of Magnetism, John Wiley &Sons, Inc.
6. Pop V., Chicinas I., Nicolae J., Fizica Materialelor. Metode experimentale, Presa Universitară Clujeană, 2001
7. Rado G. T., Suhl H., Magnetism, Academic Press, 1963.
8. Zijlstra, Experimental Methods in Magnetism, North Holand, Amsterdam, 1967
9. E. H. Feutrill, P. G. McCormick and R. Street, J. Phys.D: Appl. Phys. 29 (1996) 2320.

STUDIA UNIVERSITATIS BABEŞ-BOLYAI, PHYSICA, LII, 1, 2007

SOFT MAGNETIC NANOCRYSTALLINE/NANOSTRUCTURED MATERIALS PRODUCED BY MECHANICAL ALLOYING ROUTES

I. CHICINAŞ*

Materials whose crystallites/particle sizes are smaller than 100 nm are commonly named nanocrystalline/nanostructured/nanosized materials. The unique properties of nanocrystalline materials are derived from their large number of atoms residing in defect environments (grain boundaries, interfaces, interphases, triple junctions) compared to coarse-grained polycrystalline counterparts [1-3]. The benefits found in the nanocrystalline alloys stem from their chemical and structural variations on a nanoscale, which are important for developing optimal magnetic properties [1,2,4]. It is well known that the microstructure, especially the crystallite size, essentially determines the hysteresis loop of the soft ferromagnetic materials. The reduction of crystallite size to the dimensions of the domain wall width increases the coercivity towards an extreme value controlled by the anisotropy [5]. However, the lowest coercivity is found again for crystallite smaller than the correlation lengths like in amorphous and nanocrystalline alloys. Such behaviour has been explained by the random anisotropy model [6].

Besides the incipient crystallisation of amorphous solids [1-3], mechanical alloying is nowadays one of the widely used preparation techniques to obtain nanocrystalline structures. Mechanical alloying techniques involve the synthesis of materials by high-energy ball milling, in which elemental blends (or pre-alloyed powders, oxides, nitrides, etc) are milled to achieve alloys or composite materials [7–9]. These techniques allow producing non-equilibrium structures/microstructures including amorphous alloys, extended solid solutions, metastable crystalline phases, nanocrystalline materials and quasi crystals [9-15]. The disadvantage of ball-milling processes for making nanocrystalline powders is the contamination of products from the milling media (balls and vial) and atmosphere. In last two decades, a large variety of mechanical routes has been developed in order to produce nanocrystalline/amorphous alloys/intermetallic compounds.

Mechanical alloying (MA) refers especially to the formation of alloys/ compounds from elemental precursors during high-energy ball milling in planetary mills, vibratory mills, attritors and tumbling ball mills. The repeated collision between balls and powders with very high impact velocity deform and work-harden the

* Materials Sciences and Technology Dept., Technical University of Cluj-Napoca, 103-105 Muncii ave., 400641 Cluj-Napoca, Romania, Ionel.Chicinas@stm.utcluj.ro

powder. In this repetitive cold welding and fracturing mechanism, cold welding of overlapping particles occurs between clean surfaces formed by prior fractures. The competing process of deformation, fracture and welding during milling produces a microstructural refinement and finally some composition changes. In the case of the milling in planetary ball mil, depending of rotation speed of the disk on which the vial holders are fixed (Ω) and the rotation speed of the vial (ω), it has introduced the concept of the shock frequency, the kinetic shock energy and the shock power. According to Ω/ω ratio, it can have the shock mode process (SMP) when Ω » ω, and the friction mode processes (FMP), when Ω « ω [16, 17].

Mechanical milling (MM) refers to the process of milling pure metals or compounds which are in thermodynamically equilibrium before milling. This process can produce disorder, amorphous materials and composition changes. For MA and MM, the weight rate powder/balls is usually from 1/7 to 1/10, but can be found also rates from 1/5 up to 1/50. The materials obtained by mechanical alloying or mechanical milling present a high number of crystalline defects and it is possible to obtain amorphous alloys by mechanical alloying even for a negative energy for amorphous phase formation, by the way: $mA + nB \rightarrow A_mB_n$ *(crystalline)* $\rightarrow A_mB_n$ *(amorphous)* [9].

Mechanical alloying combined with annealing (MACA) is a new mechanical alloying technique which consists of mechanical alloying/milling and subsequent annealing. If the milling process is stopped before the MA finishing and then the milled powders mixture is subjected to an annealing it is possible to improve (finishing) the solid state reaction of compound/alloy forming [18, 19]. It is important to note the double effect of the annealing on the samples: (i) improvement of the solid-state reaction between elements and (ii) diminution of the internal stresses.

A new method of mechanical alloying consists in **MACA synthesis with inserting nanocrystalline germs** of the reaction product was proposed in [20]. Basically, the idea of the method consists in changing the solid state reaction of A_mB_n intermetallic compound synthesis from the classical form $mA + nB = A_mB_n$ to the form $(1-x)\cdot(mA + nB) + x\cdot A_mB_n = A_mB_n$. The effect is the reducing the milling time.

Reactive milling (RM) or mechanochemical synthesis (mechanochemistry) involves mechanical activation of solid state displacement reactions in a ball mill. Thus, mechanical energy is used to induce chemical reactions. Mechanochemical synthesis is generally based on the following displacement reaction $A_xC + yB \rightarrow xA + B_yC$, where A_xC and B are precursors, A is the desired new phase (reaction product) and B_yC is a by-product of the reaction [3, 21].The applications of mechanochemistry include exchange reactions, reduction/oxidation reactions, decomposition of compounds, and phase transformations. This process has been used successfully to prepare nanoparticles of a number of materials, including transition metals, alloys, oxide ceramics, ferrites, etc.

The nanocrystalline/nanosized ferrites were prepared especially by two basically mechanical routes: (i) directly, by reactive milling of oxides or others precursor's mixture and (ii) by dry or wet milling of the polycrystalline ferrites obtained by classical methods. As type of ferrites, by mechanical routes were obtained the follows: Fe_3O_4, $NiFe_2O_4$, $CuFe_2O_4$, $ZnFe_2O_4$, $MnFe_2O_4$, $MgFe_2O_4$, $CoFe_2O_4$, $CdFe_2O_4$, $NiAlFeO_4$, $Mn_{(1-x)}Zn_xFe_2O_4$. In the case of the soft magnetic ferrites produced by mechanical routes, a partial reversibility during milling of the reaction $\alpha\text{-}Fe_2O_3 + MeO \leftrightarrow MeFe_2O_4$ was evidenced and the particles contain several related Fe–Me–O phases [22-25]. As a consequence of the partial reversibility of the reaction, the complete formation of $ZnFe_2O_4$ spinel phase was attained after 1320 hrs of milling, while the $CuFe_2O_4$ spinel phase cannot be obtained by RM even for milling times as long as 1600 hrs [23]. Generally, the soft magnetic ferrites produced by mechanical routes exhibit a reduced particle size under 10 nm. As a consequence, the soft magnetic nanocrystalline/nanosized ferrites produced by mechanical routes present also particle size with a superparamagnetic (SPM) behaviour [26-28] and a spin canted effect [22, 27, 29, 30]. As a consequence of the spin canted magnetic structures, a nonsaturated magnetisation (even at a field of 9 T) and a ΔH_C shift to the left, depending on the milling time, were reported [22, 23]. The properties of the nanocrystalline/nanosized ferrites prepared by different mechanical routes were reviewed in ref. [31].

In last decades, many works were dedicated to obtain, by different mechanical routes, the nanocrystalline soft magnetic powders from some alloys systems based on Fe or Ni. The most studied systems are Fe-Ni and Fe-Cu. The Fe-Cu immiscible system is a representative system to illustrate the possibility of the MA to form the metastable phases, mechanically alloyed Fe_xCu_{100-x} solid solutions, which are never obtained by classical metallurgy or quenching method in immiscible binary systems.

The researches concerning alloys from Fe-Cu system produced by mechanical routes cover entire Fe-Cu diagram. The problems involved in mechanical alloying in Fe-Cu system are reviewed in ref. [32]. Generally, the solubility limit can be easily extended at 20 at% Cu in bcc phase and 6o% Fe in fcc phase [33]. A milling map of the Fe-Cu system shows that it is possible to extend to solubility limit both for bcc and fcc phases by increasing the milling time. The Fe-Cu alloys obtained by mechanical alloying present very interesting magnetic properties. Despite both Cu and Fe metals with fcc structures are nonmagnetic, the substitution of Cu atoms by Fe in fcc-Cu lattice leads to the formation of a random solid solution with the appearance of the ferromagnetic order. It was shown that the ferromagnetism (Fe-Fe positive exchange interactions) in the mechanically alloyed Fe–Cu originates when the atomic volume is expanded by a certain value (5.3% of γ-Fe, regardless of copper content), and when a certain number of neighboring iron atoms exist to percolate the ferromagnetic interaction and possibly to induce the magnetic moment on iron [34]. The mixture of Cu and bcc Fe (α-Fe) is magnetically soft with low coercivity. In the case of the fcc $Fe_{50}Cu_{50}$ solid solution an

improvement of the coercive field, remanence induction and saturation induction, comparatively with as-milled powders has been found by isothermally annealing at 450 °C. This behaviour was explained in terms of the precipitation of nanocrystalline/ultrafine Fe in Cu matrix by a spinodal decomposition [35]. A rich synthesis on the coercivity in nanocrystalline alloy powder prepared by MA is given in the reference [36]. Magnetoresistivity measurements performed at 77 K have shown giant magnetoresistance (GMR) behaviour in samples with Fe concentration between 10 and 45 at%. The highest values of GMR ratio were reached at 20 Fe at % ($\Delta\rho/\rho$ = 1% for as-prepared samples milled for 75 hours and 2.75% for as-prepared samples milled for 20 hours [37]. The Invar effect was observed in Fe-Cu solid solutions by means of lattice thermal expansion and magnetisation measurements [38].

The most studied alloys by mechanical routes belong to the Fe-Ni system. Different mechanical routes and very different milling conditions have been used to produce nanocrystalline Fe-Ni powders [15]. Very rich analysis of the phase transformation in $Fe_{1-x}Ni_x$ ($10 \leq x \geq 90$ at%) alloys by mechanical alloying and subsequent annealing was reported [39]. It was shown that single phase solid solution of MA samples is significantly wider than that of thermodynamically stable alloys. A synthesis concerning the phases which could be obtained by mechanical alloying is presented by comparison with the equilibrium phase diagram in the Fe-Ni alloys, figure 1 [40]. It can be seen a considerable extension of the solubility limit and also the obtaining a bct phase by MA. The nanocrystalline Ni_3Fe intermetallic compound was produced by mechanical alloying of elemental Ni and Fe powders and annealing [18, 19, 41-44]. The mean crystallite sizes of about 22 or 12 nm were obtained after 12 and respectively 52 hours of milling and 3 hours of annealing at 330 °C [18, 19].

The magnetic properties of the Ni-Fe powders obtained by MA depend on the milling conditions and of the structure. It was been proved that the milling performed in the “friction mode processes” leads to the formation of alloys exhibiting a soft magnetic behaviour [17, 45]. A strong decrease of the coercive field versus crystallite size appears especially for crystallite size smaller than 20 nm and a limit value of the H_C = 110 A/m was obtained for Fe-Ni 20 at% after 96 hours of milling [46]. An interesting result was obtained for $Fe_{65}Ni_{35}$ alloys, which had not Invar anomaly as suggested by the equilibrium diagram [47]. A higher Curie temperature than that for the equilibrium alloys has been observed for Fe-Ni 35 at% and Fe-Ni 50 at% [47]. Many authors report an increasing of the magnetisation with increasing the milling time [18,19, 41, 45, 47]. In the case of Ni_3Fe, it was found that M_s decreases at milling time longer than 20 hours due to presence of anti-site defects in structure, induced by milling [18,19,41]. A fall in the M_s value was observed for a mean grain size of 8 nm and it was explained by the presence of SPM particles [43].

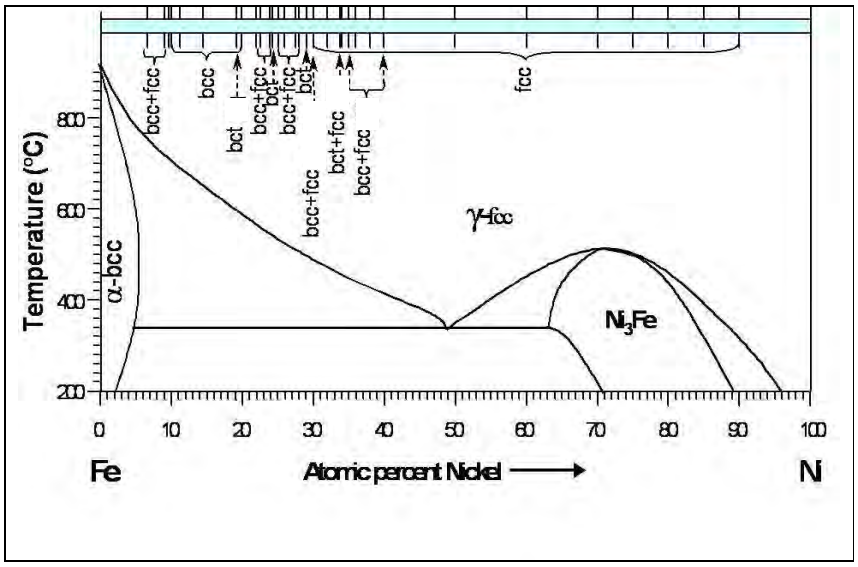

Figure 1. A synthesis concerning the phases which could be obtained by mechanical alloying by comparison with the equilibrium phase diagram in the Fe-Ni alloys. The dotted lines indicate other phases than usually reported [after Ref. 40].

The progressive synthesis of Ni_3Fe phase by MA and subsequent annealing was checked by XRD and magnetic measurements [18, 19]. It was found that the spontaneous magnetisation tend to a saturation value by Ni_3Fe compound formation. Assuming the M_S as a control parameter of the alloying process by milling and subsequent annealing, a *Milling – Annealing – Transformation* (MAT) diagram was proposed [19]. In this diagram the line M_S = constant corresponds to the milling time – annealing time pairs for which the Ni_3Fe phase is formed in the whole volume of the sample and divide the diagram in to two side.

Because of their attractive soft magnetic properties the Fe-Co powders have been produced in the nanocrystalline state by MA. It was found that in the case of $Fe_{50}Co_{50}$ and $Fe_{rich}Co$ alloys the milling implies diffusion of hcp-Co into α-Fe and finally a disordered bcc-FeCo solid solution is obtained [48-50]. A coexistence of the hcp and fcc phase and an evolution of the hcp/fcc ratio with milling time have been observed for Co-10 at% Fe [51]. It was shown that the coercivity is directly affected by the crystallite size, but not by hcp/fcc phase's ratio [51].

Many works on the ternary and policomponents alloys based on Fe and Ni obtained by mechanical routes have been reported. The nanocrystalline Supermalloy powders (Ni-Fe-Mo) have been obtained from a mixture of pre-alloyed Ni_3Fe and Mo [52, 53] and from 79Ni-16Fe-5Mo (wt%) elemental powders mixture [54, 55]. A minimum in the spontaneous magnetisation vs. milling time shows the presence of different processes in the Supermalloy formation by milling [55]. The coercivity was found to be dependent on the grain size and the domain wall width was estimated at 15 nm [52]. New data about obtaining Ni-Fe-Cu-Mo powders by mechanical alloying and subsequent annealing are recently published [56]. Finemet alloys obtained by mechanical alloying, having soft magnetic properties inferior to those of melt-spun ribbons, have been reported also [57].

The coercivity in the nanocrystalline soft magnetic mechanically alloyed powders is explained in the "random anisotropy model", which was modified in order to take into account the residual stress induced by MM [58].

The nanocrystalline soft magnetic powders produced by mechanical routes are used like powders or like starting materials to design new magnetic materials by powder consolidation. The powder consolidation with preserving the nanocrystalline structure can be made by field activated pressure assisted sintering (FAPAS) and spark plasma sintering (SPS) methods [14] or by producing of the soft magnetic composites. Some applications of these nanocrystalline powders like microwave absorbing or soft composite magnetic materials have been reported [59-61].

REFERENCES

1. C. Suryanarayana, Int. Mater. Reviews **40,** 41 (1995).
2. K. Lu, Mater. Sci. Eng. **R16**, 161 (1996).
3. S.C. Tjong , H. Chen, Mater. Sci. Eng. **R41**, 1 (2004).
4. M.E. McHenry, M.A. Villard, D.E. Laughlin, Prog. Mater. Sci. **44**, 291 (1999).
5. G. Herzer, Nanocrystalline Soft Magnetic Alloys, in Handbook of Magnetic Materials, Ed. by K.H.J. Buschow, Elsevier Science BV, Amsterdam-Lausanne (1997)
6. G. Herzer, Physica Scripta **T49**, 307 (1993).
7. B.S. Murty, S. Ranganathan, Int. Mater. Rev. **43**, 101 (1998).
8. C. C. Koch, J. D. Whittenberger, Intermetallics **4**, 339 (1996).
9. C. Suryanarayana, Progr. Mater. Sc. **46**, 1 (2001).
10. A. R. Yavari, Mater. Trans. JIM **36**, 228 (1995).
11. P. H. Shingu, K. N. Ishihara, Mater. Trans. JIM **36**, 96 (1995).

12. A. Arrott, Nanostructured Mater. **12**, 1135 (1999).
13. D.L. Zhang, Progr. Mater. Sci. **49**, 537 (2004).
14. E. Gaffet, G. Le Caër, Mechanical Processing for Nanomaterials, in Encyclopaedia of Nanoscience and Nanotechnology, vol.X, Ed. by H.S. Nalwa, American Sci. Publishers (2004).
15. I.Chicinaş, J. Opt. Adv. Mater. **8**, 439 (2006).
16. M. Abdellaoui, E. Gaffet, Acta. Metall. Mater. **44**, 1087 (1995).
17. R. Hamzaoui, O. Elkedim, E. Gaffet, Mater. Sci. Eng. **A 381**, 363 (2004).
18. I. Chicinaş, V. Pop, O.Isnard, J.M. Le Breton, J. Juraszek, J. Alloys Comp. **352**, 34 (2003).
19. V. Pop, O. Isnard, I. Chicinaş, J. Alloys Comp. **361**, 144 (2003).
20. Z. Sparchez, I. Chicinaş, O. Isnard, V. Pop, F. Popa, J. Alloys and Compounds, **434–435**, 435 (2007).
21. L. Takacs, Progr. Mater. Sci. **47**, 355 (2002).
22. G.F. Goya, H.R. Rechenberg, J.Z. Jiang, J. Appl. Phys. **84**, 1101 (1998).
23. G.F. Goya, H.R. Rechenberg, J. Metastable and Nanocrystalline Mater. **14**, 127 (2002).
24. J.Z. Jiang, G.F. Goya, H.R. Rechenberg, J. Phys.: Condens. Mater. **11**, 4063 (1999).
25. F. Padella, C. Alvani, A. La Barbera, G. Ennas, R. Liberatore, F. Varsano, Mater. Chem. Phys. **90**, 172 (2005).
26. G.F. Goya, J. Mater. Sci. **39**, 5045 (2004).
27. V. Šepelák, D. Baabe, D. Mienert, D. Schultze et al., J. Magn. Magn. Mater. **257**, 377 (2003).
28. S. Ozcan, B. Kaynar, M.M. Can, T. Firat, Mater. Sci. Eng. B **121,** 278, (2005).
29. M. Menzel, V. Šepelák, K.D. Becker, Solid State Ionics **141-142**, 663 (2001).
30. V. Šepelák, I. Bergmann et al. J. Phys. Chem. *C* **111** (2007), 5026
31. V. Šepelák, I. Bergmann, S. Kips, K.D. Becker, Z. Anorg. Allg. Chem. **631**, 993 (2005).
32. J.Z. Jiang, C. Gente, R. Bormann, Mater. Sci. Eng. **A242**, 268 (1998)
33. P.J. Schilling, J.H. He, R.C. Tittsworth, E. Ma, Acta Mater. **47**, 2525 (1999).
34. H. Ino, K. Hayashi, T. Otsuka, D. Isobe, K. Tokumitsu, K. Oda, Mater. Sci. Eng. **A304-306**, 972 (2001)
35. B.N. Mondal, A. Basumallick, P.P. Chattopadhyay, J. Magn. Magn. Mater. **309**, 290 (2007)
36. R.B. Schwarz, T.D. Shen, U. Harms, T. Lollo, J. Magn. Magn. Mater. **283**, 223 (2004).
37. L.M. Socolovsky, F.H. Sánchez, P.H. Shingu, Hyperfine Inter. **133**, 47 (2001)

38. P. Gorria, D. Martinez-Blanco, J.A. Blanco, Phys. Rev. B **69**, 214421 (2004)

39. S.D. Kaloshin, V.V. Tcherdyntsev, I.A. Tomilin, Yu.V. Baldokhin, E.V. Shelekhov, Physica B **299**, 236 (2001).

40. V. Pop, I. Chicinaş, J. Optoelectron. Adv. Mater. **9,** 1478, (2007).

41. I. Chicinas, V. Pop, O. Isnard, J. Magn. Magn. Mater. **242-245**, 885 (2002).

42. C. N. Chinnasamy, A. Narayanasamy, K. Chattopadhyay, N. Ponpandian, Nanostr. Mater., **12**, 951 (1999).

43. C. N. Chinnasamy, A. Narayanasamy et al. Mater. Sci. Eng. **A304-306**, 408 (2001).

44. B.H. Meeves, G.S. Collins, Hyperfine Interact. **92**, 955 (1994).

45. R. Hamzaoui, O. Elkedim, E. Gaffet, J. Mater. Sci. **39**, 5139 (2004).

46. R. Hamzaoui, O. Elkedim, N. Fenineche, E. Gaffet, J. Craven, Mater. Sci. Eng. **A 360**, 299 (2003).

47. E. Jartych, J.K. Żurawicz, D. Oleszak, M. Pękała, J. Magn. Magn. Mater. **208**, 221 (2000).

48. M. Sorescu, A. Grabias, Intermetallics **10**, 317 (2002).

49. Y. Liu, J. Zhang, L. Yu, G. Jia, C. Jing, S. Cao, J. Alloys Comp. **377**, 202 (2004).

50. H. Moumeni, S. Alleg, J.M. Greneche, J. Alloys Comp. **386**, 12 (2005).

51. N.E. Fenineche, R. Hamzaoui, O. El Kedim, Mater. Lett. **57**, 4165 (2003).

52. Y. Shen, H.H. Hng, J.T. Oh, J. Alloys Comp. **379**, 266 (2003).

53. Y. Shen, H.H. Hng, J.T. Oh, Mater. Lett. **58**, 2824 (2004).

54. I. Chicinas, V. Pop, O. Isnard, J. Mater. Sci. **39**, 5305 (2004).

55. O. Isnard, V. Pop, I. Chicinas, J. Magn. Magn. Mater. **290-291**, 1535 (2005).

56. F. Popa, O. Isnard, I. Chicinaş, V. Pop, J. Magn. Magn. Mater. **316,** e900, (2007).

57. M. Manivel Raja, K. Chattopadhyay, B. Majumdar, A. Narayanasamy, J. Alloys Comp. **297**, 199 (2000).

58. T. D. Shen, R. B. Schwarz, J. D. Thompson, Phys.Rev B **72**, 014431-1 (2005).

59. P.H. Zhou, L.J. Deng, J.L. Xie, D.F. Liang, L. Chen, X.Q. Zhao, J. Magn. Magn. Mater. **292**, 325 (2005).

60. I. Chicinas, O. Geoffroy, O. Isnard, V. Pop, J. Magn. Magn. Mater. **290-291**, 1531 (2005).

61. I. Chicinas, O. Geoffroy, O. Isnard, V. Pop, J. Magn. Magn. Mater. **310**, 2474 (2007).

SOFT NANOCRYSTALLINE ALLOYS (MELT SPUN)

OLIVIER GEOFFROY*

1. Presentation

Nanocrystalline magnetic soft alloys were patented in 1987 [Yos 88] and can be seen as an extension of amorphous magnetic soft alloys, introduced towards 1970. There intrinsic extremely high magnetic permeability coupled with a low production cost allow to use them for a wide range of applications.

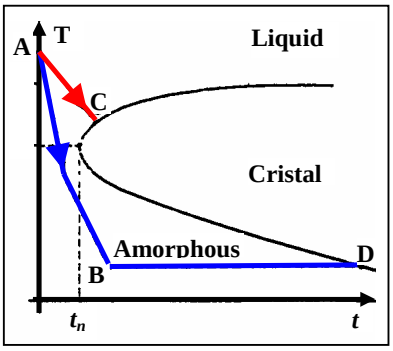

Fig. 1. Temperature-duration-Transformation rate diagram

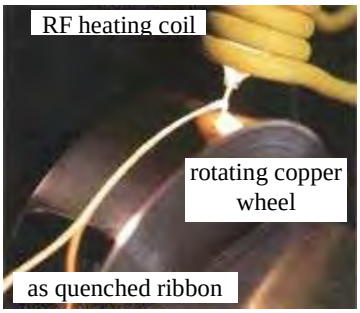

Fig. 2a. melt spinning Process

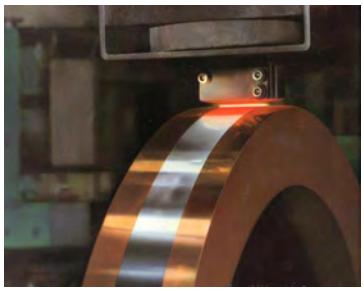

Fig. 2b. Planar flow casting

Different families exist with Typical composition (atomic):

* $Fe_{73.5}Cu_1Nb_3Si_{15,5}B_7$ (***Finemet*** by Hitachi Metals, ***Vitroperm*** by Vacuumschmelze GmbH, † ***Nanophy*** by Imphy Alloys)
* $Fe(Co)_{86}Zr_7B_6Cu_1$ († ***Nanoperm*** by Alps Electric Co.)
* $(Fe_{1-x}Co_x)_{88}Hf_7B_4Cu_1$: ***Hitperm***

* Institut Néel, CNRS - Université Joseph Fourier, BP 166, 38042 Grenoble cedex 9, France

2. Elaboration and crystallographic structure

The elaboration is made of two stages:

* **First stage:** Elaboration of an amorphous precursor:
  - ➡ glass formers are needed (B, Hf…)
  - ➡ It is necessary to achieve very high cooling rate to prevent crystallisation (cf on fig 1: route AB instead of route AC):

$$\frac{dT}{dt} > 10^6 \text{ K / s}$$

  - ➡ Different technical processes exist:
  - * Splat cooling (Not industrial): compression of a liquid drop between two cooper disks.
  - * Projection on a rotative cooled cooper wheel (Industrial):
    - Melt spinning for ribbons of several millimetres width
    - Planar flow casting for ribbons of several centimetres width (until 20 cm)
* **Second stage:** Nanocristallisation annealing (≈ One hour, $T_{anneal} \approx 500$ °C)

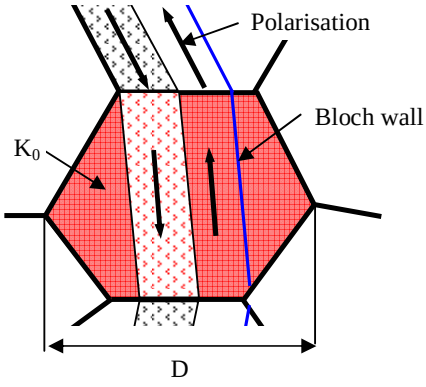

Fig. 3a. domain walls in classical crystalline alloys ($e_w \approx 3$ L << D)

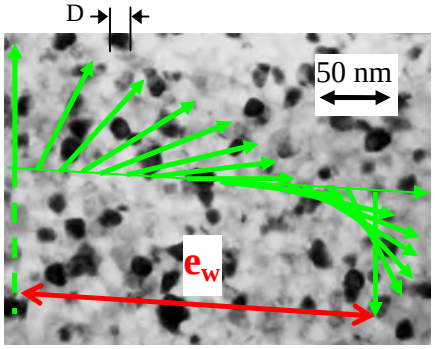

Fig. 3b. Microstructure of a Nanophy sample (Imphy Alloy). Superimposed, extension of a domain wall (thickness $e_w \approx 3$ L >> D)

- ➡ Rapid diffusion of Cu initiates local nucleation of crystalline FeSi (Finemet) or Fe (Nanoperm) with random crystallisation directions.
- ➡ Slow diffusion of Nb (Finemet) or Zr (Nanoperm) inhibs growth of crystallites: typical size D ≈ 10-20 nm
- ➡ Atypical resulting crystalline structure (cf fig 3):

Coexistence of a soft magnetic nanocristalline phase (Fe or FeSi) with a residual amorphous phase.
volumic crystalline fraction f ≈ 70 %

3. Magnetic Properties

* Amorphous phase ensures continuity of magnetic exchanges interactions between nanograins:
  - ➡ from a magnetic point of view, ribbon = continuous medium
  - ➡ extension of a Domain-Wall upon a great number of grains (e_w >> D, cf. Figure 3b)
  - ➡ At the scale of the DW, anisotropy K_{eff} much smaller than the crystallographic one K_0 due to averaging.

In addition: very low magnetostriction (cf. fig.7):

$\lambda_s(f= 70\%) \approx 10^{-6}$

➡ Coercivity ↘↘ ($H_c < 1$ A/m)
Permeability ↗↗ ($\mu_r > 10^5$)

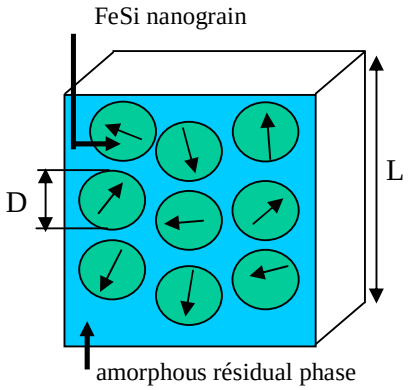

Fig. 4. Magnetic correlated volume L^3 comprising $n = f (L/D)^3$ nanograins. Arrows feature the distribution of magnetization easy axes due to random cristallization

<u>Quantitative description:</u> **R**andom **A**nisotropy **M**odel
Magnetic independent entity = **C**orrelated **V**olume of side L (magnetic correlation length) (cf. fig. 4).

The effective anisotropy K_{eff} is driven by the random magnetocristalline contribution K_a. Noticing A the exchange stiffness, one obtains:

$$\left.\begin{array}{l} L = \sqrt{A\,K_{eff}} \\ K_{eff} = K_a = \sqrt{\langle K^2 \rangle} = K_0 / \sqrt{n} \\ n = f\,(L / D)^3 \end{array}\right\} \; K_{eff} \approx K_0^{\,4}\, A^{-3}\, f^{-2}\, D^6 \qquad (1)$$

$\mathbf{H_c \approx K_{eff} \approx D^6}$ (cf. Fig.5)

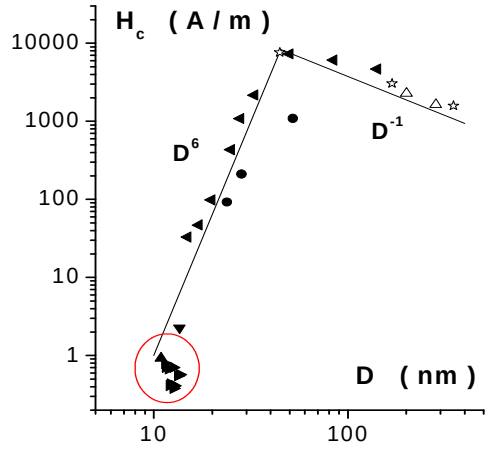

Fig. 5. Evolution of the coercitivity with the grain size. The D^{-1} dependancy corresponds to classical alloys (e_w << D, see fig.3a). The circle denotes the region where magnetoelastic effects have to be considered

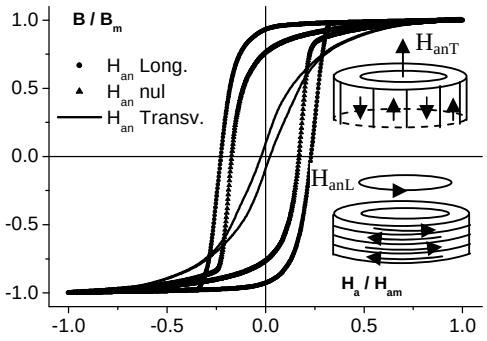

Fig. 6. different shapes of the hysteretical loop (round, flat, rectangular) obtained applying a magnetic field during annealing

➡Related property:

Due to vanishing anisotropies, possibility to tailor the shape of the hysteretic loop by means of induced anisotropy applying stress or magnetic field during crystallisation annealing (cf fig. 6) [ALV 05]

4. Magnetostriction and Magnetoelastic effects:

For little grain sizes (D ≈ 10 nm), deviation from the D^6 law occurs (cf. fig.5, circle): in this region, **M**agneto**E**lastic effects give a significant contribution K_{me} to K_{eff}, leading instead of (1) to [SUS 98]:

$$K_{eff}^2 = K_{me}^2 + K_a^2 = K_{me}^2 + K_0^2 A^{-3/2} f^{-1} D^3 K_{eff}^{-3/2} \qquad (2)$$

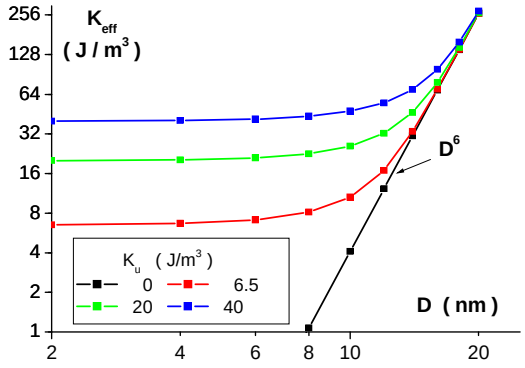

Fig. 7. Modelisation of K_{eff} as a function of grains size for different valeues of K_u ($A = 10^{-11}$ J/m, f=1, K_0 = 8000 J/m^3)

Figure 7 illustrates the competition between K_{me} and K_a. It is so expected that for little grain sizes H_c is controlled by the magnetostriction coeff. λ_s.
Measurements show that λ_s linearly depends on crystalline fraction f (cf. fig. 8) with, as a first approximation, the typical behaviour

$$\lambda_s = f\,\lambda_c + (1-f)\,\lambda_a$$

λ_c, λ_a = magnetostriction of crystalline and amorphous phases[1].

[1] An accurate modelisation has to take into account the f dependance of λ_a due to change in the amorphous phase composition and the contribution of surface magnetostriction to λ_c in the little grain sizes range [SLA 98], [NAN 01], [SZU 02]

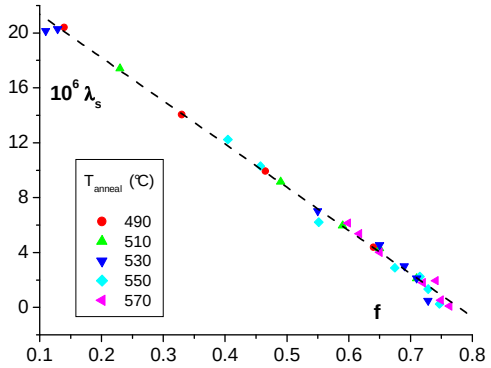

Fig. 8. evolution of λ_s (measured by SAMR method) as a function of cristalline fraction f (samples Nanophy)

Starting from H_c, D, f, measurements, K_{me} is obtained from (2) and can be compared to λ_s measurements. With E = Young Modulus, it is experimentally obtained (cf. fig. 9)

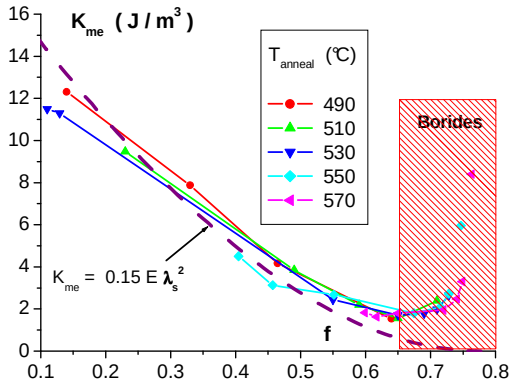

Fig. 9. Evolution of K_{me} obtained from H_c measurements following (2) on Nanophy samples Comparison with a fit $\approx E \lambda_s^2$.

$$K_{me} = \alpha E \lambda_s^2 \qquad \alpha = 0{,}15$$

The λ_s^2 dependency indicates that the source of stress is internal. Simple scaling argument explains that the source of Magnetoelastic frustration does not lie at the interface nanograin / amorphous but at the scale of the CV itself. According to quantitative modelisation [GEO 06], a reasonable scheme is that frustration occurs

when the magnetization reverses in the CV: its shape (in black on Fig. 9) is imposed by the magnetization of the surrounding medium (black arrows), even when its own magnetization (red arrow) would promote the red shape (dash line).

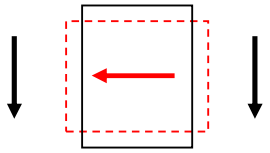

Fig. 10. Schematic view of ME frustration occuring in CV at magnetisation reversal

5. Additional properties

* Ribbon thickness ≈ 20 µm
* Electrical resistivity ρ ≈ 140 10^{-8} Ω

→ Nanocristalline alloys = good candidates for medium frequencies applications

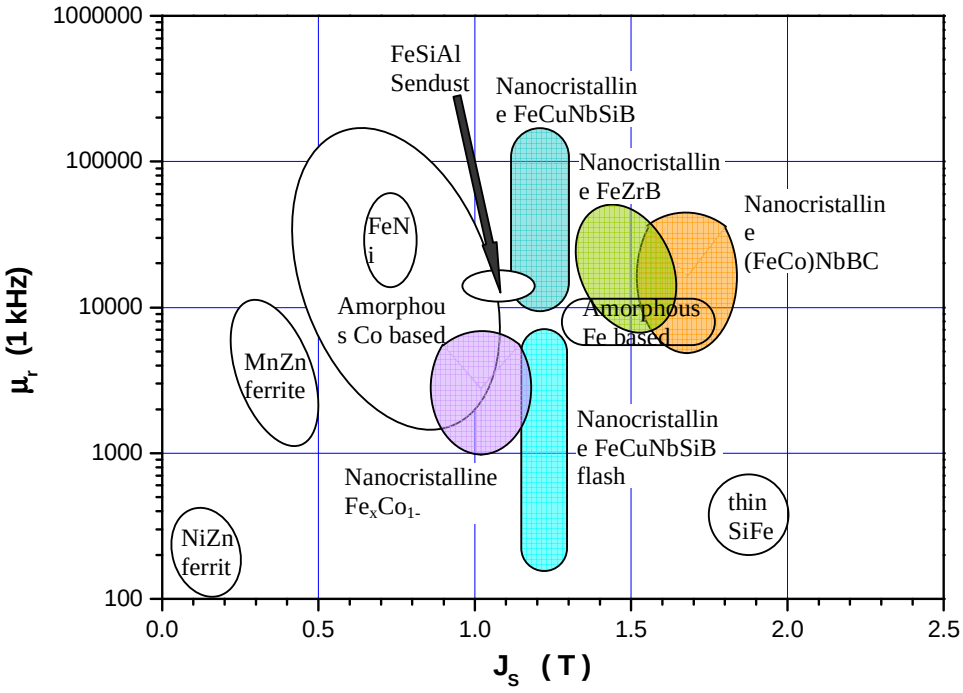

Fig. 11. general view of soft magnetic materials for medium frequency applications [WAE 06]

* Magnetisation Saturation:
  $J_S \approx 1{,}25$ T (Finemet) $J_S \approx 1.7$ T (Nanoperm) [SUS 91]
* Operating Temperature
  ≈ **150 °C** limited by the Curie Temperature of the residual amorphous phase T_{Cam} (cf. Fig.12)
  ➡ Enhancement of T_{Cam} by partial substitution of Fe by Co in Finemet or Nanoperm (➡ Hitperm) [WIL 99], [MIT 04], [GER 06]
  ➡

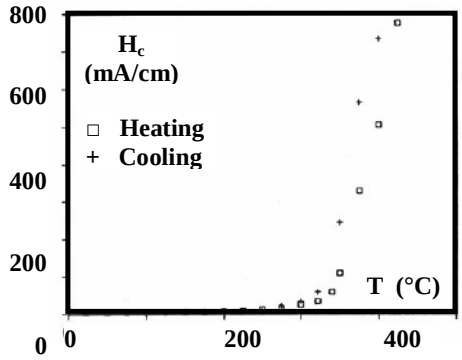

Fig. 12. Coercivity of Finemet (annealed 1h 540°C) as a function of temperature measurement [Her 89]

REFERENCES

[ALV 05] Alves F., Simon F., Kane S. N., Mazaleyrat F., Waeckerle T., Save T., Gupta A., J. Mag. Mag. Mater. 294, 2005, e141
[GEO 06] Geoffroy O., Chazal H., Porteseil J.-L., Waeckerlé T., Alves F., J. Mag. Mag. Mat., 304, 2006, 145
[GER 06] Gercsi Zs., Mazaleyrat F., Varga L. K., J. Mag. Mag. Mat., 302, 2006, 454
[MIT 04] Mitra A., Kim H.-Y., Louzguine D. V., Nishiyama N., Shen B., Inoue A., J. Mag. Mag. Mat., 278, 2004, 299
[NAN 01] Nan CeWen, Huang Jin H., Wenig G. J., J. Mag. Mag. Mat., 233, 2001, 219
[SLA 01] Slawska-Waniewska A., J. Phys. IV France 8, 1998, Pr2-11
[SUS 91] Suzuki K., Makino A., Inoue A., J. Appl. Phys., 70, 1991, 6232
[SUS 98] Suzuki K., Herzer G., Cadogan J.M., J. Mag. Mag. Mat., 177-181, 1998, 949
[SZU 02] Szumiata T., Brzozka K., Gawronski M., Gorka B., Jezuita K., Blazquez-Gamez J. S., Kulik T., Zuberek R., Slawska-Waniewska A., Greneche J.M., J. Mag. Mag. Mater. 250, 2002, 83
[WAE 06] Waeckerle T., Alves F. in "Matériaux magnétiques en génie électrique", Kedous-Lebouc ed., Lavoisier Publishing
[WIL 99] Willard M. A., Huang M.-Q., Laughlin D. E., McHenry M. E., J. Appl. Phys., 85, 1999, 4421
[YOS 88] Yoshizawa Y., Oguma S., Yamauchi K., J. Appl. Phys., 64, 1988, 6044

STUDIA UNIVERSITATIS BABEŞ-BOLYAI, PHYSICA, LII, 1, 2007

NANOSTRUCTURED HARD MAGNETS

JULIA LYUBINA[*], OLIVER GUTFLEISCH[*]

Permanent magnets find application in a wide variety of devices, from everyday appliances like loudspeakers to motors, data storage and medical (e.g. magnetic resonance imaging) devices. There is a constant search for new materials with superior properties, either in the form of new magnetic compounds or in the form of known materials with improved magnetic properties. Modern high-performance magnets are based on intermetallic compounds of rare-earths (R = Nd, Pr, Sm) and 3*d* transition metals (T = Fe, Co) with very high magnetocrystalline anisotropy, such as $Nd_2Fe_{14}B$ and $SmCo_5$ [1-3]. FePt magnets with the $L1_0$ structure have recently attracted much attention because of their potential usage in ultra high-density data storage and permanent magnets for special applications. The material design on a nanoscale is one of the possibilities to improve the magnet performance. In this presentation, the complex relation between the structure, microstructure and magnetic properties of modern high-performance magnets will be reviewed.

1. Magnetic properties of hard magnetic materials

The interactions on the atomic scale determine the intrinsic magnetic properties of a material, such as the spontaneous magnetisation M_s, the Curie temperature T_c and the magnetocrystalline anisotropy constant K_1. The extrinsic magnetic properties of hard magnetic materials, remanent magnetisation (remanence) M_r and coercive force (coercivity) H_c, are related to magnetic hysteresis and are determined to a great extent by the microstructure. Another key characteristic of a permanent magnet is the energy product $(BH)_{max}$, which is twice the maximum magnetostatic energy available from a magnet of optimal shape. The energy product increases both with increasing coercivity and remanence. However, for materials with sufficiently high H_c, the energy product can never exceed the value $\mu_0 M_r^2 / 4$.

The remanent magnetisation of real magnets is usually below its saturation value (mostly due to lack of grain alignment). In particular, the remanence-to-saturation ratio M_r/M_s is limited to 0.5 for magnets composed of non-interacting uniaxial randomly oriented particles. The processing route for obtaining an anisotropic magnet (e.g. sintering) is in general more sophisticated than that for a non-textured

[*] IFW Dresden, Institute for Metallic Materials, P.O. Box 270016, 01171 Dresden, Germany, j.lyubina@ifw-dresden.de

magnet, thus justifying the efforts to obtain a better M_r/M_s ratio in the latter. A possibility to increase M_r in non-textured magnets is remanence enhancement in the so-called *exchange-spring* or *exchange-coupled* magnets [4-6]. In general, remanence enhancement in this type of magnets is attributed to intergrain coupling via exchange interaction. This coupling causes the magnetisation of neighbouring grains to deviate from their particular easy axis resulting in a magnetisation increase parallel to the direction of the applied field. The exchange-coupling concept has its origin in the random-anisotropy theory [7, 8].

Assemblies of high anisotropy (hard magnetic) grains are termed single-phase exchange-coupled magnets and a combination of a high anisotropy phase with a less anisotropic (soft magnetic) phase is called nanocomposite exchange-coupled magnets. Various combinations of hard magnetic phases with soft magnetic phases have been synthesised including $R_2Fe_{14}B/\alpha$-Fe (R = Nd, Pr), $Sm_2Fe_{17}N(C)_x/\alpha$-Fe, Sm-Co/α-Fe(Co) and FePt/Fe_3Pt exchange-coupled nanocrystalline bulk magnets [4, 9-14], as well as thin films and multilayers [15-17].

2. R-Fe-B (R = Nd, Pr)

An overview of the most relevant manufacturing routes, with special emphasis on nanostructured magnets, is given in the flow chart of figure 1, which illustrates the principal processing routes of rare-earth permanent magnets (RPMs) [18]. For the

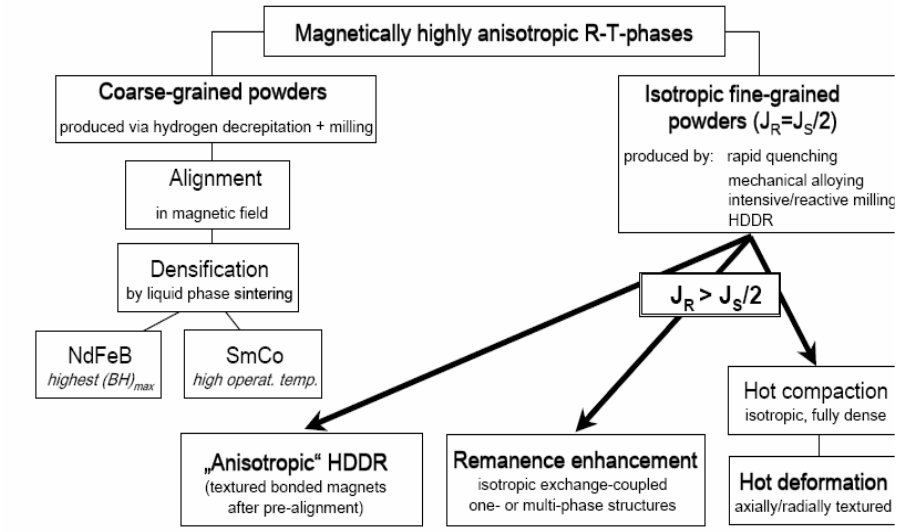

Fig. 1. Flow chart illustrating the principal processing routes of high energy density RPMs based on coarse- and fine-grained powders.

production of high performance RPMs with maximum energy densities a careful control of low level metallic impurities and non-metallic impurities such as oxygen is pivotal during all processing stages, regardless of which processing route is chosen. Each branch ends by machining and magnetising the magnet. The left branch represents classical powder-metallurgical processing resulting in monocrystalline particles of typically 10 µm in diameter, hence large compared to the critical single-domain particle size d_c, which is in the range of 200–300 nm for $Nd_2Fe_{14}B$ and $Pr_2Fe_{14}B$. The right branch of this figure embodies processing routes, which aim at grain sizes considerably smaller than d_c.

In general, there exist three prototypes of RPMs based on $R_2Fe_{14}B$. Type (I) is rare earth rich and the individual crystallites are separated by Nd-rich (oxide) intergranular phase, which basically is a thin paramagnetic layer. This structure leads essentially to a magnetic decoupling and each hard magnetic grain behaves like a small permanent magnet, which results in high coercivity. Type (II) can be obtained using the stoichiometric $R_2Fe_{14}B$ composition and the grains are exchange-coupled without an additional phase between them. Provided the grains are small enough, a remanence enhancement is observed. A further increase in remanence is found in the type (III) nanocomposite magnet, a two- or multi-phase exchange coupled magnet, where a rare-earth deficient composition is used and the coupling occurs between the $R_2Fe_{14}B$ grains and soft magnetic crystallites (α-Fe or/and Fe_3B).

In this presentation, concepts of maximising the energy density in nanostructured magnets by either inducing a texture via anisotropic HDDR processing or hot deformation, or enhancing the remanence via magnetic exchange coupling are evaluated. A model for the texture memory effect in HDDR processed $Nd_2Fe_{14}B$ materials is introduced [19]. Highly textured Nd-rich $(Nd,Pr)_2Fe_{14}B$ obtained by hot deformation show unique magnetic microstructures based on cooperative phenomena. Magnetic force microscopy (MFM) is used to image the so-called “interaction domains” [20]. For nanostructured isotropic, multi-phase (Nd,Pr)FeB-based materials, enhanced remanence is observed.

3. $Sm_2(Co,Cu,Fe,Zr)_{17}$-type magnets

$Sm_2(Co,Cu,Fe,Zr)_{17}$–type magnets are typical pinning hardened magnets, i.e. reverse domains are prevented from growing by various pinning centres. Recently significant progress has been made in the development of high temperature $Sm(Co_{bal}Fe_vCu_yZr_x)_z$ magnets and operating temperatures of up to 500°C are now feasible [21, 22]. This extraordinary behaviour has to be attributed to the special composed of a three-phase system: Fe-rich rhombohedral 2:17 pyramidal cells, Cu-rich hexagonal cell walls of 1:5 structure and Zr-rich lamellae of 2:17 phase intersecting the cells perpendicular to the *c*-axis. The evolution of nanostructure, microchemistry and magnetic properties during a complex heat treatment regime of

melt-spun and sintered $Sm(Co_{bal}Fe_vCu_yZr_x)_z$ magnets is described. A characteristic gradient of domain wall energy within the $Sm(Co,Cu)_5$ cell boundary phase depending on subtle changes in microchemistry, namely the Cu content, is responsible for a specific domain wall pinning mechanism.

4. $L1_0$-type Fe-Pt magnets

Since the mid-1930s Fe-Pt alloys are known to exhibit high coersivities due to high magnetocrystalline anisotropy of the $L1_0$ FePt phase [23], but the high price prevented widespread applications of these alloys. Distinct advantages of Fe-Pt alloys are, as opposed to the rare-earth-transition-metal-based compounds, that they are very ductile and chemically inert. These magnets present interest for specialised applications such as in magnetic micro-electromechanical systems (magnetic MEMS) or in aggressive environments, for instance, in dentistry, where they are used as magnetic attachments to retain dental prostheses in the oral cavity.

Through the use of mechanical alloying and subsequent heat treatment the formation of chemically highly ordered $L1_0$ FePt and, in the case of the Fe-rich and Pt-rich compositions, $L1_2$ Fe_3Pt and $FePt_3$ phases, respectively, is achieved. Whereas in Pt-rich alloys the decoupling effect of the $FePt_3$ phase leads to coercivity improvement, in Fe-rich nanocomposites a peculiar nanometer scale multilayer structure gives rise to remanence enhancement due to large effects of exchange interactions between the crystallites of the phases [14, 24]. The structure, magnetic properties [25] and magnetisation reversal processes of these alloys are described.

REFERENCES

1. J. M. D. Coey (editor), *Rare-Earth Iron Permanent Magnets* (Clarendon Press, Oxford, UK, 1996).
2. K.H.J. Buschow, in: *Handbook of Magnetic Materials*, vol. 10, K.H.J. Buschow (editor): Chapter 4, *Magnetism and processing of permanent magnet materials* (North Holland Elsevier, Amsterdam, Netherlands, 1997).
3. R. Skomski and J. M. D. Coey, *Permanent Magnetism* (IoP Publishing, Bristol and Philadelphia 1999).
4. R. Coehoorn, D. B. de Mooij, J. P. W. B. Duchateau, K. H. J. Buschow, *Novel permanent magnetic materials made by rapid quenching*, J. de Phys. 49 (1988) C8-669.
5. D. Eckert, A. Handstein, K.-H. Müller, R. Hesske, J. Schneider, N. Mattern, L. Illgen, *Material structure, domain structure, and magnetization processes in $Nd_4Fe_{77}B_{19}$ permanent magnets*, Mater. Lett. 9 (1990) 289
6. E. F. Kneller, R. Hawig, *The exchange-spring magnet: a new material principle for permanent magnets*, IEEE Trans. Magn. 27 (1991) 3588. [4]
7. Y. Imry, S. Ma, *Random-field instability of the ordered state of continues symmetry,* Phys. Rev. Lett. 35 (1975) 1399. [5]

8. E. Callen, Y. J. Liu, J. R. Cullen, *Initial magnetisation, remanence, and coercivity of the random anisotropy amorphous ferromagnet*, Phys. Rev. B 16 (1977) 263-270.
9. A. Manaf, P. Z. Zhang, I. Ahamad, H. A. Davies, R. A. Buckley, *Magnetic properties and microstructural characterisation of isotropic nanocrystalline Fe-Nd-B based alloys*, IEEE Trans. Magn. 29 (1993) 2866.
10. J. Ding, P. G. McCormick, R. Street, *Remanence enhancement in mechanically alloyed isotropic Sm_7Fe_{93}-nitride*, J. Magn. Magn. Mater. 124 (1993) 1.
11. E. H. Feutrill, P. G. McCormick, R. Street, *Magnetization behaviour in exchange-coupled $Sm_2Fe_{14}Ga_3C_2/\alpha$-Fe*, J. Phys. D: Appl. Phys. 29 (1996) 2320.
12. S. Hirosawa, H. Kanekiyo, M. Uehara, *High-coercivity iron-rich rare-earth permanent magnet material based on $(Fe, Co)_3B$-Nd-M (M=Al, Si, Cu, Ga, Ag, Au)*, J. Appl. Phys. 73 (1993) 6488.
13. A. Bollero, O. Gutfleisch, K.-H. Müller, L. Schultz, G. Drazic, *High-performance nanocrystalline PrFeB-based magnets produced by intensive milling*, J. Appl. Phys. 91 (2002) 8159.
14. J. Lyubina, I. Opahle, K.-H. Müller, O. Gutfleisch, M. Richter, M. Wolf, L. Schultz, *Magnetocrystalline anisotropy in $L1_0$ FePt and exchange coupling in FePt/Fe_3Pt nanocomposites*, J. Phys.: Condens. Matter 17 (2005) 4157.
15. S. M. Parhofer, J. Wecker, C. Kuhrt, G. Gieres, L. Schultz, *Remanence enhancement due to exchange coupling in multilayers of hard- and softmagnetic phases*, IEEE Trans. Magn. 32 (1996) 4437.
16. E. E. Fullerton, J. S. Jiang, S. D. Bader, *Hard/soft magnetic heterostructures: model exchange-spring magnets*, J. Magn. Magn. Mater. 200 (1999) 392.
17. H. Zeng, J. Li, J. P. Liu, Z. L. Wang, S. Sun, *Exchange-coupled nanocomposite magnets by nanoparticle self-assembly*, Nature 420 (2002) 395.
18. O. Gutfleisch, *Controlling the properties of high energy density permanent magnetic materials by different processing routes*, J. Phys. D: Appl. Phys. 33 (2000) R157.
19. O. Gutfleisch, K. Khlopkov, A. Teresiak, K.H. Müller, G. Drazic, C. Mishima, Y. Honkura, *Memory of texture during HDDR processing of NdFeB*, IEEE Trans. on Magn. 39 (2003) 2926.
20. K. Khlopkov, O. Gutfleisch, R. Schaefer, D. Hinz, K.-H. Mueller, L. Schultz, *Interaction domains in die-upset NdFeB magnets in dependence on the degree of deformation*, J. Magn. Magn. Mater. 272-276 (2004) e1937.
21. G.C. Hadjipanayis, W. Tang, Y. Zhang, S.T. Chui, J.F. Liu, C. Chen, H. Kronmüller, *High temperature 2:17 magnets: relationship of magnetic properties to microstructure and processing*, IEEE Trans. Magn. 36 (2000) 3382.
22. O. Gutfleisch, K.-H. Mueller, K. Khlopkov, M. Wolf, A. Yan, R. Schaefer, T. Gemming, L. Schultz, *Evolution of magnetic domain structures and coercivity in high-performance SmCo 2:17-type permanent magnets*, Acta Mater. 54 (2006) 997.
23. L. Graf and A. Kussmann, *Zustandsdiagramm und magnetische Eigenschaften von Platin-Eisen-Legierungen*, Physik. Z. 36 (1935) 544.
24. J. Lyubina, O. Gutfleisch, K.-H. Müller, L. Schultz, *Structure and hysteresis properties of nanocrystalline FePt powders*, J. Magn. Magn. Mater. 290-291 (2005) 547-550.
25. Lyubina, O. Isnard, I. Opahle, M. Richter, O. Gutfleisch, K-H. Müller, L. Schultz, *Influence of composition and order on the magnetism of Fe-Pt alloys: neutron powder diffraction and theory*, Appl. Phys. Lett. 89 (2006) 032506.

STUDIA UNIVERSITATIS BABEŞ-BOLYAI, PHYSICA, LII, 1, 2007

GIANT MAGNETO-IMPEDANCE AND APPLICATIONS

MANUEL VAZQUEZ*

The Giant Magnetoimpedance, GMI, effect consists of a large variation of the impedance of a metallic magnetic conductor when submmitted to the action of a dc magnetic field. Typically, impedance is experimentally determined by the four point technique by which an ac current flows along the sample and a voltage is picked up to determine the impedance. Both components, real and imaginary, of impedance contribute to the GMI.

Its origin is related to the classical electromagnetic skin effect. When a high-frequency current flows along the sample, typically elongated, it is restricted to a small thickness at its surface. This penetration depth, according to the classical theory, is inversely proportional to the conductivity and to the permeability of the sample as well as to the frequency of the ac current. Consequently, large conductivity and permeability values lead to a reduced skin depth penetration depth. The skin effect has been conventionally studied in metallic conductors with high electrical conductivity so, elements like Cu, Au or Ag exhibit noticeable skin effect.

Although previously discovered, it has not been until the decade of the 90's when GMI has been actually observed and studied in a wide spetrum of magnetic materials with relatively high electrical conductivity. The magnetic permeability of such materials can be modified by the action of a dc magnetic field in such a way that it changes the penetration depth of the skin effect. Consequently, the impedance of these materials depends on the applied dc field. To observe the GMI effect is thus neccesary to deal with a material of large permeability which in addition can be suitably modified by a dc field. In short. GMI is expected to be observed in ultrasoft magnetic materials with as large as possible electrical conductivity. Also, their thickness should be comparable to the changes of skin depth induced by the applied dc field.

* Institute for Materials Science, CSIC 28049 Madrid. Spain, mvazquez@icmm.csic.es

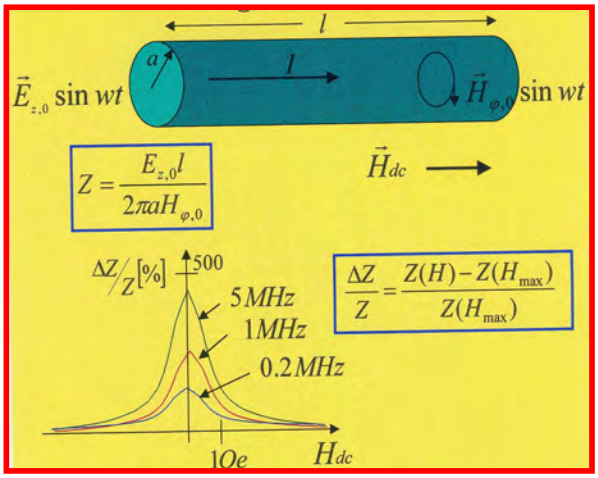

Figure 1.- Schematic view of the GMI effect is summarized in the figure, where a current *I* flows a long a wire submitted to a magnetic field H_{dc}. The definition of GMI as the relative change of impedance, $\Delta Z/Z$, is given together with a typical result for a magnetic microwire as a function of the applied field for a range of frequencies of the current *I*.

GMI is particularly large in materials as soft amorphous materials (ribbons and wires) where besides their soft character, they exhibit relatively high conductivity. Typical range of frequency at which GMI is observed goes from 100 kHz to 10 MHz for amorphous wires and ribbons, and typically increases with working frequency. Even though they are not so soft materials, GMI has been also observed in thin films and multilayers, and multilayer microwires (see figure 2).

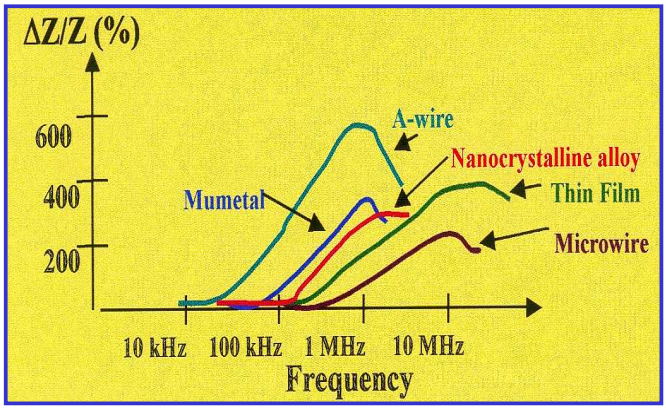

Figure 2.- Typical values of GMI for several families of soft magnetic materials

As a consequence of the stress dependence of magnetic permeability, changes in impedance can be observed in those materials when submitted to changing mechanical stress as tensile or torsional stresses. In such a case we will be talking about stress impedance, SI.

The connection between GMI effect and ferromagnetic resonance, FMR, has been discussed in a number of works. In this case, resonance phenomena are typically observed in the GHz range, and particularly the natural ferromagnetic resonance, NFMR, is detected between 2 and 12 GHz for example for amorphous microwires depending on the magnetostriction constant.

Applications of GMI effect have been proposed in a number of sensor devices where sensing element exhibits the mentioned characteristics. A number of sensor devices make use of GMI effect. The first and main application is as magnetic field sensor, where the GMI element is placed in a region of changing dc field which amplitude is to be quantified. A direct consequence of it is for example a dc current sensor where the magnetic field created by such a current is measured.

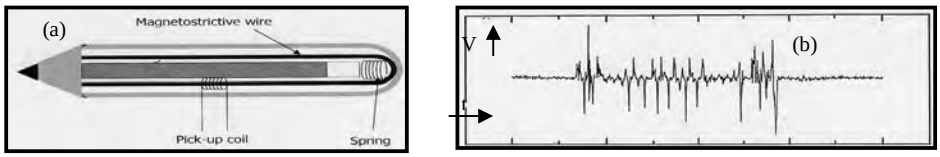

Figure 3.- Schematic view of a magnetoelastic pen (a) based on the stress dependence of GMI and a typical magnetoelastic signature (b).

Other family of sensor devices make use of the stress impedance. In these cases stress sensors are developed, as tensile, bending or torsion sensors. This family of sensors include also a magnetoelastic pen for authentication of signatures (figure 3), or curvature sensor in household electrical appliances.

In the lecture, different aspects about the giant magnetoimpedance effect will be considered from the definition and origin of GMI effect, the materials that suit better to design the GMI effect, their characteristics and phenomenology, and finally their applications in various sensor families.

REFERENCES

1. Giant Magnetoimpedance, Handbook of magnetic materiasl, M. Knobel, M. Vazquez and L. Kraus, ed. K.H.J. Buschow, Vol 15, Chapter 5, 2003, pp. 497-563. Elsevier, 2003
2. Magnetic Sensors and Magnetometers, P. Ripka and L. Kraus ed. Artech House, 2001, pp 349-367
3. See special issue of J. Magn. Magn. Mat. 249 (2002) devoted to the International Workshop on Magnetic Wires and Applications, San Sebastián (Spain) 2001.
4. Kamruzzaman Md., I.Z. Rahman, J. Mater Proc Techn. 119 (2001) 312
5. M. Knobel and K. Pirota, J. Magn. Magn. Mater 242-245 (2002) 33

STUDIA UNIVERSITATIS BABEŞ-BOLYAI, PHYSICA, LII, 1, 2007

THE MAGNETIC MICROSTRUCTURE OF NANOSTRUCTURED MATERIALS

RUDOLF SCHÄFER*

A review is given on the magnetic microstructure and magnetization processes of modern fine- and nanocrystalline magnetic materials, based on Kerr-microscopical domain observation. The grain size dependence of coercivity together with typical domain images is summarized in Fig. 1. In coarse-grained material the domain character is determined by the surface orientation of the individual grains [1]. The rising influence of grain boundary domains with decreasing grain size is responsible for the characteristic 1/D dependence of coercivity. For grain sizes in the 100 nm regime, coercivity shows a maximum that can be applied for hard magnets. Immobile, patchy domains are characteristic for this regime. With further decreasing grain size, coercivity drastically falls of with D^6, leading to extremely soft magnetic nanocrystalline and finally amorphous material. Residual anisotropies in competition with controllable, macroscopic anisotropies are responsible for the domain character in such materials [1, 2].

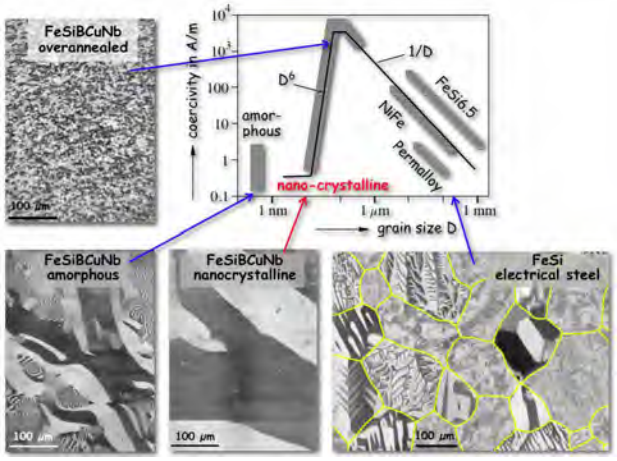

Fig. 1. Coercivity as function of grain size (after [3]) for a number of materials, together with typical domain images

* IFW Dresden, Inst. f. Metallic Materials, Helmholtzstr. 20 , D-01069 Dresden, r.schaefer@ifw-dresden.de

1. Domains in nanocrystalline ribbons

Nanocrystalline FeCuNbSiB ribbons, produced by rapid quenching and annealing, reveal a homogeneous ultrafine grain structure of bcc FeSi with grain sizes of typically 10–15 nm and random orientation, embedded in an amorphous minority matrix [3]. The microstructure leads to a distribution of magnetic anisotropy axes randomly varying their orientation over the scale of the grain size D (Fig. 2). As D is smaller than the ferromagnetic correlation length L_{ex}, the smoothing action of exchange energy impedes the magnetization to follow the local anisotropy axes, i.e. local anisotropies are largely washed out. As the average random anisotropy is negligibly small, the domains are controlled by uniaxial anisotropies (like field- or creep induced anisotropies) that are uniform on a macroscopic scale. Apparently homogenously magnetized domains (see Fig. 1) are therefore observed [4]. The size of uniaxial anisotropy can be controlled by field annealing (also annealing without magnetic field will cause induced anisotropy along the direction of local magnetization of the domains present during annealing).

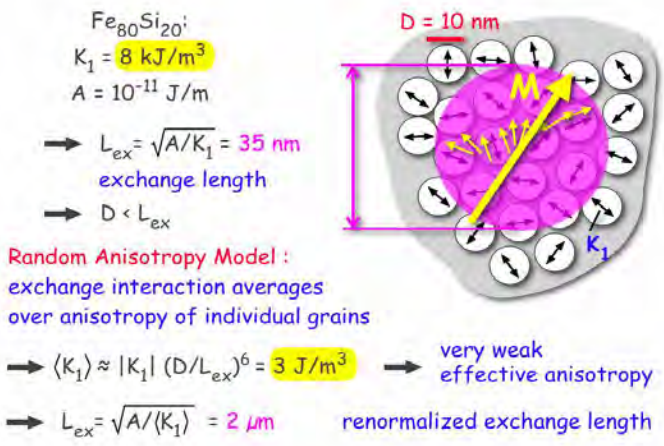

Fig. 2. Visualization of the random anisotropy model in nanocrystalline material. The exchange length L_{ex} represents the characteristic minimum scale below which the direction of magnetization cannot vary appreciably (A and K_1 are exchange and magnetocrystalline anisotropy constants, respectively)

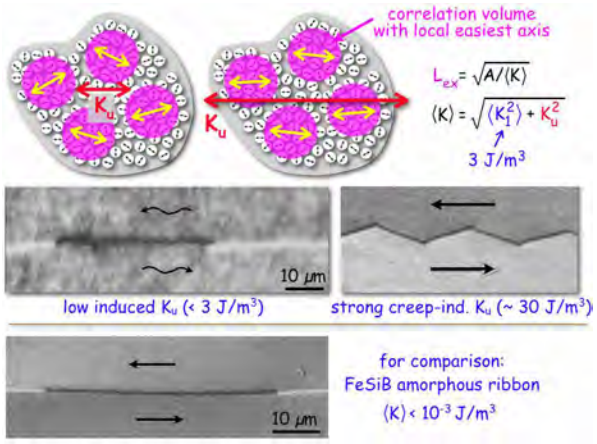

Fig. 3. The interplay of effective random ($<K_1>$) and induced (K_u) anisotropy determines the degree of magnetization modulation on a microscopic scale. Shown are high-resolution observations on $Fe_{73}Cu_1Nd_3Fe_{16}B_7$ nanocrystalline ribbons (20 µm thick) with different strengths of induced anisotropy, as well as an amorphous ribbon for comparison

On a microscopic scale, however, interesting details are revealed that depend on the competition of random and uniform (induced) anisotropy (Fig. 3) [5, 6]. If the uniform anisotropy is larger than the effective random anisotropy, the domains are homogeneously magnetized also on a microscopic scale. For induced anisotropies in the order of or lower than the effective random anisotropy, the magnetization is microscopically modulated in a patch-like way within otherwise regular domains that are oriented along the induced anisotropy direction. These patches are fluctuating on a scale of a few micrometers which is the order of the renormalized exchange length (see Fig. 2). They reflect the angular dispersion of the easiest magnetic axis (given by statistical fluctuations) from one correlation volume to the other.

Domain modulations on the microscopic scale have consequences for magnetization processes (Fig. 4). Whereas for weak modulation (i.e. strong induced anisotropy) the easy axis process is governed by domain wall motion, nucleation-dominated processes are observed for strong modulation (i.e. small induced anisotropy) due to the strong microscopic disorder in magnetization. Correspondingly, homogeneous and inhomogeneous rotational processes, respectively, are observed in hard-axis fields. The modulation has also a strong impact on the dynamic magnetization processes at elevated frequencies. A nucleation-dominated process in observed for strongly modulated material (Fig. 5), while wall motion is found in higher anisotropy material (not shown). In both cases, the domain refinement with increasing frequency is caused be eddy current effects. Interestingly, the material with the smallest induced anisotropy (i.e. strongest modulation) reveals the highest permeability and lowest power loss.

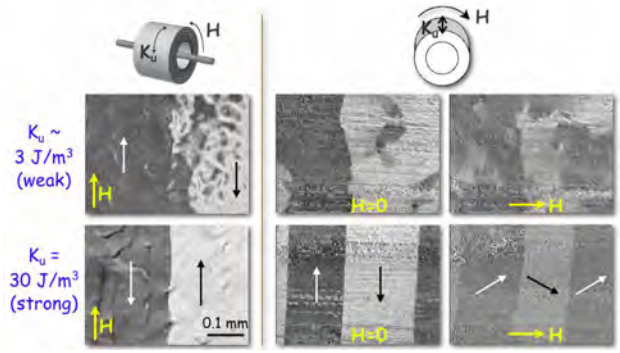

Fig. 4. Easy-axis (left) and hard-axis (right) magnetization processes for two different nanocrystalline FeCuNdFeB ring cores with circumferential and transverse induced anisotropy axis, respectively, of different strengths.

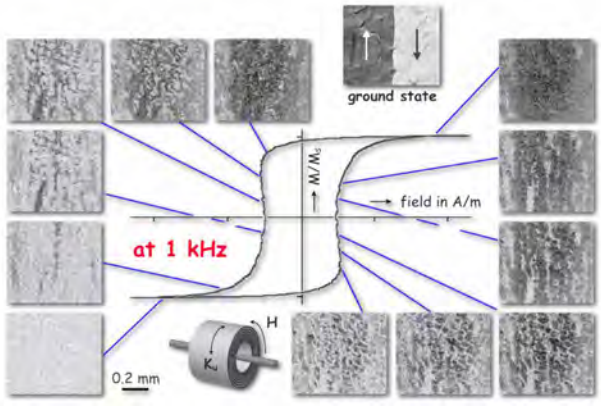

Fig. 5. Stroboscopic observation of the dynamic easy-axis process at 1 kHz on a low-anisotropy nanocrystalline ring core. The regular 180° domains of the ground state are replaced by patch domains at high frequency (after [7]).

According to the random anisotropy model [3], the effective anisotropy constant $\langle K_1 \rangle$ is equal to $|K_1|\sqrt{N}$, where K_1 is the magnetocrystalline anisotropy and N is the number of exchange-coupled grains within the renormalized correlation volume. Consequently, the magnetic microstructure of nanocrystalline ribbons can be modified by either changing K_1 (Fig. 6a, b) or N (Fig. 6c). If the random anisotropy is less effectively averaged out, a patchy and immobile domain structure is observed.

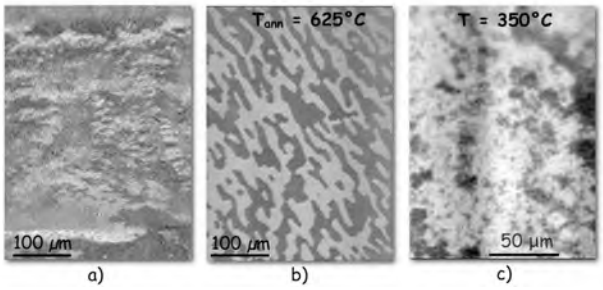

Fig. 6. (a) Adding cobalt to the standard FeCuNdFeB alloy significantly increases the magnetocrystalline anisotropy, leading to a stronger effective anisotropy and immobile patch domains. The $Co_{45}Fe_{28.5}Si_{13.5}B_9Cu_1Nd_3$ ribbon was provided by *Pilar Marin, Madrid*. Patchy domains are also observed in (b), where a regular FeCuNdFeB ribbon was "overannealed". Here Fe_2B precipitates have been formed that have a high magnetocrystalline anisotropy, thus increasing the effective anisotropy although the grain size of the bcc FeSi grains remains unchanged. Image (c) shows patch domains in an optimized FeCuNdFeB ribbon that was heated above the Curie point of the amorphous matrix phase, leading to a reduction of the number of exchange coupled grains (after [6]).

2. Domains in nanocrystalline magnetic films

When nanocrystalline ribbons are thinned to the micrometer regime and below (Fig. 7), the patchy modulation of magnetization changes to a classical ripple pattern with a textured modulation that is well known from thin film magnetism [1]. This indicates that both, ripple and patches are due to the statistical perturbation by the crystal anisotropy, caused by the irregular nanocrystalline microstructure in each case.

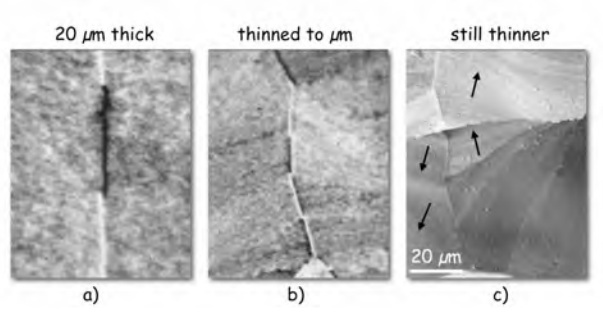

Fig. 7. (a) Patch-like modulated domains in nanocrystalline $Fe_{84}Zr_{3.5}Nb_{3.5}B_8Cu_1$ ribbon (thickness 20 µm), which transform into ripple (b, c) by thinning the ribbon (after [2])

The preference of a textured modulation in the case of films and a patchy modulation for bulk nanocrystalline material, respectively, can be explained by stray field arguments (Fig. 8). Consider two neighborhoods of grains (correlation volumes), in which by statistical fluctuations two local anisotropy axes dominate that are superimposed onto an average (induced) anisotropy axis. If the two neighborhoods are magnetized along different angles ϑ_1 and ϑ_2, a "transverse" magnetic charge $\lambda_{trans} = \sin\vartheta_1 - \sin\vartheta_2$ is generated at the supposed boundary. For small ϑ this charge is much larger than the longitudinal charge $\lambda_{lon} = \cos\vartheta_1 - \cos\vartheta_2$ appearing at the boundary of longitudinally neighbored areas. The stray field energy therefore suppresses lateral variations of magnetization, thus causing ripple texture orthogonal to the average anisotropy axis. This discussion is based on the fact that in thin films the magnetization vector is forced parallel to the film plane by the demagnetizing field. In bulk material, there is the additional freedom of magnetization modulation also in the third dimension. If one correlation volume is magnetized to the left, there can be another one underneath that is magnetized to the right. This leads to a cancellation of transverse magnetization components so that stray fields, which would enforce certain wall orientations, are irrelevant. Arbitrarily oriented walls, i.e. patch domains, are the consequence.

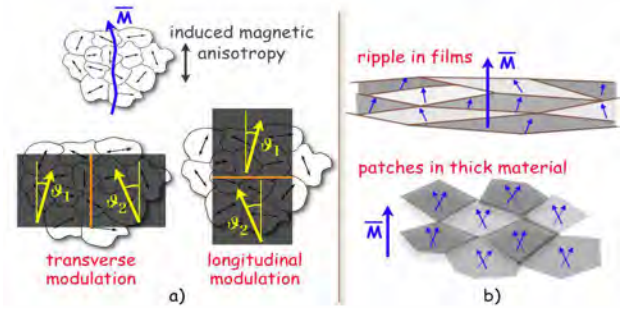

Fig. 8 (a) Stray field argument in favor of longitudinal magnetization ripple in magnetic films. (b) The cancellation of transverse magnetization allows a patchy modulation in case of bulk nanocrystalline material like ribbons. A macroscopic, induced anisotropy, here aligned vertically, was assumed.

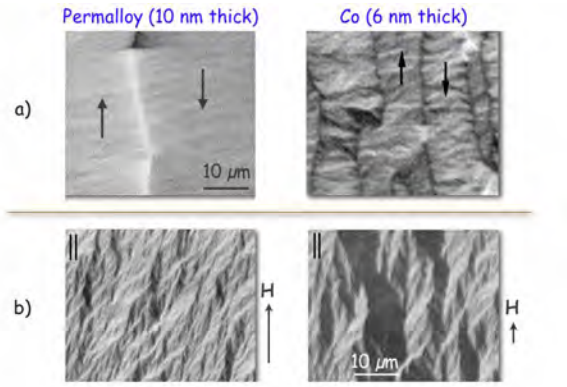

Fig. 9. (a) Polycrystalline Co films with strong magnetocrystalline anisotropy show a stronger ripple effect than Permalloy. (b) The large microscopic dispersion in Co-films leads to a nucleation dominated magnetization process – shown are two domain states in decreasing magnetic field, observed on a 6 nm thick Co-film. All films were prepared by sputtering, thus having a nanocrystalline microstructure

The same arguments as for the nanocrystalline ribbons also apply to films: A stronger magnetocrystalline anisotropy leads to less-effective averaging effects, i.e. a stronger microscopic dispersion of magnetization. Consequently, Permalloy films with their very small crystal anisotropy show a much weaker ripple effect than cobalt films (Fig. 9a). In the latter a strongly nucleation-dominated magnetization process is observed (Fig. 9b).

3. Domains in fine- and nanostructured permanent magnets

The microstructure of common permanent magnets like hexaferrites, NdFeB or CoSm type magnets consists of highly anisotropic grains in the size range of 10 µm in a polycrystalline, textured compound that are prepared in such a way, that the switching of one grain has little influence on its neighbors [1]. Regular domains are observed in such material, the character of which depends on the orientation of the observed surface. But permanent magnets can also be prepared from *single-domain* particles. Classical examples are the *Alnico* alloys, consisting of fine filaments of a high-saturation FeCo alloy that are embedded into a non-magnetic NiAl matrix.

Modern small particle magnets are based on high-anisotropy materials that consist of single-domain *grains*. A number of techniques can be used to prepare fine-crystalline magnets out of precursors such as $Nd_2Fe_{14}B$ [8]: rapid quenching and subsequent crystallization, mechanical alloying, and the HDDR-process. All these methods generate a fine powder with a particle size around 100 µm and a grain size

between some 10 nm and some 100 nm, which then has to be compacted into solid magnets. Oriented magnets can be produced by “die-upsetting”. Also by the HDDR process an anisotropic powder can be produced which can be oriented in a magnetic field.

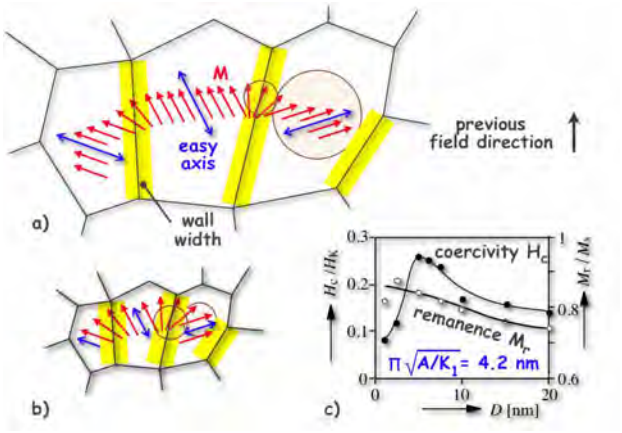

Fig. 10. Mechanism of remanence-enhancement in non-oriented, nanocrystalline NdFeB magnets. The rotational zones around the grain boundaries in the order of the domain wall width contribute to the remanence. Their relative volume increases with decreasing grain size [compare (a) and (b)]. Simulated coercivity and remanence curves are shown in (c) (taken from [9])

But even non-oriented nano-crystalline materials remain interesting as a relatively weak exchange interaction between very small grains can lead to an enhanced remanence without a significant loss in coercivity (exchange enhanced magnets). The coupling enhances the remanence above the average $M_r = 0.5\ M_s$ of independently oriented uniaxial grains (see Fig. 10). A further possibility of achieving high remanence in non-oriented nanocrystalline materials consists in adding a high-saturation soft magnetic phase, which is strongly exchange coupled to the basic hard magnetic phase if the extension of the soft phase is sufficiently small. The coercivity in these two-phase nano-crystalline magnets is dominated by the hard phase, whereas the high remanence is primarily a consequence of the soft phase. A highly irregular magnetic microstructure that is modulated on the scale of the grain size (i.e. of the order of some ten nanometers) is found in such material. It somehow resembles the irregular patch domains of the overannealed FeCuNbSiB ribbons (see Fig. 1), although on a much finer scale due to the higher anisotropy and smaller grain size.

If the exchange coupling between single-domain grains is interrupted, the dipolar interaction between the grains causes *magnetostatic interaction domains* [1] (Figs. 12, 13). They are characterized by grain neighborhoods, in which all grains are correlatively saturated along their individual easy axis along a certain net direction. Interaction domains are the more pronounced the better the texture of the material [12]. Interestingly, such domains have recently also been found in the classical Sm_2Co_{17} pinning magnets, which indicates predominant magnetostatic interaction between the $Sm_2(CoFe)_{17}$ cells that are interrupted by precipitation phases [13].

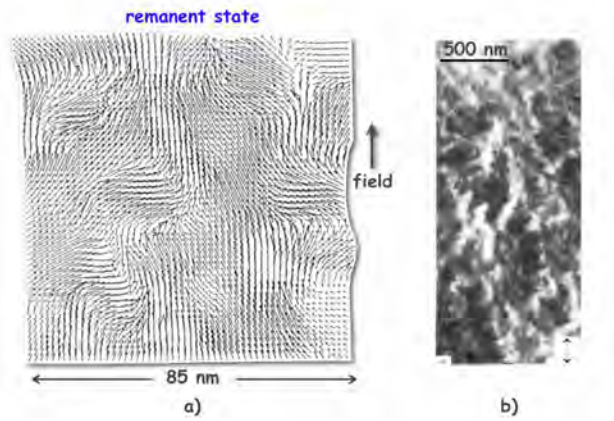

Fig. 11. (a) Finite element simulation of remanance-enhanced $Nd_2Fe_{14}B/Fe_3B$ magnet (taken from [10]). (b) Domain image, obtained by transmission electron microscopy in the Foucault mode, of $Nd_2Fe_{14}B/Fe$ material (taken from [11]).

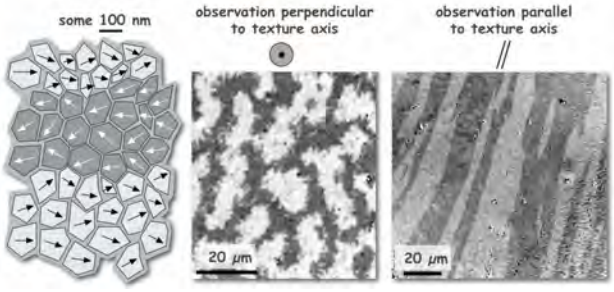

Fig. 12. Magnetostatic interaction domains in fine-crystalline NdFeB material, where the $Nd_2Fe_{14}B$-grains are exchange-decoupled by a paramagnetic grain boundary phase

Note that the „softening-effect“ due to random anisotropy as described in Chap. 1 is irrelevant for nanostructured permanent magnets, even in the case of exchange-coupled grains. The exchange length L_{ex} is 1.3 nm in NdFeB (with $K_u = 4.3 \cdot 10^6$ kJ/m^3 and $A = 8 \cdot 10^{-12}$ J/m), being far below the typical grain size of 20 nm.

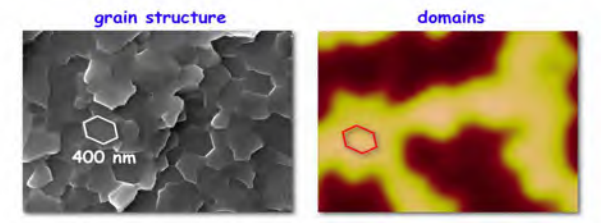

Fig. 13. The comparison between grain structure and interaction domains (here imaged by Magnetic Force Microscopy) directly proves, that the domains extend over several correlated grains (courtesy O. Gutfleisch, taken from [14])

REFERENCES

1. A. Hubert and R. Schäfer: Magnetic Domains. The Analysis of Magnetic Microstructures. Springer, Berlin (1998)
2. R. Schäfer: *Domains in extremely soft magnetic materials*. J. Magn. Magn. Mat. **215-216**, 652-663 (2000)
3. G. Herzer, *Nanocrystalline soft magnetic alloys*. In: Buschow KHJ, editor. Handbook of Magnetic Materials, vol. 10. Elsevier Science B.V., p.415 (1997)
4. R. Schäfer, A. Hubert, G. Herzer: *Domain observation on nanocrystalline material*. J. Appl. Phys. **69**, 5325 (1991)
5. G. Herzer: *Anisotropies in soft magnetic nanocrystalline alloys*. J. Magn. Magn. Mat. **294**, 99-106 (2005)
6. S. Flohrer, R. Schäfer. Ch. Polak, G. Herzer: *Interplay of uniform and random anisotropy in nanocrystalline soft magnetic alloys*. Acta Materialia 53, 2937-2942 (2005)
7. S. Flohrer, R. Schäfer. J. McCord, S. Roth, G. Herzer, L. Schultz: *Magnetization loss and domain refinement in nanocrystalline tape wound cores*. Acta. Mat. 54, 3253-3259 (2006)
8. O. Gutfleisch, A Bollero, A. Handstein, D. Hinz, A. Kirchner, A. Yan, K.-H. Müller, L. Schultz: *Nanocrystalline high performance magnets*, J. Magn. Magn. Mat. 242-245, 1277-1283 (2002)

9. W. Rave and K. Ramstöck: *Micromagnetic calculation of the grain size dependence of remanence and coercivity in nanocrystalline permanent magnets*, J. Magn. Magn. Mat. 171, 69-82, (1997)
10. T. Schrefl and J. Fidler: *Finite element modeling of nanocomposite magnets*. IEEE Trans. Magn. 35, 3223 (1999)
11. J.N. Chapman, S. Young, H.A. Davies, P. Zhang, A. Manaf, R.A. Buckley: *A TEM investigation of the magnetic domain structure in nanocrystalline NdFeB samples*. Proc. 13th Int. Workshop on RE Magnets & their applications, p.95, Birmingham (1994)
12. K. Khlopkov, O. Gutfleisch, R. Schäfer, D. Hinz, K.-H. Müller, L. Schultz: *Interaction domains in die-upset NdFeB magnets in dependence on the degree of deformation*. J. Magn. Magn. Mat. 272-276, E1937-E1939 (2004)
13. O. Gutfleisch, K.-H. Müller, K. Khlopkov, M. Wolf, A. Yan, R. Schäfer, T. Gemming, L. Schultz: *Evolution of magnetic domain structures and coercivity in high-performance SmCo 2:17 type permanent magnets*, Acta Materialia **54**, 997-1008 (2006)
14. K. Khlopkov, O. Gutfleisch, D. Hinz, K.-H. Müller and L. Schultz, "*Evolution of interaction domains with texture in Nd2Fe14B studied with magnetic force microscopy*", J. Appl. Phys., accepted.

STUDIA UNIVERSITATIS BABEŞ-BOLYAI, PHYSICA, LII, 1, 2007

MEMS: AN OVERVIEW

NORA M. DEMPSEY*

1) What are MEMS?

Micro-Electro-Mechanical-Systems (MEMS) are machines which range in size from a micrometre to a millimetre (Figure 1). They may function as actuators, motors, generators, switches, sensors…. and have applications in fields as diverse as telecommunications, automotive and aerospace, astronomy and ophthalmometry, biotechnology, logistics…

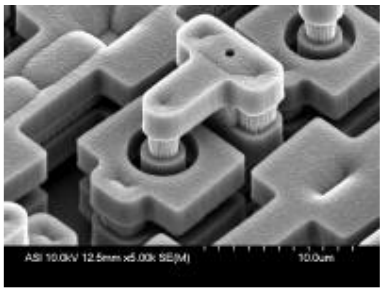

Figure 1a: MEMS Post Style Actuator

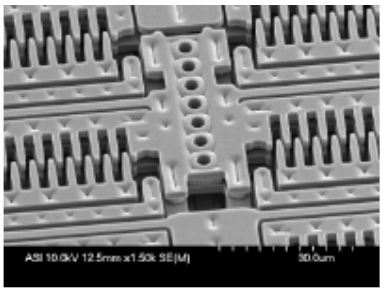

Figure 1b: Large Force Electrostatic MEMS Comb Drive (http://www.memx.com/products.htm)

Common examples include:
- inkjet printers
- accelerometers (airbag deployment…)
- gyroscopes (trigger dynamic stability control…)
- pressure sensors (car tires, blood…)
- displays (projectors…)
- optical switching technology (telecommunications)
-Bio-MEMS (Lab-On-Chip, MicroTotalAnalysis…)

2) Why are MEMS of interest?

MEMS are of interest for many reasons:

COST: Batch processing of MEMS using techniques developed by the microelectronics industry means that the price of an individual machine is very low (some costing no more than a few cents !).

* Institut Néel, CNRS/UJF, Grenoble, France

SIZE: Their small size means that they don't take up much space and weigh little, with obvious benefits for portable applications (mobile phones, aerospace devices…) or applications with space limitations (implantable devices, micro-surgery,…..).

ENERGY EFFICIENCY: MEMS hold great potential for the environment: they already increase fuel efficiency in modern cars and houses of the future will intelligently control energy consumption, by exploiting MEMS to regulate temperature and lighting in accordance with need (ambient temperature + human presence).

INTELIGENT MACHINES: As MEMS are made using microelectronics technology, electro-mechanical elements can be integrated with electronics onto one substrate, the former acting as the arms and legs of the machine, the latter as the brain.

REDEFINING WHAT IS POSSIBLE: MEMS challenge traditional engineering concepts, as gravity and inertia are of reduced importance and atomic forces and surface science may dominate. Scaling laws demonstrate that effects not exploitable at the macro-scale can become of interest at the micron-scale.

3) How are MEMS made?
There are a number of different categories of MEMS technologies:

1) Bulk Micromachining:
Bulk micromachining creates devices by wet etching into a wafer, typically Si.

2) Surface Micromachining:
Surface Micromachining builds devices up from the wafer layer-by-layer.
It requires more fabrication steps than Bulk Micromachining, and thus it is more expensive. However it enables the creation of more sophisticated devices of higher functionality.

3) LIGA:
LIGA is a relatively inexpensive fabrication technology which uses x-ray lithography to create small, but relatively high aspect ratio devices.

4) Deep Reactive Ion Etching:
Deep Reactive Ion Etching micromachining uses a plasma etch to create features. It is more expensive but also more flexible than traditional Bulk Micromachining based on wet etching.
These different categories use three basic building blocks:

I – Deposition
II - Lithography
III - Etching

I – Deposition
Deposition technology may be classified as **chemical** (Chemical Vapor Deposition, Electrodeposition, Epitaxy , Thermal oxidation…) or **physical** (Physical Vapor Deposition, Casting…).
II - Lithography
Lithography concerns the transfer of a pattern to a photosensitive material by selective exposure to a radiation source, the wavelength of which determines the achievable feature size.
III – Etching
Etching processes are classified as "wet" when a chemical solution is used to etch the material or "dry" when material removal is achieved by sputtering or dissolution using reactive ions or a vapour phase etchant.

4) What materials are used in MEMS?

MEMS are made using a number of different materials, the choice depending on the functionality required and cost limitations. The tree main categories are:
- Silicon
Silicon is used in a wide variety of MEMS because of its intrinsic physical properties and the fact that its structuring is well mastered, thanks to its use in the microelectronics industry.
- Polymers
Polymers are used because they are relatively cheap and can show a great variety of material characteristics.
- Metals
Common metals such as Gold, Nickel, Aluminum, Chromium, Titanium, Tungsten, Platinum and Silver are used in many MEMS. More exotic metallic materials are exploited for very particular functionalities (see below).

5) What are the physical principles exploited in MEMS?

Many different physical principles are exploited in MEMS. Owing to the fact that MEMS is an off-shoot of the microelectronics industry, the first MEMS were based on ***electrostatic*** principles. Following this, ***differential thermal expansion*** was exploited in bimorph actuators. Today's MEMS also exploit ***piezoelectricity, electromagnetism, ferromagnetism, magnetostricition, shape memory effects***…. MEMS is a fast evolving domain and it is expected that other effects will also be exploited.

6) From MEMS to NEMS

Nanotechnology is advancing at such a rate that what is achieved at the micron scale is or soon will be achievable at the nanometre scale, extending the field to nano-electro-mechanical systems (NEMS). This evolution to ever smaller sizes will reinforce the above mentioned advantages of MEMS, and should even allow the exploitation of quantum effects.

STUDIA UNIVERSITATIS BABEŞ-BOLYAI, PHYSICA, LII, 1, 2007

MAGNETIC MEMS

NORA M. DEMPSEY*

1) Why are magnetic MEMS of interest?

Micro-Electro-Mechanical-Systems (MEMS) are devices of sub-mm dimensions integrating various components (mechanical elements, sensors, actuators) and electronics on a common substrate (typically Si). They are progressively permeating our everyday lives, mainly in the form of micro-sensors (pressure, temperature, contact, chemical, gyroscopes etc…) and have applications in many fields including automotive, air-and-space, industrial processing and biotechnology. The potential impact of MEMS actuators has not yet been realised because their output forces, torques and energy densities are much limited by the mainly electrostatic principles upon which today's systems are based. Micro-actuators incorporating magnetic materials and based on magnetic actuation principles provide a number of advantages over electrostatic actuators, namely low voltage and power consumption combined with large actuation forces over relatively long distances. However their emergence has been limited by the non-availability of high quality magnets of the appropriate size.

2) Which magnetic materials for MEMS?

A variety of magnetic materials have potential applications in magnetic MEMS including familiar hard and soft materials as well as more exotic magnetostrictive, thermo-reversible and shape memory materials. While soft materials such as permalloy (FeNi) are relatively easy to prepare in film form by electrodeposition and sputtering, the processing of the other materials is more challenging. The core of this lecture will deal with the preparation of high performance hard magnetic materials based on rare-earth transition metal (RE-TM) alloys (NdFeB, SmCo) or $L1_0$ alloys (FePt, CoPt).

3) Preparation of μ-magnets

Various routes which have been used to prepare μ-magnets are listed in Table 1.

* Institut Néel, CNRS/UJF, Grenoble, France

Table 1. Techniques used to prepare µ-magnets.

Top-down Routes	Bottom-up (deposition) Routes
Machining of bulk magnets	Electro-deposition
Screen printing, tape casting and bonding	Plasma spraying
Mechanical deformation	Pulsed Laser Deposition (PLD)
	Sputtering

All routes have their advantages and disadvantages. A number of factors will determine the choice of preparation technique including:
- ***Process-material-compatibility***
- ***integratability into the overall micro-fabrication process***
- ***compatibility of substrates and buffer/capping layers with overall micro-fabrication process***
- ***thermal compatibility*** of the material with the substrate

3-i) Top-down preparation techniques

Machining of bulk magnets

This technique is presently used to prepare magnets for application in milli-systems (wrist watches, flip-dot displays, heart catheters...). There is a lower limit to the magnet thickness achievable by micro-machining (ca 150 µm for RE-TM magnets). High quality RE-TM magnets may suffer surface-degradation during micro-machining, resulting in the loss of coercivity of the surface layer, and thus the overall magnet remanence.

Screen printing, tape casting and bonding

Screen printing and tape casting are well adapted to fabricate isotropic films with thicknesses in the range of 0.1-1 mm. In the case of screen printing, the permanent magnetic thick film can be deposited directly onto the micro-system components.

Mechanical deformation

Cyclic mechanical deformation can be used to prepare foils of typical thickness 100 µm. Hot-deformation can be used to die-upset magnets down to thicknesses of several hundreds of microns.

3-ii) Bottom-up preparation techniques

Electro-deposition
Electro-deposition can be used to deposit certain materials at rates of up to a few µm/h over large areas. It is a technique already used in MEMS processing.

Plasma spraying
Plasma spraying is a rapid solidification technique in which alloy powder is injected into a very high temperature plasma flame and then projected onto a surface. It is suitable for the preparation of thick films ($\leq$ 1 mm).

Pulsed Laser Deposition (PLD)
PLD can be used to prepare films. However deposition rates tend to be low and deposited surfaces small.

Sputtering
Sputtering can be used to prepare films. Deposition rates and film surface areas depend strongly on the type of sputtering tool and target size. Triode sputtering is adapted to high deposition rates over large surfaces.

3-iii) A case study: high rate sputtering of thick hard magnetic films

Based on encouraging literature reports, and the fact that sputtering is one of the most promising routes for the integration of high quality magnets into MEMS, a high rate triode sputtering chamber was developed at Institut Néel. In our case, Si substrates are used so as to be compatible with local micro-technology platforms. The deposition of three high performance hard magnetic materials, NdFeB, SmCo and FePt has been studied. Thick films (5-50 µm) were deposited at deposition rates of up to 20 µm/h. The influence of deposition temperature on the magnetic and structural properties of films in the as-deposited and post-deposition annealed states will be presented. The extrinsic magnetic properties (coercivity, remanence) depend strongly on the substrate temperature during deposition. NdFeB films can be prepared with out-of-plane texture while the SmCo films can be prepared with in-plane texture.

4) Structuring of µ-magnets

A number of different routes which have been used to pattern permanent magnet films are schematized in figure 1. The patterns produced can be categorized as i) *topographic* or ii) *crystallographic*. The topographically patterned films can be further categorized as patterned either *during deposition* or *post-deposition*. The cross section of a 5 µm thick NdFeB film deposited on a pre-patterned substrate is shown in figure 2.

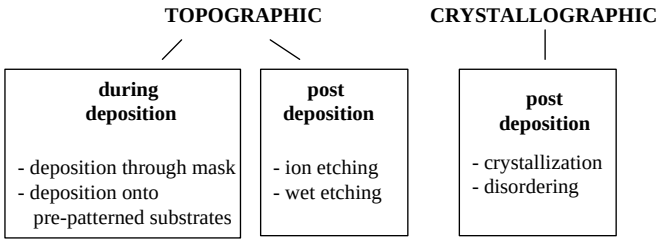

Figure 1. Overview of different routes used to pattern permanent magnet films.

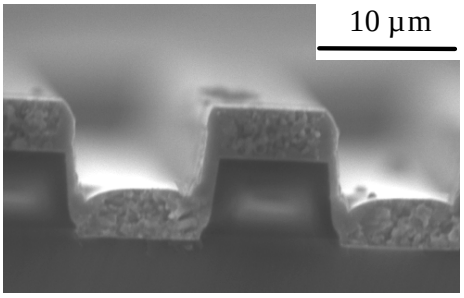

Figure 2. Cross sectional SEM image of {Ta(100 nm) / NdFeB (5 µm) / Ta (100 nm)} deposited onto a pre-patterned Si/SiO substrate.

The second, and less conventional type of patterning, involves the local modification of the film's magnetic properties through a change in its crystallographic state. In this case a modulation in the magnetic properties is achieved without a modulation in the film's surface height.

5) Proto-type magnetic MEMS

A number of proto-type magnetic MEMS (µ-motors, µ-generators, bistable µ-switches..) will be reviewed. The use of micro-magnet arrays for levitation of small particles, which demonstrates the potential for magnetic lab-on-chip systems, will be presented.

STUDIA UNIVERSITATIS BABEŞ-BOLYAI, PHYSICA, LII, 1, 2007

PREPARATION AND CHARACTERISATION

JULIA LYUBINA[*]

Modern high performance magnets are based on nanocrystalline materials. The excellent magnetic properties of these materials are determined by a specific chemical and phase composition and, to a great extent, by a particular nanometer-scale (crystallite sizes in the range of 10^1 - 10^2 nm) microstructure. Therefore, one on the most important stages for the development and optimisation of nanocrystalline magnetic materials is the study of the structure as well as the understanding of the phase formation mechanisms in these materials. Here, preparation and characterisation of magnetic bulk nanocrystalline materials is reviewed (for the preparation of film systems see e.g. the presentations by N. M. Dempsey, J. Bachmann). Principle synthesis methods including mechanical ball milling, melt spinning and hydrogen-assisted processing are applied to R-Fe-B (R = Nd, Pr) and Fe-Pt alloys with the aim to produce permanent magnets with a high remanence and high coercivity. The use of x-ray diffraction for the study of the structure as well as advanced microstructure imaging techniques is discussed. Differential scanning calorimetry (DSC) is applied for the study of phase transformations and for the analysis of the thermal properties of the materials.

1. PREPARATION

1.1. Mechanical ball milling

Mechanical alloying, or more generally mechanical ball milling, is the process when mixtures of powders (of different metals or alloys/compounds) are milled together. Frequently the term *mechanical alloying* is used to emphasise the fact that material transfer is involved during processing, whereas milling of (already alloyed) powders having uniform composition with the aim of e.g. crystallite size reduction and/or mechanically inducing other transformations is termed *mechanical milling* [1]. Mechanical alloying is a complex process and involves the optimisation of a number of variables to achieve a desired structure, phase composition and microstructure. The most important parameters are: type of mill, milling container, milling time and speed, type and size of the grinding medium, ball-to-powder weight ratio, milling atmosphere, process control agents and temperature of milling.

[*] IFW Dresden, Institute for Metallic Materials, P.O. Box 270016, 01171 Dresden, Germany, j.lyubina@ifw-dresden.de

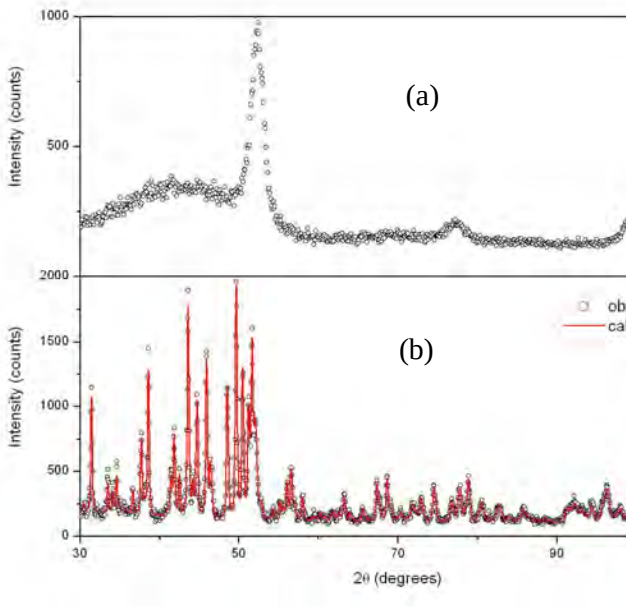

Fig. 1. X-ray diffraction pattern of an alloy with the composition close to $Nd_2Fe_{14}B$ milled in a planetary ball mill for 60 h (a) and an example of a Rietveld refinement plot for this alloy after subsequent heat treatment at 650°C/30 min. Open circles and the full line represent observed and calculated x-ray diffraction profiles, respectively.

Mechanical alloying of elemental Nd, Fe and B powders leads to the formation of a layered microstructure of Fe and Nd with B particles remaining undeformed and embedded in the interfaces [2]. In contrast, mechanical ball milling of the $Nd_2Fe_{14}B$ compound crushed into coarse powder, sometimes with the additional elemental Fe or Co powders, leads to the formation of a mixture of an amorphous phase and nanocrystalline Fe (Fig. 1a). In both methods, heat treatment at relatively low annealing temperatures of 600-700 °C and short reaction times of 5-30 min are required for the formation of the hard magnetic $Nd_2Fe_{14}B$ phase (Fig. 1b), which is due to the extremely fine distribution of the reactants.

A variation of milling is *cryomilling* in which the milling operation is carried out at cryogenic temperatures. The method is indispensable for processing powders of ductile components, where the effect of cold welding between the powder particles and the grinding medium should be minimised. It allows to avoid the use of process control agents often leading to powder contamination. This method has been successfully used to prepare nanocrystalline Fe-Pt (x = 40-60) alloys [3].

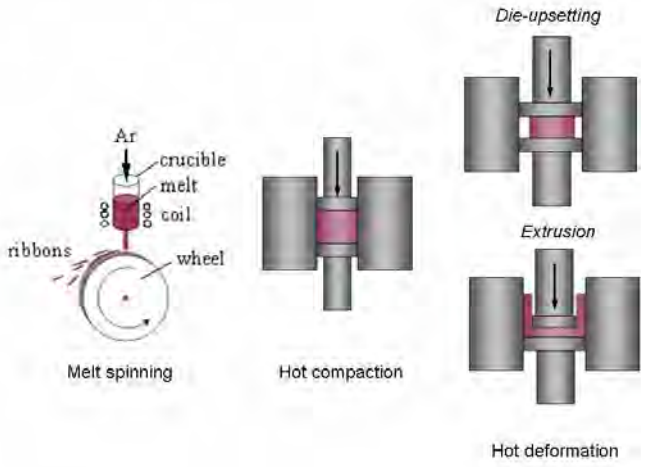

Fig. 2. Schematic representation of the melt spinning, hot compaction and hot deformation techniques.

1.2. Melt spinning

In the melt spinning method, a molten alloy is injected through an opening of a crucible onto a rapidly rotating wheel, as a rule, made out of material heaving high heat conductivity (Fig. 2). During this process solidification rate may reach about 10^5-10^6 K/s and, as a result, ribbons or flakes (due to high brittleness Nd-Fe-B ribbons are frequently fragmented) with thickness of about 30-50 μm are thrown off the wheel surface. The process is usually carried out in inert atmosphere (e.g. Ar or He).

The structure and magnetic properties of rapidly quenched Nd-Fe-B alloys depend on the quenching rate, which is determined by the wheel rotation speed, injection conditions (type and pressure of the inert gas, crucible opening size, distance between the crucible and the wheel etc.) and temperature of the melt. The method mostly used for the production of rapidly quenched Nd-Fe-B alloys is "overquenching" followed by heat treatment during which coercivity is developed. By overquenching materials with partially amorphous structure, similar as that shown in Fig. 1a, are obtained. Optimally annealed overquenched Nd-Fe-B ribbons have grain structure with crystallite size in the range of 20-50 nm, i.e. below critical single-domain particle size of the $Nd_2Fe_{14}B$ compound (200-300 nm [4]). This method is applied for commercial production of magnet powders suitable for the manufacture of bonded magnets.

1.3. Hot deformation

Nd-Fe-B materials produced by the melt spinning and by mechanical ball milling are magnetically isotropic. Therefore, in the absence of exchange coupling between crystallites, the remanence-to-saturation ratio M_r/M_s is limited to 0.5 [5]. One of the methods for obtaining anisotropic magnets with maximised energy density from nanocrystalline Nd-Fe-B alloys is the hot deformation (Fig. 2). Prior to the hot deformation a highly dense almost isotropic precursor is obtained by the hot compaction (T = 675-750 °C). A grain alignment along the c-axis of the tetragonal $Nd_2Fe_{14}B$ phase (easy magnetisation direction) perpendicular to the plastic flow is achieved after high temperature (700 -800 °C) compressive deformation (die-upsetting). The key for the hot workability is the presence of a rare earth rich grain boundary phase, which is liquid at the deformation temperature. Alternatively, hot extrusion may be performed, which results in obtaining ring magnets with a radial texture.

1.4. Sintering

Sintering is a conventional powder metallurgy method for the production of textured $Nd_2Fe_{14}B$-type and $Sm(Co,Cu,Fe,Zr)_z$ magnets. Because the compositions of recent high energy density Nd-Fe-B magnets are close to stoichiometry, conventionally cast materials would contain a high proportion of Fe-dendrites due to the peritectic nature of the formation of the $Nd_2Fe_{14}B$ phase. Fe is detrimental to the crushability during jet milling and to the magnetic properties of the magnet. The “strip casting” method, in which alloys are cast onto a rotating water-cooled wheel, suppresses the formation of free α-Fe and leads to a fine grained microstructure with grain sizes ranging from 5-60 μm. Pulverisation is usually achieved by jet milling where an ultrasonic flow of inert gas induces mechanical collisions of the particles. The particles are subsequently aligned in large magnetic fields (~ 1 MA/m), densified and subjected to the liquid-phase sintering (at around 1000 °C). Anisotropic, sintered $Nd_2Fe_{14}B$-type magnets with energy products (BH)max exceeding 400 kJ/m^3 are now produced routinely in industry using these techniques.

1.5. Hydrogen-assisted processing methods

Hydrogen Decrepitation

Hydrogen decrepitation is usually used in the production of fully dense sintered Nd-Fe-B magnets. Decrepitation means the self-pulverisation of large metal particles into powder. It relies on the fact that the bulk alloy consists of the matrix phase, $Nd_2Fe_{14}B$, and a Nd-rich, grain boundary eutectic which readily absorbs hydrogen at room temperature and at hydrogen pressures < 1 bar. This results in the formation of neodymium hydride and the subsequent differential expansion results in the decrepitation of the bulk material. The initial failure is predominantly intergranular in nature and the exothermic nature of the reaction causes the alloy to heat up and hydrogen is absorbed subsequently by the matrix phase to form a $Nd_2Fe_{14}BH_x$ solution.

HDDR

The Hydrogenation Disproportionation Desorption Recombination (HDDR) process is a strikingly simple method for producing magnetically highly coercive rare-earth transition metal powders (e.g. of $Nd_2Fe_{14}B$-type) by utilising a fully reversible hydrogen gas-induced chemical reaction. Unlike the HD-process, the HDDR route involves heating the bulk alloy in around 1 bar of hydrogen to about 800 °C. The first stage of the HDDR-process is the absorption of hydrogen by the Nd-rich phase at the grain boundaries essentially to form $NdH_{2.7}$. The next stage is the formation of the $Nd_2Fe_{14}BH_x$ interstitial solution. This is followed by a complete hydrogen desorption with further increasing temperature before the disproportionation reaction is triggered. In the case of $Nd_2Fe_{14}B$, the HDDR reaction can be described as:
$Nd_2Fe_{14}B + (2 \pm x)\ H_2 \Leftrightarrow 2NdH_{2 \pm x} + 12Fe + Fe_2B \pm \Delta H$. As in mechanically alloyed or melt spun materials, the coercivity in HDDR processed materials arises from the fact that final grain sizes are significantly smaller than or comparable to the critical single-domain grain size. The crucial difference, however, to the former two methods is that with the HDDR process it is possible to produce directly highly anisotropic magnet powders without the mechanical deformation necessary for example for melt-spun materials. Here "anisotropic powder" means that the magnetically easy axes (c-axes) of the $Nd_2Fe_{14}B$ grains are aligned in the multigrain powder particles. Consequently, compact textured magnets can be produced by aligning these anisotropic powder particles in a magnetic field.

2. CHARACTERISATION

2.1. X-ray diffraction

The purpose of this presentation is to illustrate the potential of x-ray powder diffraction in materials characterisation and give a brief description of the methods for the determination of the phase composition, microstructure parameters (crystallite size and lattice strain) and chemical ordering.

Traditionally phase identification is based on a comparison of the observed data with interplanar spacings *d* and relative intensities *I* of known phases. Quantitative phase analysis assumes that the integrated intensity of Bragg reflections is proportional, among all the intensity factors, to the volume fraction of a phase in a multi-phase mixture. The analysis is, however, extremely complicated or not possible at all when a severe overlap of diffraction peaks and/or peaks of different phases occurs. For instance, in the case of Nd-Fe-B alloys, x-ray structure analysis is complicated due to several reasons: in the Nd-Fe-B system the formation of several equilibrium and non-equilibrium phases is possible. Due to low crystal symmetry and large lattice constants, x-ray diffraction patterns contain a large number of overlapping diffraction lines, often of low absolute intensity (Fig. 1). In

$L1_0$-based alloys, diffraction lines of the phases suffer from a severe overlap due to the nanocrystalline nature of the materials and/or rather close cell dimensions [7]. Evidently, these reasons complicate an extraction of detailed crystal structure information as well. Hence, the determination of peak position and intensity independently of each other is not an appropriate approach in these cases.

An advanced method for analysing diffraction data was proposed by Rietveld [8, 9]. It is based on a whole-pattern fitting with parameters of a model function depending on the crystallographic structure, instrument features and some numerical parameters. With such an approach, even the overlapping peaks contribute information about the structure to the refinement. The aim of the Rietveld analysis is to find a set of parameters that describe the observed diffraction pattern as good as possible. These include lattice constants, phase fraction, degree of texture, site occupation parameters (used for the determination of the degree of chemical order) and profile broadening parameters.

The broadening of x-ray diffraction lines arises due to both physical (specimen-related) and instrumental (geometrical) factors [10, 11]. Once the instrumental broadening is "removed", the analysis of the physically broadened line profile can be made. In general, the physical broadening contains contributions from the small size of the crystallites (coherently scattering domains) and lattice strain (often denoted as microstrain or lattice distortion) caused by e.g. the presence of lattice defects. In order to separate the contributions from crystallite size and lattice strain to the overall breadth the modified Williamson-Hall analysis [12], the so-called "average size-strain" method of Langford [13] can be applied.

Neutron diffraction can also be used for the characterisation of materials [14]. As compared to x-rays, neutrons offer the advantage of being weakly absorbed by materials, i.e. their penetration depth is large, in the order of centimetres. The neutron scattering amplitude does not show a strong dependence on the atomic number, thus providing a possibility to locate light atoms or distinguish neighbouring atoms in the periodic table. Moreover, the interaction of the magnetic moment of neutrons with unpaired electrons enables the investigation of magnetic structures.

2.2. Differential scanning calorimetry

A critical step towards understanding the phase formation in various materials is to characterise their thermal properties [15, 16]. Differential scanning calorimetry (DSC) has proven to be a very useful tool in this effort. By determining the rate of heat flow into a sample, DSC provides quantitative thermodynamic and kinetic information about physical or chemical changes occurring in the material. The latter alter the enthalpy and/or heat capacity of the material, which in turn results in the release or the absorption of heat. Thus, DSC enables determination of transition temperatures and transition heats of such processes as melting, crystallisation,

solid-state transitions, chemical ordering, spin-reorientation transitions, chemical reactions etc. as well as kinetics of these processes (e.g. Kissinger method [17, 18]). Also second order-type transitions, such as ferromagnetic Curie transition, can be detected by abrupt variations in heat capacity.

2.3. Imaging techniques

In electron microscopy, a focused beam of electrons is used to examine objects on a very fine scale. This examination can yield information about topography, microstructure, chemical composition and crystallographic information. Whereas transmission electron microscopy (TEM) is applied for the investigation of very thin samples with resolution down to atomic scale, scanning electron microscopy (SEM) can be used for imaging surface features of massive samples. The process of image formation is fundamentally different between the two techniques; for more details the reader is referred to Ref. [19]. In contrast to TEM, sample preparation for SEM is less complicated. At the same time, high resolution SEM allows observation of crystallites in the range of about 20-30 nm [7, 20]. Secondary electron mode in SEM provides a three-dimensional perspective, whereas the use of backscattered electrons allows detecting the contrast between areas with different chemical compositions.

Atomic force microscopy (AFM) is another scanning probe technique. It relies on attractive forces that are generated between electron clouds of atoms of a specimen and a vibrating cantilever, when these are brought in close proximity, and yields information about sample topography. AFM can be used for imaging non-conductive samples at near-atomic resolution. Magnetic force microscopy (MFM) relies on a principle similar to AFM. The MFM technique is based on the detection of the magnetostatic interaction between a sample and a small ferromagnetic tip and is used for observation of magnetic domains [21].

REFERENCES

1. C. Suryanarayana, *Mechanical alloying and milling*, Prog. Mater. Sci. 46 (2001) 1.
2. L. Schultz, J. Wecker, E. Hellstern, *Formation and properties of NdFeB prepared by mechanical alloying and solid-state reaction*, J. Appl. Phys. 61 (1987) 3583.
3. J. Lyubina, O. Gutfleisch, R. Skomski, K.-H. Müller, L. Schultz, *Phase transformations and thermodynamic properties of nanocrystalline FePt powders*, Scr. Mater. 53 (2005) 469.
4. K.H.J. Buschow, *New permanent magnet materials* (North-Holland, Amsterdam, 1986).
5. E. P. Wohlfarth, *Relations between different modes of acquisition of the remanent magnetisation of ferromagnetic particles*, J. Appl. Phys. 29 (1958) 595.

6. J. Lyubina, I. Opahle, K.-H. Müller, O. Gutfleisch, M. Richter, M. Wolf, L. Schultz, *Magnetocrystalline anisotropy in $L1_0$ FePt and exchange coupling in FePt/Fe_3Pt nanocomposites*, J. Phys.: Condens. Matter 17 (2005) 4157-4170.
7. H. M. Rietveld, *A profile refinement method for nuclear and magnetic structures*, J. Appl. Cryst. 2 (1969) 65.
8. R. A. Young (editor), *The Rietveld Method* (Oxford University Press, Oxford, UK, 1993).
9. B. E. Warren, *X-ray Diffraction* (Dover Publications, Inc., NY, 1990).
10. C. Suryanarayana and M. Grant Norton, *X-ray Diffraction: A Practical Approach* (Plenum Press, NY, 1998).
11. K. Williamson and W. H. Hall, *X-ray line broadening from filed aluminum and wolfram*, Acta Metall. 1 (1953) 22.
12. J. I. Langford, *The use of the Voigt function in determining microstructural properties from diffraction data by means of pattern decomposition*, in Proc. Int. Conf.: Accuracy in powder diffraction II edited by E. Prince and J.K. Stalick (NIST Special Publication No. 846, U.S. Government Printing Office, Washington, DC, 1992), p. 110.
13. J. Baruchel, J. L. Hodeau, M. S. Lehmann, J. R. Regnard, C. Schlenker (editors), *Neutron and Synchrotron Radiation for Condensed Matter Studies* (Springer Verlag, Berlin, Germany, 1993).
14. R. W. Cahn, P. Haasen, E. J. Kramer (editors), *Materials Science and Technology. Vol. 2A: Characterisation of Materials, Part I* edited by E. Lifshin (VCH Verlagsges. mbH, Weinheim, 1992).
15. M. E. Brown (editor), *Introduction to Thermal Analysis: Techniques and Applications* (Kluwer Academic Publishers, Dordrecht, 2001).
16. H. E. Kissinger, *Reaction kinetics in differential thermal analysis*, Analytical Chem. 29 (1957) 1702.
17. J. Lyubina, O. Isnard, O. Gutfleisch, K-H. Müller, L. Schultz, *Ordering of nanocrystalline Fe-Pt alloys studied by in-situ neutron powder diffraction*, J. Appl. Phys. 100 (2006) 094308.
18. S. L. Flegler, J. W. Heckman, K. L. Klomparens, *Scanning and Transmission Electron Microscopy: An Introduction* (Oxford University Press, NY, 1995).
19. S.V. Ketov, Yu.D. Yagodkin, A.L. Lebed, Yu.V. Chernopyatova, K. Khlopkov, *Structure and magnetic properties of nanocrystalline $SrFe_{12}O_{19}$ alloy produced by high-energy ball milling and annealing*, J. Magn. Magn. Mater. 300 (2006) e479.
20. S. Porthun, L. Abelmann, C. Ladder, *Magnetic force microscopy of thin film media for high density magnetic recording*, J. Magn. Magn. Mater. 182 (1998) 238.

STUDIA UNIVERSITATIS BABEŞ-BOLYAI, PHYSICA, LII, 1, 2007

CORRELATION EFFECTS AND THE ELECTRONIC STRUCTURE OF HALF-METALLIC FEROMAGNETS

L. CHIONCEL*

Most theoretical efforts for understanding half-metallic ferromagnets (HMF) are supported by first-principles calculations, based on density-functional theory (DFT). In fact the very discovery of HMF was due to such calculations [1]. DFT calculations are usually based on the Local Spin Density Approximation (LSDA) or the Generalized Gradient Approximation (GGA). These approximations have been proved very successful to interpret or even predict material properties in many cases, but they fail notably in the case of strongly-correlated electron systems. For such systems the so-called LSDA+U (or GGA+U) method is used to describe static correlations, whereas dynamical correlations can be approached within the LSDA+DMFT (Dynamical Mean-Field Theory). An important dynamical many-electron feature of half-metallic ferromagnets is the appearance of non-quasiparticle states [2,3] which can contribute essentially to the tunneling transport in heterostructures containing HMF [4,5].The origin of these states is connected with "spin-polaron" processes: the spin-down low-energy electron excitations, which are forbidden for HMF in the one-particle picture, turn out to be possible as superpositions of spin-up electron excitations and virtual magnons. The density of these non-quasiparticle states vanishes at the Fermi level but increases drastically at the energy scale of the order of a characteristic magnon frequency ω_m, giving an important contribution in the temperature dependence of the conductivity due to the interference with impurity scattering [3].

Our study focuses on the half-metallic ferromagnets in which the gap is situated in the spin-down/minority channel. (The results are valid equally to the cases when the half-metallic gap is situated in the spin-up channel). In this extend abstract the examples of semi-Heuslers NiMnSb [6] and FeMnSb [7] will be presented, while the lecture presents also results for full-Heusler Co_2MnSi and zinc-blende half-metals like CrAs [8] and VAs [9].

The temperature dependence of the HMF electronic structure and stability of half-metallicity against different spin-excitations is crucial for practical applications in spintronics. A simple attempt to incorporate finite-temperature effects [10], leading

* Graz University of Technology, Institute of Theoretical Physics - Computation Physics, A-8010 Graz, Austria

University of Oradea, Faculty of Science, RO-410087 Oradea, Romania

to static non-collinear spin-configurations, shows a mixture of spin up and spin down density of states that destroys the half-metallic behavior. In our work we use a different more natural approach to investigate the proper dynamical spin fluctuations effect on the electronic structure at temperatures $T<T_c$, within the half-metallic ferromagnetic state.

Nonquasiparticle states: an illustrative example: Before investigating, *ab initio*, real materials it is worthwhile to illustrate the correlation effects on the electronic structures of HMFs using a simple ``toy" model. The one-band Hubbard model of a saturated ferromagnet can provide us the simplest model of a half-metallic state. Difficulties in solving the Hubbard model are well known. Fortunately there is an exact numerical solution in the limit of infinite dimensionality or large connectivity called Dynamical Mean Field Theory (DMFT) [11]. Following this approach we will consider the Bethe lattice with coordination $z \rightarrow \infty$ and nearest neighbor hoping $t_{ij} = t/z^{1/2}$. In this case a semicircular density of states is obtained as function of the effective hopping t: $N(\varepsilon)=1/(2\pi t^2)\ (4t^2 - \varepsilon^2)^{1/2}$. In order to stabilize our "toy" model in the HMF state, we add an external magnetic spin splitting term Δ=0.5eV, which mimics the local Hund polarization originating from other orbitals in real materials. This HMF state corresponds to a mean-field (HF) solution with an LSDA-like DOS, denoted in Fig.1 as a dashed line.

Our model allows the study the magnon spectrum through the two-particle correlation function which is obtained using the QMC procedure. We calculate the local spin-flip susceptibility[6]:

$$\chi_{loc}^{+-}(\tau-\tau') = \langle S^{+}(\tau)\, S^{-}(\tau')\rangle$$
$$\chi_{loc}^{+-}(\tau-\tau') = \langle T_{\tau}\, c_{\uparrow}^{+}(\tau)\, c_{\downarrow}(\tau)\, c_{\downarrow}^{+}(\tau')\, c_{\uparrow}(\tau')\rangle_{Seff}$$

which gives us information about the integrated magnon spectrum [3,12]. The DMFT results are presented in Fig.1. In comparison with a simple Hartree-Fock solution one can see an additional well-pronounced feature appearing in the spin-down gap region, just above the Fermi level. This new many-body feature corresponds to the so-called non-quasiparticle states in HMF's and represents the spin-polaron process [2,3]

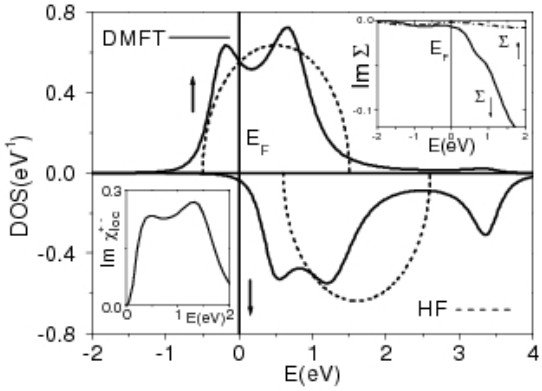

Fig. 1. Density of states for HMF in the Hartree-Fock (HF) approximation (dashed line) and in QMC solution of DMFT problem for semi-circular model (solid line) with the band-width W=2eV,Coulomb interaction U=2 eV, Δ=0.5 eV, chemical potential μ=-1.5 eV and temperature T=0.25 eV. Insets: imaginary part of the the spin-flip susceptibility (left) and imaginary part of self energy (right).

The left inset of Fig.1, represents the imaginary part of the local spin-flip susceptibility. One can see a well pronounced shoulder ~ 0.5eV, which is related to a characteristic *magnon* excitation [3]. In addition there is a broad maximum ~1eV corresponding to the Stoner excitation energy. The right inset of Fig.1, represents the imaginary part of self-energy. The spin up channel can be described by a Fermi-liquid type behavior, with a parabolic energy dependence Im $\Sigma_{\uparrow} \sim (E-E_F)^2$, whereas in the spin down channel, of $\Sigma_{\downarrow}$, the non-quasiparticle shoulder at 0.5 eV, is visible.

The existence of the non-quasiparticle states for this model has been proved by perturbation-theory arguments [2] (i.e. for a broad-band case) and in the opposite, infinite-U limit [3]. Physically, the appearance of these states can be considered as a kind of spin-polaron effect. According to the conservation laws, in the many-body theory the spin-down state with the quasimomentum **k** can form a superposition with the spin-up states with the qausimomentum **k-q** plus a *magnon* with the quasimomentum **q** running through the whole Brillouin zone. Taking into account the restrictions from the Pauli principle (an impossibility to scatter into occupied states) one can prove that this superposition can form only above the Fermi energy (here we consider the case where the spin-up electronic structure is metallic and the spin-down is semiconducting; oppositely, the nonquasiparticle states form only *below* the Fermi energy) [2,3]. If we neglect the *magnon* energy in comparison with the typical electron one, the density of non-quasiparticle states will vanish abruptly right at the Fermi energy; more accurate treatment shows that it vanishes continuously in the interval of the order of the *magnon* energy according to a law

which is dependent on the *magnon* dispersion [2]. As a consequence the non-quasiparticle states are almost currentless [2,3]. Recently, some evidence of the existence of almost currentless states near the Fermi energy in the half-metallic ferromagnet CrO_2 have been obtained by X-ray spectroscopy [13].

NiMnSb and FeMnSb: In the previous section we illustrated the effect of many-body interactions on the Hubbard model for a half-metallic ferromagnet. In this section we show that *the same* many-body effects are captured in the realistic LDA+DMFT electronic structure calculation for NiMnSb and FeMnSb. Fig.2 represents the results for density of states using LDA and LDA+DMFT

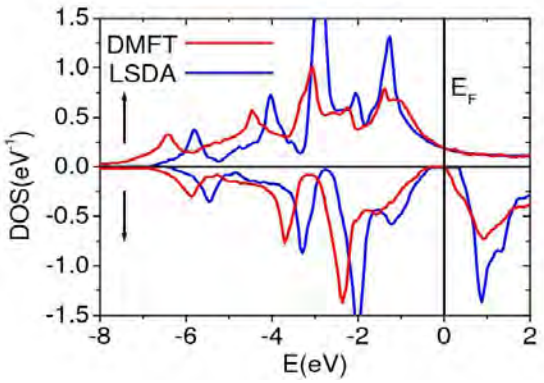

Fig. 2. Density of states for HMF NiMnSb in the LSDA scheme (blue line) and in LDA+DMFT scheme (red line) with effective Coulomb interaction U=3eV, exchange parameter J=0.9eV and temperature T=300 K. The NQP state is evidenced just above the Fermi level.

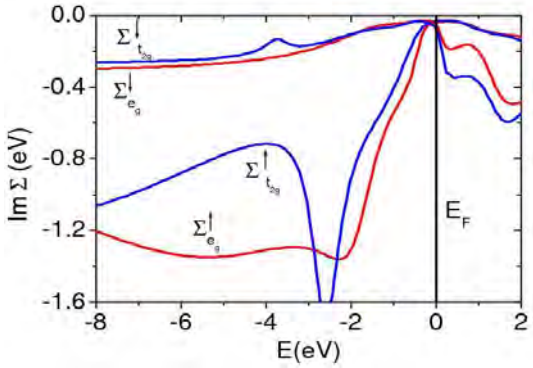

Fig. 3. The imaginary part of self-energies ImΣ_d^dw for t_{2g} (solid line) and e_g (dotted line), ImΣ_d^{\up} for t_{2g} (dashed line) and e_g (dashed dotted line) respectively.

It is important to mention that the magnetic moment per formula unit is not sensitive to the U values. For a temperature equal to T=300K the calculated magnetic moment, μ=3.96 μ_B, is close to the integer LDA-value μ=4.00μ_B, which suggests that the half-metallic state is stable with respect to the introduction of the correlation effects. In addition, the DMFT gap in the spin down channel, defined as the distance between the occupied part and starting point of non-quasiparticle states' "tail", is also not very sensitive to the U values. For different U the slope of the "tail" is slightly changed, but the total DOS is weakly U-dependent due to the T-matrix renormalization effects. Thus different values of U, do not effect too strongly on a general picture of the LDA+DMFT electron energy spectrum (except the smearing of the density of states features which is due to different temperatures in our calculations). In comparison with the LDA result, a strong spectral weight transfer is present for the whole occupied part of the valence band. The most interesting new effect is the appearance of the non-quasiparticle states in the energy gap above the Fermi energy. Their spectral weight for realistic values of the parameters are not too small which means that they should be well-pronounced in the corresponding experimental data.

In general, one should take into account *spin-orbit coupling effects* connecting the spin-up and -down channels through the scalar product between the angular momentum **l** and the spin **s** operators. The strength of this interaction is proportional to the spatial derivatives of the crystal potential V(**r**): V_{SO} ~ grad V **ls** with non zero off-diagonal elements $V^{\sigma,\sigma'}$,σ=↑,↓. Our results [7] suggest that depolarization in this class of Heusler compounds is dominated by NQP states, while *spin-orbit* contributions are much smaller. In addition, many-body effects are more pronounced in FeMnSb than in NiMnSb. (see Fig.5). This is tightly connected to the larger DOS in the majority spin channel in the former material. Therefore, doping of NiMnSb by Fe could be an interesting issue to investigate the interplay between alloying and many body effects. In this respect, we have carried out preliminary LDA+DMFT calculation on NiMnSb supercell containing 25% Fe impurities, i. e. for $(Ni_3Fe)Mn_4Sb_4$. Our results show a half-metallic character at the LDA level, with similar strong correlation-induced depolarization effects as in pure FeMnSb. Therefore, for this material, many body effects are of primary importance even in the presence of disorder.

The nature of non-quasiparticle states: From the point of view of the many-body theory, the general approach in DMFT is to neglect the momentum-dependence in the electron self-energy. In many cases, such as the Kondo effect, the Mott metal-insulator transition, etc. the energy dependence of the self-energy is obviously much more important than the momentum dependence and, therefore, the DMFT is adequate to consider these problems [11].

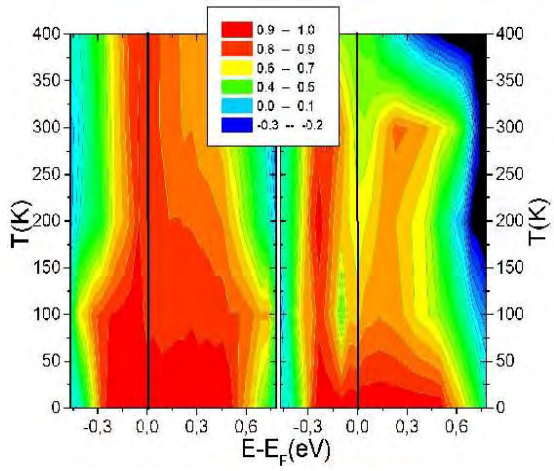

Fig. 4. Contour plots of polarization as function of energy and temperature for different values of local Coulomb interaction U. Left U=2eV, right U=4eV. The LSDA polarization is plotted as the T=0K temperature result. The asymmetry of NQP states is clearly visible for U=4eV.

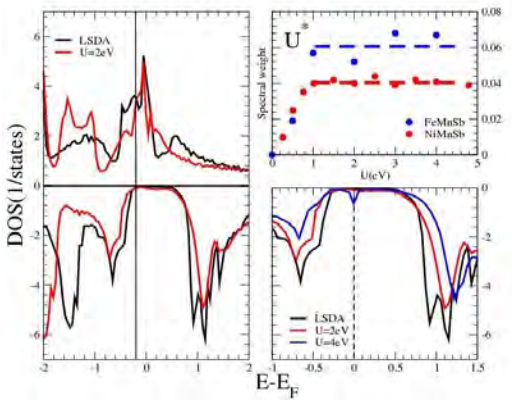

Fig. 5. Left: Density of states of half-metallic FeMnSb, LSDA (black line) and LSDA+DMFT (red line), for the effective Coulomb interaction U=2eV exchange parameter J=0.9eV and temperature T=300K. Lower right panel: zoom around E_F for different values of U. Upper right panel: Spectral weight of the NQP states calculated as function of U. The values obtained for NiMnSb are plotted for comparison.

As for itinerant electron ferromagnetism, the situation is not completely clear. One can expect that in magnets with well defined local magnetic moments such as half-metallic ferromagnets the local approximation for the self-energy (i.e., the DMFT) should be even more accurate. In particular, as we discussed above, it can be used for the calculations of spin-polaronic (non-quasiparticle) effects in these materials.

Several experiments could be performed in order to clarify the impact of these non-quasiparticle states on spintronics. Experiments such as Bremsstrahlung Isohromat Spectroscopy (BIS) or Spin Polarized Scanning Tunneling Microscopy (SP-STM), Andreev reflection spectroscopy using the tunneling junction superconductor - HFM will be discussed during the lecture.

REFERENCES

1. R. A. de Groot, F. M. Mueller, P. G. van Engen, and K. H. J. Buschow, Phys. Rev. Lett. 50, 2024 (1983).
2. D. M. Edwards and J. A. Hertz, J. Phys. F 3, 2191 (1973).
3. V. Yu. Irkhin and M. I. Katsnelson, J. Phys. C 18, 4173 (1985); J. Phys.: Condens. Matter 2 , 7151 (1990); M. I. Katsnelson and D. M. Edwards, J. Phys.: Condens. Matter 4, 3289 (1992).
4. V. Yu. Irkhin and M. I. Katsnelson, Eur. Phys. J. B 19, 401 (2001).
5. G. Tkachov, E. McCann, and V. I. Fal'ko, Phys. Rev. B 65, 024519 (2001)
6. L. Chioncel, M. I. Katsnelson, R. A. de Groot, and A. I. Lichtenstein, Phys. Rev. B 68, 144425 (2003)
7. L. Chioncel, E. Arrigoni, M.I. Katsnelson M, A.I. Lichtenstein Phys. Rev. Lett. 96, 137203 (2006)
8. L. Chioncel, M. I. Katsnelson, G.A. de Wijs, R.A. de Groot , A.I Lichtenstein, Phys. Rev B 71, 085111 (2005)
9. L. Chioncel, P. Mavropoulos, M. Lezaic, et. al. Phys. Rev. Lett. 96, 197203 (2006)
10. R. Skomski and P. A. Dowben, Europhys. Lett. 58, 544 (2002). P. A. Dowben and R. Skomski, J. Appl. Phys. 39, 7948 (2003).
11. A. Georges, G. Kotliar, W. Krauth, and M. Rozenberg, Rev. Mod. Phys., 68, 13 (1996).
12. T. Moriya, Spin Fluctuations in Itinerant Electron Magnetism (Springer, Berlin 1985).
13. E. Z. Kurmaev, A. Moewes, S. M. Butorin, et. al. , Phys. Rev. B 67, 155105 (2003).

STUDIA UNIVERSITATIS BABEŞ-BOLYAI, PHYSICA, LII, 1, 2007

GIANT HALL EFFECTS AND HALL EFFECT

MICHEL VIRET*

The **Hall effect** refers to the difference in electrical potential on the opposite sides of an electrical conductor through which an electric current is flowing, created by a magnetic field applied perpendicularly to the current. This potential is also referred to as the Hall voltage as it was first measured by Edwin Hall in 1879.

In ferromagnetic materials, it is found that the transverse resistivity (ρ_{xy}) contains a contribution from the magnetization (M) in addition to the usual Hall effect. This contribution is called the Anomalous Hall effect (AHE) and the conventional expression for the Hall resistivity is :

$$\rho_{xy} = R_0 . B_{perp} + R_s . \mu_0 M_{perp}$$

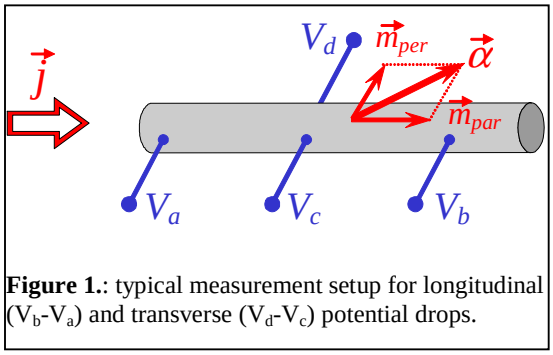

Figure 1.: typical measurement setup for longitudinal (V_b-V_a) and transverse (V_d-V_c) potential drops.

where $\boldsymbol{B}$ is the magnetic field, $\boldsymbol{R_0}$ is the usual Hall coefficient, and $\boldsymbol{R_s}$ is the anomalous Hall coefficient. The mechanism for the AHE is still controversial as theoretically, the key issues are whether the effect is intrinsic or extrinsic and how to treat the impurity and phonon scatterings. However, the basic ingredients necessary for this physical effect are somewhat consensual. These are the spin polarisation and spin-orbit coupling between the magnetic and orbital degrees of freedom. A typical measurement setup is shown in the figure where both transverse and longitudinal voltages can be measured.

Normal Hall Effect

The Hall effect in non-magnetic materials is due to the effect of the magnetic induction on the charge carriers. These charges experience a Lorentz force when a magnetic field is present that is not parallel to their motion. Without the magnetic field, the charges follow an approximately averaged straight path. However, when a perpendicular magnetic field is applied, their path is curved so that moving

* CEA Saclay, DSM/DRECAM/SPEC, 91191 Gif sur Yvette cedex, France

charges accumulate on one side of the material. This establishes an electric field that opposes the migration of further charge, so a steady electrical potential builds up for as long as the current is flowing. For a simple metal where there is only one type of charge carrier (electrons) the Hall voltage V_H is given by

$$V_H = \frac{-IB/d}{ne}$$

where I is the current across the plate length, B is the magnetic flux density, d is the thickness of the plate, e is the electron charge, and n is the bulk density of the carrier electrons.

One very important feature of the Hall effect is that it differentiates between positive charges moving in one direction and negative charges moving in the opposite. It actually offered the first real proof that electric currents in metals are carried by moving electrons and not by protons.

- Hall effect in semiconductors:

The Hall effect also showed that in some substances, especially semiconductors, it is more appropriate to think of the current as positive holes moving rather than negative electrons. Also, because in semiconductors the densities of states are much lower than in metals, Hall voltages are much larger. This property is important since it is currently used in field sensors.

- Quantum Hall effect:

At high magnetic field, one can envision that electron trajectories can be curved in smaller and smaller radii, eventually leading to charge localisation. This can indeed happen in pure samples and high field. The most impressive manifestation of this property is found in two-dimensional electron gases where the electronic density of states becomes a set of discrete Landau levels due to the confinement produced by the field. It follows that the Hall conductance is quantised in e^2I/h units.

The Anomalous Hall Effect

In 1880 Edwin Hall discovered that a transverse voltage is present in saturated ferromagnets even in the absence of an applied field. This Hall voltage is called spontaneous or anomalous (in practice a small H serves to align the magnetic domains). The origin of the anomalous Hall effect (AHE) has been vigorously debated for many decades and it is fair to say that its understanding is still a subject of controversy. However, one can say that the anomalous Hall effect occurs in ferromagnets because broken time reversal invariance in spin-space is transferred to orbital properties by spin-orbit coupling, and is related to the small orbital contribution to the magnetization in ferromagnetic metals.

Several mechanisms have been proposed to explain this physical phenomenon. Two theories attribute the AHE to the impurity scattering modified by the spin-orbit interaction, namely the skew scattering and the side-jump mechanism. These extrinsic effects are rather complicated and depend on the details of the impurities as well as on the band structure of the materials. A third mechanism has been recently revisited and seems to be favoured by more recent experimental results. This is the Karplus and Luttinger theory, which proposes an intrinsic mechanism of AHE. The model is based on the existence of an extra term in the group velocity of electrons called the "Berry curvature". One may regard it as an effective magnetic field that lives in reciprocal space to produce a Lorentz force, and hence a Hall voltage. All these theories for the AHE derive the right equation with a voltage proportional to M, as they are based on the perturbative expansion of the spin-orbit coupling.

Therefore any material with both spin polarised carriers and spin-orbit coupling will produce a non-zero transverse voltage proportional to the magnetisation. In homogeneous magnetic materials and giant magneto-resistance composites, this contribution can be much larger than the normal Hall effect. Another manifestation of the phenomenon is to be found in the so called ‘spin Hall effect’ where spin-orbit coupling generates a spin dependent transverse scattering but the absence of a net carriers’ spin polarisation prevents the building of charges. This results in a pure spin accumulation. These Hall effects will be presented in detail during the lecture with a particular emphasis for applications in spin electronics.

STUDIA UNIVERSITATIS BABEŞ-BOLYAI, PHYSICA, LII, 1, 2007

"BIOMEDICAL APPLICATIONS OF MAGNETIC NANOPARTICLES I: DRUG DELIVERY"

M.R. IBARRA[12], R. FERNÁNDEZ-PACHECO[1], C. MARQUINA[2], J.G VALDIVIA[1]

The wide interdisciplinary world of Nanoscience has experienced a strong development during the last years. One exciting topic is the possibility of using nanoscale magnetic materials for biomedical applications. Many interesting problems regarding magnetic properties exist to be investigated from the fundamental point of view, and expectations are opened for their application as magnetic carriers and bioferrofluids.

One of the important points in the use of magnetic nanoparticles for biomedical applications is the encapsulation of the magnetic material, in order to make it biocompatible, and to have the possibility of producing a bio-ferrofluid. Coating the nanoparticles with a suitable material offers the possibility of attaching them to antibodies, proteins, medical drugs etc. Therefore studies on surface adsorption, the possibility of functionalising and/or conjugating the particle coating with bioactive components are also a crucial issue. The election of the magnetic material as well as a detailed knowledge of its magnetic properties play an important role in the use of the nanoparticles in Biomedicine, as well as in the effectiveness of the desired application. In order to obtain the biocompatible ferrofluid, we have prepared carbon coated iron nanoparticles. In the following sections the adequacy of both carbon and iron as staring materials for the synthesis of biocompatible magnetic carriers is discussed.

The magnetic nanoparticles offer the possibility of being directed towards a specific target in the human body and remaining eventually localised, by means of an applied magnetic field. Obviously, when magnetic nanoparticles are going to be used for in vivo applications, very low values of applied magnetic field are desirable. Therefore the suitable materials are those with high magnetisation at the operation temperature, that is to say, at room temperature. As stated at the beginning of this section, standard starting materials for the production of magnetic particles are iron, cobalt and nickel. Nevertheless, the control of the particle size and shape, and the matrix or medium in which the particle is embedded, is also of crucial importance. In vivo applications (like drug delivery, magnetic resonance

[1] Instituto de Nanociencia de Aragón, Edificio Interfacultades II, Zaragoza (Spain)
[2] Instituto de Ciencia de Materiales de Aragón (CSIC/Universidad de Zaragoza), Facultad de Ciencias, Zaragoza (Spain)

imaging, hyperthermia, additionally require particles being biocompatible, stable and biodegradable. This is achieved by coating and embedding the particles in a suitable material. Polysaccharides (like dextran), or polymers (as for example polyvinyl alcohol) are used as typical coatings, whereas water-based ferrofluids are the most commonly used injection vehicle. Coating the particles allows also the possibility of modifying the particle surface by attaching bioactive components, as antibodies, proteins etc, by means of chemical bonding or by means of adsorption, which broadens their possibilities for applications. Concerning the particle size, and particularly in the case of in vivo applications, the magnetic particles should not retain any remanent magnetisation once the magnetising field has been removed. This would avoid aggregation due to dipolar interactions between their respective magnetisations, favouring the biological absorption and eventual excretion of the particles by the body.

An optimum magnetic response has been achieved using iron nanoparticles. With respect to the coating, carbon has been used as biocompatible material. One of the advantages of using carbon is its high capacity of adsorption. Iron coated nanoparticles are therefore appropriate to be used as magnetic carriers of medical drugs, magnetic resonance imaging contrasts, biological labels etc, adsorbed into the carbon surface.

The production of carbon coated magnetic nanoparticles is accomplished by two methods: by the arc discharge method designed by Krätschmer-Huffman in 1990 which uses a plasma furnace, with two graphite electrodes. One of them is a stationary anode, which consists of a drilled carbon cylinder where, in our particular case, several micrograms of 10 micron iron powders are introduced. The cathode is a moveable graphite electrode. An arc is created between the graphite electrodes in a helium atmosphere. The moveable electrode is sublimed and builds up a carbonaceous deposit or *collaret* around it, at the same time that soot is deposited on the inner surface of the chamber walls. The morphologic and structural characterizations have been performed by Transmission Electron Microscopy (TEM), Dynamic Light Scattering, and electron diffraction. The magnetic nanoparticles are encapsulated either in carbon nanotubes (this are mainly found in the cathode), in concentric graphitic shells (“onions”) or in amorphous carbon. In the case of samples obtained by high energy milling TEM shows that the final powder is composed by a mixture of carbon coated nanoparticles together with the free carbon and non encapsulated magnetic metallic particles.

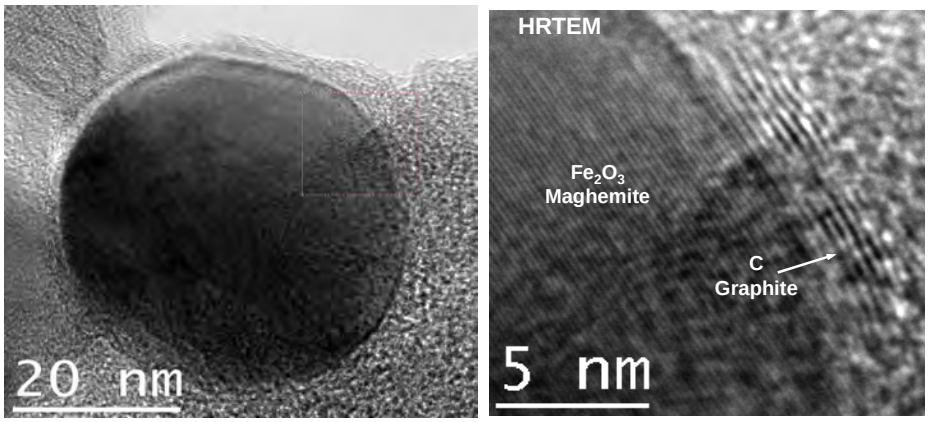

HRTEM images of carbon coated magnetic nanoparticles produced by arc discharge. As corresponds to a lighter element, C appears with a lighter contrast compared to Fe.

Electron Filter (EF)-TEM has been also performed in order to get a better insight into the chemical nature of the obtained materials. EFTEM images have been taken selecting the Electron Energy Loss Spectroscopy (EELS) peaks separately for iron and carbon (iron at 708 eV, L_3 peak, and carbon at 284, K peak). Once both images were obtained, an elementary map can be drawn, showing a coloured distribution of each of the elements. The EFTEM confirms the presence of iron content in the core of the nanoparticles, which is completely surrounded by a carbon coating. The crystallographic structure of the samples has been analysed by electron diffraction. According to the patterns, the core of the magnetic nanoparticles contains iron oxide, crystallised in the cubic phase γ-Fe_2O_3, or maghemite (Fernández-Pacheco et al., to be published). The morphological and structural characterization shows that the samples prepared by arc discharge as well as the samples prepared by mechanical milling contain also non-coated or partially-coated nanoparticles, which are not biocompatible and therefore not suitable to be used as magnetic carriers. Moreover, all those carbon nanostructures that not contain magnetic nanoparticles have to be eliminated, in order to enrich the magnetic concentration of a future bio-ferrofluid. With this purpose a combined magnetic and chemical purification method as been developed. For magnetic purification, stable suspensions of the particles are prepared in a surfactant solution (2.5 g of SDS in 500 ml of distilled water). Magnetic separation (by means of a 3 KOe permanent magnet), yields only magnetic nanoparticles. Afterwards the purified magnetic material is washed with HCl 3M at 80ºC. All the non-completely coated magnetic material is dissolved and the remaining coating carbon forms carboxylic groups,

which, due to their hydrophobic nature, contribute to the stability of a future ferrofluid suspension. The sample is finally heated at 350ºC in order to evaporate remaining free amorphous carbon structures (Fernández-Pacheco et al., to be published).

Magnetisation measurements on purified samples were performed in a Superconducting Quantum Interference Device (SQUID). The magnetisation isotherms at room temperature show no coercivity and no remanent magnetisation. This is characteristic of superparamagnetic behaviour, in good agreement with the nanometric size of the magnetic particles derived from TEM images. Therefore we can conclude that the synthesised magnetic nanoparticles fulfil all the requirements to be used as magnetic carriers for future in vivo applications. The experimental results can be compared to those predicted by the theory of Langevin for superparamagnetism, in which the magnetisation of a nanoparticle, *m*, is a function of the temperature, *T*, and of the applied magnetic field, *H*, and follows the Langevin's law

$$m(T,H) = m_s\left(\coth\left(\frac{\mu H}{k_B T}\right) - k_B T \Big/ \mu H\right)$$

were m_s is the saturation magnetisation of the particle, μ is the magnetic moment of the particle and k_B is the Boltzman constant. Introducing the value of m_s for iron (1740 emu/cm^3), and fitting the experimental data to the Langevin's law the value of μ can be derived. As the magnetic moment is proportional to the particle volume V ($\mu = m_s V$) the values of the particle diameter can be derived, assuming spherical shape for the magnetic nanoparticles.

The magnetic characterisation has been completed by Mössbauer spectroscopy. The Mössbauer spectra allowed us to identify the presence different iron phases in the samples, even non-magnetic phases, and also to calculate the percentages of each of them. In the case of arc discharge produced samples taken from the *collaret* and the soot the Mössbauer spectra revealed the presence of non-magnetic γ-Fe in addition to α-Fe and Fe_3C.

Because of its biocompatibility, small size, superparamagnetic behaviour and big surface area, possible applications of these nanoparticles in biomedicine are nearly unlimited. At present we have focused in two main fields: drug targeting and conjugation to proteins. In the first case, the magnetic nanoparticles are suspended in water forming an stable bioferrofluid. Subsequently the drug is chemically bound to the carbon coating. This ferrofluid is directed to the target area in the human body by means of an applied magnetic field. The magnetic carriers are concentrated there until the drug is released in a desorption process, at the end of

which the magnetic field is switched off. This enables a very specific treatment and eliminates the limitations on the applied dose because of possible damage to healthy tissues. On the other hand, our synthesised magnetic nanoparticles have been conjugated to a number of antibodies and have been widely used for the development of lateral flow tests. These tests are available for pregnancy, ovulation, infectious disease, drug monitoring or bacterial contamination. The introduction of magnetic particles allows the immobilization, controlled delivery and release of molecules adsorbed to the surface of these particles by means of an external magnetic field, as well as the quantification of these tests by magnetization measurements. Carbon coated metal nanoparticles represent an alternative to polymeric coatings, and the first results obtained have been really satisfactory.

REFERENCES

1. "Magnetic Nanoparticles for drug delivery" M. Arruebo, R. Fernandez-Pacheco, M. R. Ibarra and J. Santamaria Nanotoday 2 (2007) 22 (review paper)
2. "Magnetic nanoparticles for local drug delivery using magnetic implants" R. Fernandez Pacheco et al. J. Magn. Magn. Mat. 311 (2007) 318.
3. Contact author ibarra@unizar.es

STUDIA UNIVERSITATIS BABEŞ-BOLYAI, PHYSICA, LII, 1, 2007

"BIOMEDICAL APPLICATIONS OF MAGNETIC NANOPARTICLES II:ELECTROMAGNETIC RADIATION"

G. F. GOYA[*], V. GRAZÚ[*], M. R. IBARRA[*]

Magnetic nanoparticles are used in "in-vivo" diagnosis and therapy on the bases of their interaction with electromagnetic radiation. Here we will concentrate in the tomography using magnetic resonance imaging (MRI). In this case the magnetic moments of the magnetic nanoparticles used as contrast agent, produces a local change of the proton resonance which enhance the MRI contrast. Other aspect which we will cover is the magnetic fluid hyperthermia (MFH), which uses magnetic nanoparticles as heat generators to induce localized cell death. The physical basis of these techniques relies on the interaction with external electromagnetic fields.

The first therapeutic applications of magnetic devices to humans can be chased back to the 16^{th} century, when Austrian physician Franz Anton Mesmer (1734-1815) developed his theories about magnetic fluids. He sustained the influence of invisible 'universal fluids' on the human body (after the Newtonian ideas of 'aether' associated to gravitational forces and tidal cycles), and proposed his theory of 'animal magnetism' gaining notoriety across Europe. Since then Mesmerism (a therapeutics based mainly on hypnotism) has triggered a sustained flood of both research and 'supernatural' quackery.

[*] Aragon Institute of Nanoscience (INA), Universidad de Zaragoza,Pedro Cerbuna 12, 50009 Zaragoza, Spain.

Pushed by advances in the synthesis of biocompatible magnetic nanoparticles (MNPs) in a reproducible way, the concept of targeting magnetic nanospheres inside microscopic living organisms regained interest and finally became a reality. The size of MNPs is comparable to the DNA or subcellular structures, then, they can be used for cell separation strategies using magnets as external driving forces. Similarly, recent advancements on binding chemistry of biological units onto MNPs surface and the engineering of particle's surface/shape have opened new exciting possibilities for drug delivery with high selective vectors. Nonetheless, *in vivo* applications entangle subtle problems related to the response of a living organism to alien objects (i.e., NPs-drug assemblies). For example, even if a perfectly selective drug delivery system could be designed (e.g., by using some monoclonal antibody-loaded particles), any real experiment has to overcome the problem of immunological reactions triggered by the invading NPs within the host, mainly from the reticuloendothelial system (RES).

At present, most applications of MNPs are based on the following physical principles:

a) The application of controlled magnetic field gradients (i.e., a magnetic force) around the desired target location for remotely positioning MNPs in organs or tissues (targeting, magnetic implants, magnetic separation applied to the sequencing of DNA, etc).

b) The utilization of the magnetic moment of the MNPs as a local perturbation of the proton nuclear resonance (contrast media for Magnetic Resonance Imaging, MRI).

c) The magnetic losses of nanometric particles in colloids for heating purposes (magnetic hyperthermia)

Electromagnetic radiation

Electromagnetic (EM) radiation is a fundamental tool in cancer therapy, extensively used for both diagnostics and therapy. Physical interactions between EM waves and living matter can be very different depending on the portion of the electromagnetic spectrum considered. A variety of clinical tools have been established in physical medicine based on direct emission and detection of EM waves such as x-ray radiography, computer tomography scanning (CT scan) and gamma-ray radiotherapy from radioactive isotopes. Many other techniques rely on indirect uses of EM radiation such as positron-emission tomography (PET), magnetic resonance imaging (MRI), and microwave hyperthermia (MWH).

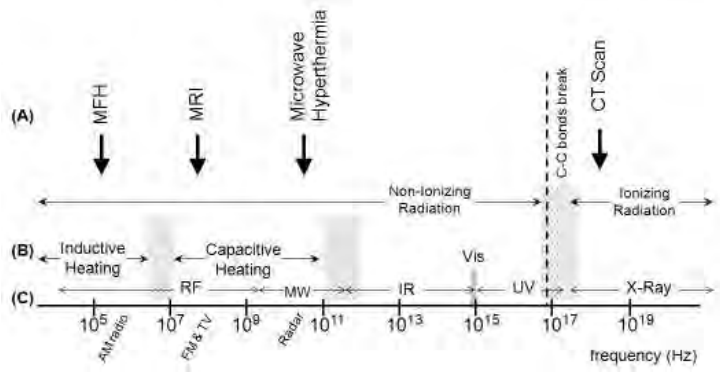

Figure 1. A. Frequency ranges for some of the most used diagnostic/therapy equipments (MFH = Magnetic Fluid Hyperthermia, MRI = Magnetic Resonance Imaging). B. The respective main physical mechanisms at each frequency range. Also shown in (C) is the common nomenclature for the electromagnetic waves at each region: RF = radiofrequency; MW = microwaves; IR = infrared; Vis = visible; UV = ultraviolet and X-Ray.

Figure 1 schematizes the different ranges of the EM spectrum used by different techniques, and also puts comparatively some physical and biological phenomena occurring within each region. The importance of this "EM landscape" is connected to absorption of energy by biological units, since the shorter the wavelength, the higher the energy content. Organic materials composed of long-chained molecules with C-C (or C=C) backbones and other carbon bonds like C-H, C-N, can absorb EM radiation at some specific frequencies that are, consequently, biologically dangerous. As an example, covalent bonds can be broken at approximately 10^{12} Hz ($\lambda \approx 300$ nm, in the UV range). Larger units have more complex (secondary, tertiary) structures, and may be bound to other units by entanglement alone, secondary forces or chemical bonds. Due to this variety of binding forces, living matter displays several 'frequency windows' where interaction with EM radiation can destroy biological units and/or metabolic functions. The frequency ranges employed by the techniques of Figure 1 are usually grouped in two coarse classes: those based on non-ionizing radiation (basically radiofrequency and microwaves), and those using ionizing radiation (high-energy X-rays and gamma-rays). The limit between these areas is defined by the energy threshold to break C-C, C-H and C-N covalent bonds, which would imply the breaking of fundamental organic molecules as DNA, RNA, proteins, etc…

Hyperthermia

For a piece of metal subjected to low- and medium-frequency alternating fields ($> 10^2 - 10^3$ Hz, for example the case of nuclei of electrical motors) the main mechanisms of power losses are magnetic hysteresis and parasitic currents (eddy currents). On the other hand, in ceramic materials the dissipation of power is mainly originated in processes of nucleation, growth and extinction of magnetic

domains. For single-domain particles in physiological conditions the situation differs radically, because a) the magnetic saturation is reached by coherent rotation of the total magnetic moment of each particle; and b) the hysteresis cycles are theoretically reversible and thus they do not entail magnetic losses. In addition to coherent rotation to be considered for single-domain particles, physiological conditions allow mechanical rotation of the particles as a response to the external magnetic field, at least for low frequencies. It follows that for colloidal dispersions the analysis of the heat transference processes must include the effects of both the Brownian motion and fluid. For biomedical applications based on the increase of temperature as magnetic fluid hyperthermia (MFH) therapy, it is clear that the mechanisms of power losses in colloids must be identified before new, more efficient therapeutic materials can be designed to *maximize* the generation of heat.

The heating capacity of a magnetic material or electromagnetic device is quantified through the specific absorption power rate (SAR), defined as the amount of energy converted into heat per time and mass. In terms of the usual experiments and parameters for magnetic colloids, the loss power per gram of Fe_3O_4 is obtained from the heating curves within the initial ΔT temperature rising interval through the definition

$$SAR = C_S \frac{\Delta T}{\Delta t} = \frac{Q}{\rho_t} \ , \qquad \textbf{(I)}$$

where C_S is the sample heat capacity, defined as a mass-weighted mean value for a given concentration of magnetic material, calculated as

$$C_S = \frac{m_{Fe}\, c_{Fe} + m_l\, c_l}{m_{Fe} + m_l} \qquad \textbf{(II)}$$

with c_{Fe}, m_{Fe} and c_l, m_l being the specific heat capacities and masses of magnetic material and liquid carrier, respectively. The last member shows the relationship between the functional definition of SAR and eq. IX.

Within oncology therapeutics, hyperthermia is a general term for the rise of temperature above the physiologic level (in the 40°C -45°C range) within a targeted tumor without damaging the surrounding healthy tissue. The rationale of this therapy is based on solid evidence from preclinical data that the antitumor cytotoxicity of radiation can be enhanced by previous temperature increase of cells or tumor tissues. It is accepted that at the cellular level hyperthermia provokes morphological and physiological changes, such as the loss of integrins from the cell surface, which is thought to be a perturbing effect on metabolic pathways preceding cell death. The actual mechanisms active during hyperthermia treatments seem to be similar to those of radiation regarding cell cycle sensitivity and hypoxia. The most extended method for reaching temperatures above the systemic values (i.e., 37·5°C) is based on the application of microwaves, although therapies involving laser or ionizing radiation have also been successfully applied to heat up malignant tissues. All these strategies are capable of easily rise the intracellular temperature to the degree needed for thermo-ablation, but also they all have undesired collateral effects such as ionization of genetic material (radiation) or lack of selectiveness (microwaves) that affect the surrounding healthy tissues.

Magnetic hyperthermia can be defined as the rise of temperature that can be accomplished remotely by means of external alternating magnetic field acting on MNPs at the targeted location.

It is important to note that the EM radiation used by MFH belongs to a frequency region where the heating effects on living tissues are negligible. Therefore,

differently from other hyperthermia methods, MFH needs a heating agent (i.e., the magnetic nanoparticles) placed at the targeted cells in order to produce the temperature increase. This difference if the main reason of the potential advantages of MFH over alternative strategies, since MNPs can be in principle attached exclusively to (or even introduced into) tumoral cells to heat them with minimum influence on the surrounding healthy tissues. Therefore the success of this approach depends critically of the ability to attach a given particle on those cells that are to be killed (i.e., the 'targeting problem').

The underlying physical mechanisms of MFH are related to the energy dissipation when a ferromagnetic material is placed on an external alternating magnetic field. In physiological conditions there are different effects to be considered for power losses: a) magnetic losses through domain wall displacements (in multi-domain particles), Néel relaxation (in single domain particles); and b) energy loss from mechanical rotation of the particles, acting against viscous forces of the liquid medium (Brownian losses).

Magnetic Resonance Imaging (MRI)

Magnetic Resonance Imaging (MRI) is the most successful among the imaging techniques currently available. It is a non-invasive, non-destructive modality that can reconstruct both 2D and 3D images of an internal living structure, without limitation in volume or depth of the analyzed target. Since the 1980s, the implementation of dedicated hardware for MRI scanners has reduced the image acquisition time from the many-hour down to the second-scale, widening the applications to include fast dynamic processes. Additionally, signal processing and the development of high-sensitivity RF detectors have shifted the spatial resolution limit from the cm scale to about 10 μm, enabling *in vivo* imaging at microscopic

resolution. The above advantages have made MRI to become a most valuable technique for cancer diagnosis and therapy.

Any resonant technique is based on the existence of physical entities (e.g., electrons, nuclei, or molecules) that can be promoted from their ground state (taken as the zero-energy, E_0) to higher-energy excited states with E_1, E_2,…E_n. In the case of MRI, the resonant physical entities are the hydrogen nuclei (protons) that exist abundantly in living tissues. Protons placed in a homogeneous magnetic field B_0 can absorb electromagnetic (EM) waves carrying energies E_ν satisfying $E_\nu = \Delta E$, where ΔE is the energy difference $\Delta E = E_1 - E_0$ between two nuclear levels. Note that MRI involves a *magnetic* coupling between the magnetic-component of the EM waves and the *magnetic* moment of the resonant hydrogen nucleus (nuclear spin). Therefore the MRI is a *nuclear* resonance technique that gives information based on (but not restricted to) the *magnetic* properties of the biological samples. The signal from relaxation of the excited protons is captured through currents induced over a specific arrangement of pick-up coils, and finally the whole relaxation process is reconstructed computationally to obtain temporal or spatial (2D and 3D) images of the desired organ/tissues. The pick-up coils are needed to transmit and/or receive the MR signal, and for optimum signal-to-noise ratio the coils should cover only the working volume to be observed. Many types of pick-up coils have been designed for minimum noise (e.g., caging coils for head and knee local studies), balancing observation volumes and sensitivity.

The energy $E_\nu = h\nu$ (where ν id the frequency and h is the Planck constant) of the EM waves used for resonant excitation will depend on the applied static field, B_0, through the relation

$$\upsilon = \frac{\gamma}{2\pi} B_0 \qquad \textbf{(III)}$$

where the γ = 267.66 MHz/Tesla is Larmor frequency of the proton. Current commercial MRI platforms employ dc fields B_0 between 1 and 3 T, so that required RF frequencies are in the 50-100 MHz range. But companies have started to develop 7, 8 and 9 Tesla systems that imply the use of frequencies within the ~ 0.3 GHz range. At these high RF frequencies dielectric coupling of the EMF with biological material cannot be neglected (see Figure 1), and indeed heating effects have been observed in phantoms using 8 Tesla MRI platforms. The strategy used to visualize and track target cells by MRI is to tag them with a contrast agent, a ferrofluid containing biocompatible MNPs.

SPION-based contrast agents

The purpose of injecting CA's is to *change* the relaxation rates (called T1 and T2) of the surrounding hydrogen atoms of the tagged cells, to the extent that a measurable change in signal intensity (contrast) is observed between particle-charged and normal tissues. The resulting differences in signals from various body tissues enable MRI to differentiate organs and to contrast benign and malignant (particle-loaded) tissues.

Gadolinium(III) was the first magnetic material clinically used as a contrast agent and still remains the foremost material in terms of total volume employed around the world. This fact is probably related to the slow and costly process of preclinical validation of a new material intended for human uses, which delays the marketing of new products. However, different alternatives are being increasingly reported as good candidates for CAs, such as additional lanthanide ions and iron oxide nanoparticles. Commercial contrast agents based on SPIONs are composed of a iron oxide core of

5 to 10 nm diameter (usually magnetite Fe_3O_4 or maghemite γ-Fe_2O_3), coated with a polysaccharide such as dextran for stabilization purposes, which results in a hydrodynamic size of ~150 nm diameter.

From the physical side, the performance of CAs regarding how it influences the relaxation of neighbor protons is proportional to the square of the saturation magnetic moment (M_S) of the particles, thus the design of new CAs requires optimized magnetic materials with large M_S values. All contrast agents based on MNPs make use of the large magnetic moment of iron-oxide subdomain particles, which can be 10^3 times larger than a single paramagnetic atom. The proximity of the magnetic particles to the desired target tissue is also a crucial parameter, since the magnitude of the interaction between a magnetic particle and neighboring protons is proportional to the sixth power of the inverse of the distance raised to (r^{-6}),

The efficiency of any MRI contrast agents as an early-diagnosis tool is intimately related to its capability of giving the strongest signal capable to be detected with the smallest amount of magnetic material. Current CAs are composed of passive MNPs and thus there are far from the above specification. In general terms, the ideal efficiency would imply

- Selective binding to target cells to provide a local, specific enhancement;
- Improved relaxational properties to decrease the detection threshold to low than 1mmol Fe/kg.
- Prominent signal–to–noise enhancement to allow high resolution levels;
- Long circulating half-life (hours) to expand the imaging time window;
- Acceptable toxicity profile to be biologically safe;
- Ease of production and clinical use to be economically and commercially sustainable;

Note of the authors: This lecture is a summary of the review paper "Magnetic Nanoparticles for Cancer Therapy" Current Nanoscience, in press

Corresponding author: goya@unizar.es

STUDIA UNIVERSITATIS BABEŞ-BOLYAI, PHYSICA, LII, 1, 2007

INTRODUCTION TO MAGNETIC RECORDING + RECORDING MATERIALS

LAURENT RANNO[*]

I will give two lectures about magnetic recording. In the first one, I will present the field of data storage and some of the relevant parameters which have to be discussed when proposing magnetic storage as the relevant technology. In the second lecture I will discuss in more detail the magnetic materials which have been developed (mainly based on transition metals) and some new materials which are being considered for magnetic recording (for example ferromagnetic semiconductors). The physical properties (magnetisation, magnetic anisotropy, spin transport properties …) or physical effects (magnetisation reversal mechanism, magnetic coupling, magnetic biasing, magnetoresistances …) which are relevant to magnetic storage or magnetic sensing will be discussed.

Many families of magnetic materials are relevant to magnetic recording, from hard magnetic materials for storage to soft materials for sensing. From metallic ferromagnets to insulating antiferromagnets, the range of useful materials is quite extended.

Data storage

Information Storage

In our technological age, a huge amount of information needs to be stored in a digital manner. The trend is exponential and shows no signs of calming down. This is the driving force in the field of data storage and makes it a fast evolving industry. Regarding microelectronics, Moore's law is the well known self-replicating trend which predicts that the number of transistors per surface area will double every 18 months. In the last decade the growth of hard disk drive (HDD) bit density has been faster than that of microelectronics and has reached 100% bit density increase per year. A density of 100 Gigabit/in^2, originally thought to be a dream value, has been reached in labs in 2002 and is already in commercial HDD. The new target is 1 Terabit/in^2.

Data storage is a large industry and many technologies compete. The life cycle of technologies is only a few years long and innovation is constant. Before discussing the field of high density magnetic recording, let us detail some of the criteria that govern storage technologies.

[*] Institut Néel, Nanoscience Dept, CNRS-UJF, Grenoble, France

Data

The quantity of bits to store is a first parameter. A microprocessor will deal with 32 or 64 bits at a time and a few megabits (Mb) will be stored in cache memory. One hour of music (i.e a CD-ROM) will be equivalent to a few 100 Mbytes (MB) while one hour of video (i.e. a DVD-ROM) will need a few Gbytes of storage. The typical capacity of a personal computer hard disk drive has now reached 100 GB. A small archiving system will deal with terabytes (10^{12} bytes) and a large archiving system will store petabytes (10^{15} bytes). The total capacity of hard disk drives produced per year is already a few exabytes (10^{18} bytes).

Data access

Data should not only be stored but they must also be accessed. Sequential access (e.g. tapes) and random access (e.g. Random Access Memory RAM) are two possibilities, the choices depending on the use. Sequential access is suitable for archiving or to watch a video, whereas accessing files on a hard disk needs random access, as any bit can be required at any moment. The access time and the access rate also matter. The timescale can span orders of magnitude from minutes to access a tape to nanoseconds to read an individual RAM cell and the required data flow can reach Gigabytes per second.

Volatility

Data storage should show a certain lack of volatility. However, non-volatility will be designed taking into consideration the relevant timescale. This can span orders of magnitude, from years in the archiving business down to microseconds in computing.

Competing Physical Effects

Bistable state

A digital memory requires two well defined and stable states to store a bit. Many physical effects offer such configurations. Bits can be stored using two physical levels by mechanically engraving the storage medium : bumps on a CD-ROM or DVD-ROM, tracks on old-age LPs (analogue storage). Optical properties of the media can be modified to create reflecting/non-reflecting bits (recordable (CD-R) and erasable (CD-RW)) or bits with opposite magneto-optical properties (magneto-optical storage). The data can also be materialized by the presence or absence of an electrical charge as in semiconductor memories (SRAM, DRAM, Flash), the presence or absence of electrical polarisation like Ferroelectric RAM (FeRAM), the crystallized or amorphous nature of an alloy as in phase change media (PCRAM memory) and of course the direction of a magnetic moment (magnetic tapes, hard disk media, magnetic RAM).

Reading technique

Depending on the way data have been stored and on data density (bit size), the appropriate reading technique is required. Mechanical bits (LPs) were read using a mechanical contact, present CD-ROMs are read using a focused infrared laser reflected from bumps in polycarbonate (bump height is a quarter of the wavelength in polycarbonate) so that the laser beam undergoes destructive interference when reflected from the edge of a bump. Optical bits are also read measuring a reflected laser beam. Electrically stored bits can be read because they control (open or closed) the channel of a transistor, by monitoring the discharge of a capacitor or by sensing the electrical resistance of the bit (phase change RAM). Magnetic bits are read by sensing the magnetic stray field above them or more directly by monitoring changes of the polarization of a laser (magneto-optical effects) or by measuring their resistance (magnetoresistive effect). Unexpected physical effects can be used in innovative systems such as the thermal dissipation change used in IBM's Millipede program.

Characteristics of Magnetic Recording

A ferromagnetic material can possess a well defined axis (the easy-axis) along which its magnetic moments will preferably align. The two possible directions will define two stable states. When the easy-axis is well defined (large remanence of the magnetisation along the easy-axis in the absence of applied field) and if the field necessary to reverse the magnetic moment (the coercive field) is large enough, the material will be called a permanent magnet and can be used to store information. The minimum size of a stable magnetic particle is smaller than 10 nm (depending on the material), which translates directly into high density storage and the intrinsic switching time of a particle magnetisation is in the nanosecond range, which leads to short data read and write times. High density and fast write-time are two of the main advantages of magnetic recording.

Here are some points which will be discussed in the lectures :

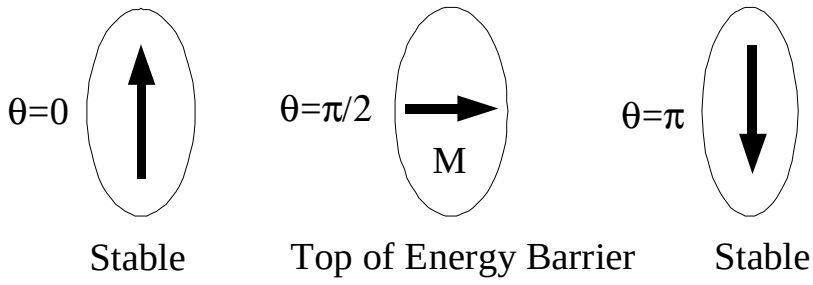

Stable states of the remanence of a magnetic particle. Thermally induced reversal of the particle magnetisation is possible when its volume becomes small enough. This phenomenon is called superparamagnetism and is one of physical limits that is being "pushed back" to improve recording density. Coupling to artifical antiferromagnetic layers has recently allowed the use of particles smaller than the superparamagnetic limit!

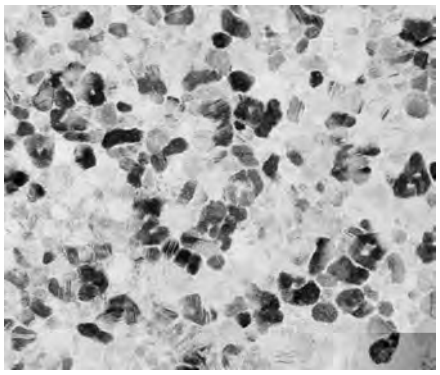

45 Gbit/in^2 demo media (Seagate)

•8.5 nm grains

$\sigma_{area} \cong 0.5$

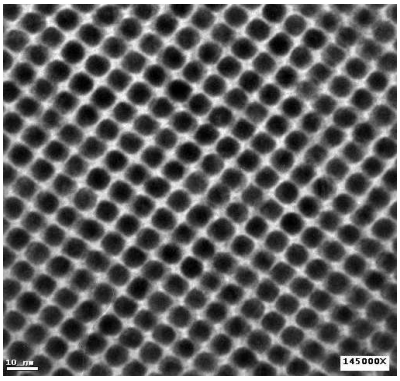

Nanoparticle arrays

•6 nm FePt particles

$\forall\ \sigma_{area} \cong 0.1$

To improve recording density, small particles with very narrow size distribution have to be synthesised. New materials such as high anisotropy FePt $L1_0$ are candidates. The following aim is to spatially organise the particle positions (lithography, self organisation…) and eventually to use only one particle / magnetic bit. (images from D. Weller (Seagate) see S. Sun, C. Murray, D. Weller, L. Folks, A. Moser, Science,287,1989 (2000))

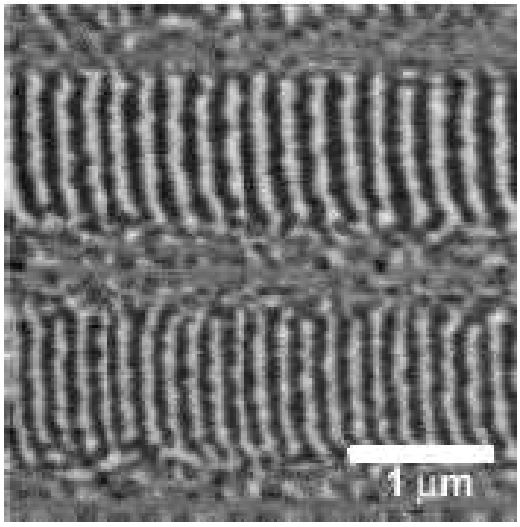

MFM image of recorded tracks (longitudinal recording). One magnetic bit contains roughly 100 magnetic grains (cobalt based) so that the information is stable against losing (i.e. reversing) a few magnetic grains. The way information is coded and physically written gives also possibilities to improve density.

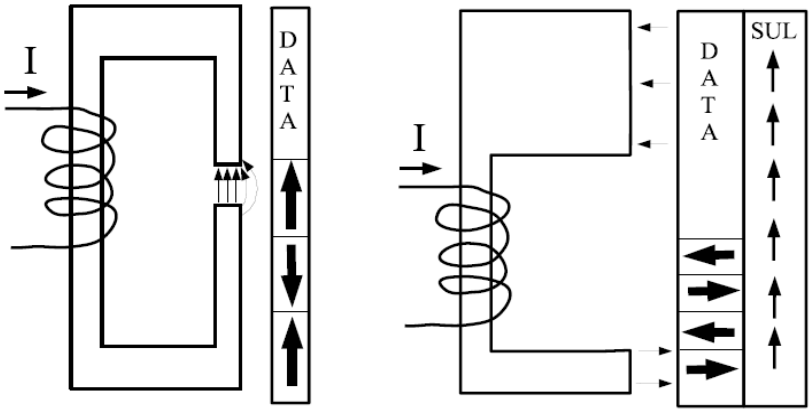

Longitudinal geometry Perpendicular geometry

Tapes, floppies and hard disks traditionally used in-plane magnetisation (longitudinal geometry). Since 2006, perpendicular magnetisation is being used in hard disks as a way to improve density. It is a major technological leap, since new media with out of plane anisotropy had to be developed and must include magnetically soft underlayers to guide the magnetic flux. Write heads and read heads had also to be redesigned for this new geometry.

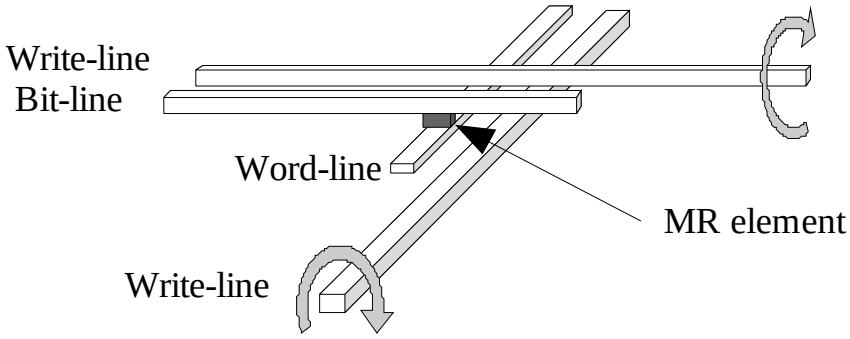

Unit cell of a magnetic RAM. First generation uses magnetic fields to reverse magnetisation. Next generations may use current to assist reversal either by decreasing the coercivity by heating the selected element or even by suppressing the need for write- lines exploiting the spin torque effect. Resistance is modified by the magnetic configuration (this is magnetoresistance). Spin torque is the opposite effect of a spin polarised current on magnetic configuration (including current-induced domain wall motion and even magnetisation reversal in small elements).

STUDIA UNIVERSITATIS BABEŞ-BOLYAI, PHYSICA, LII, 1, 2007

DEPOSITION AND GROWTH METHODS OF MEDIA FILMS, NANO-ASSEMBLED AND NANO-ORGANIZED OBJECTS, LITHOGRAPHY METHODS

JULIEN BACHMANN[*]

Current magnetic recording platforms (computer hard drives) consist of ferromagnetic thin films. Each binary bit of information is stored by an area consisting of large numbers (≈20-1000) of magnetic grains. Within this framework, size reduction driven by the need to reach ever-increasing data storage densities will at some point reach a limit, set by superparamagnetism. Indeed, below a certain size limit (related to the volume of magnetic domains), the magnetic energy of a single magnetic particle is too small relative to thermal energy for magnetic ordering to occur — the tendency of neighboring spins to align is overcome thermally, and the bit of information is lost.[1] The development of future high-density data storage platforms thus requires the preparation and systematic investigation of magnetic nanoobjects susceptible to overcome the superparamagnetic limit. The requirements on the nanoobjects are stringent:

a. *Small lateral size*
b. *Ferromagnetism along a preferred axis*
c. *Two-dimensional organization*
d. *Homogeneous, tunable geometry and magnetic parameters*

Most current research towards the synthesis of objects meeting these goals *a-d* is based on a combination of some or all of the following approaches.

A. Pseudo-1D magnetic objects. A 1D geometry allows the lateral size of the object to be reduced almost arbitrarily (*a*), while the large shape anisotropy can overcome superparamagnetism and orient the ferromagnetic response along a single axis (*b*).

B. Lithography. Various lithographic methods are available to create a perfect pattern of micrometer period or below on large areas of substrate, and subsequently transfer the pattern to a magnetic material (*c*).

C. Ordered porous templates. Several materials can be prepared with a self-ordered or lithographically ordered porous structure, such that the geometry of the pores is determined by the experimental preparative parameters —

[*] *Max Planck Institute of Microstructure Physics, Halle, Germany*
European School on Magnetism 2007, Cluj-Napoca
1. C. A. Ross, *Annu. Rev. Mater. Res.* **2001**, *31*, 203-235.

deposition of magnetic material into the pores yields organized arrays of magnetic 1D nanostructures of tunable geometry (*c*, *d*).

D. Electrodeposition. When an electrode defined at the bottom of the template pores supplies electrons to an solution containing metal cations, precipitation of the ("reduced") solid metal occurs at the electrode and then progresses upwards into the pores, thus forming nanowires (**A**) inside the template matrix.

E. Atomic layer deposition. The pore walls of the template are covered conformally with solid material deposited layer by layer by a self-limiting chemical reaction occurring at the surface between two gaseous, thermally stable, precursors. ALD thus yields nanotubes (**A**) of accurately tunable thickness (*d*).

A. Pseudo-1D magnetic objects

In a ferromagnetic object of elongated, cylindrically symmetric (oblate) geometry, the *z* axis is the "easy" axis for magnetization. In the absence of an external field, the magnetic moment of the magnetized oblate will lie along +*z* or –*z*, and magnetizing the object in another direction costs an additional energy term.[1,2] The energy difference between states magnetized in the *z* and in the *x* (or *y*) direction furnishes a quantification of the shape anisotropy of the system. If the shape anisotropy is much larger than thermal energy, the ferromagnetic state is stable and superparamagnetism is overcome. In the case of large aspect ratios (wires), however, reversing the magnetization from +*z* to –*z* by application of an external magnetic field requires less energy than rotation of the overall magnetic moment into the *(x, y)* plane, because magnetization reversal is not homogeneous: instead, it occurs via an intermediary "curling" state which has no *(x, y)* component of the magnetic moment.[3] Magnetization reversal in nanowires of very small diameter may occur only via formation of a domain boundary at one extremity and its propagation along the wire,[4] a mechanism that usually results in larger coercive fields.

B. Lithography

Lithography is based on thin films of organic materials called "resists", the chemical identity of which changes upon exposure to light or an electron beam. A pattern is "written" in the resist using a shadow mask, an interference figure, or the focused electron beam of an electron microscope, and then developed by chemical etching.

[2.] K. Nielsch and B. J. H. Stadler, in *Handbook of Magnetism and Advanced Magnetic Materials*, Vol. 4; H. Kronmüller and S. Parkin, eds.: John Wiley and Sons, Ltd., Chichester, **2007**.

[3].E. H. Frei, S. Shtrikman and D. Treves, *Phys. Rev.* **1957**, *106*, 446-454.

[4]. R. Hertel and J. Kirschner, *Physica B* **2004**, *343*, 206-210.

The pattern in the resist can subsequently be transferred to the underlying substrate by further etching steps (dry or wet chemical), or to another substrate by physical contact.[1,5,6]

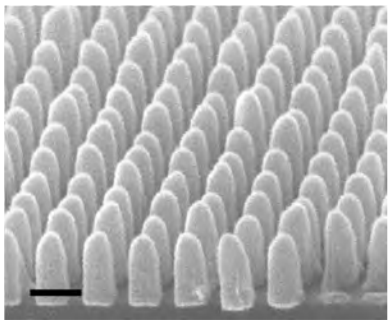

Figure 1. Array of Ni pillars obtained lithographically (scale bar: 100 nm; from Ross).[1]

Lithographic methods thus provide the ability to organize nanoobjects in perfect periodic (one- or two-dimensional) arrangements over macroscopic areas. Hexagonal and square arrays of quantum dots, disks, and pillars are achievable (Figure 1), as well as parallel alignments of wires lying "horizontally" on the substrate. However, to date lithographic techniques have not yielded arrays of wires or tubes of high aspect ratio standing "vertically" (*i. e.* with their long axis perpendicular to the substrate plane).

C. Ordered porous templates

Some materials can be obtained as micrometer-thick membranes traversed with pores, the axis of which is perpendicular to the plane of the membrane. Even if the preparation technique is particular to a specific material system (such as Al_2O_3 or TiO_2), deposition into the pores may be general. It thus allows one to obtain wires or tubes of a desired material by using the porous membrane as a template. The ordering of the nanoobjects is determined by that of the template. Chemical dissolution of the template yields isolated nanoobjects.

Ion-track-etch polycarbonate membranes, available commercially as filters for use in chemistry and biology, have been used as templates, but their pores are randomly distributed and are not aligned parallel to one another.[7] In another approach, phase separation phenomena can be used, in particular in block copolymeric systems: selective etching of a columnar phase-separated structure yields vertical hollow cylinders.[8] So-called "macroporous silicon" is obtained by electrochemical oxidation of a doped and lithographically pre-patterned Si wafer under irradiation in solutions of hydrofluoric acid.[9] The pores are nearly perfect structurally and their geometry can be adjusted experimentally, however the

[5].Y. N. Xia, J. A. Rogers, K. E. Paul and G. M. Whitesides, *Chem. Rev.* **1999**, *99*, 1823-1848.

[6].Y. N. Xia and G. M. Whitesides, *Annu. Rev. Mat. Sci.* **1998**, *28*, 153-184.

[7].M. Wirtz and C. R. Martin, *Adv. Mat.* **2003**, *15*, 455-458.

[8].B. Smarsly and M. Antonietti, *Eur. J. Inorg. Chem.* **2006**, *6*, 1111-1119.

[9].S. Ottow, V. Lehmann and H. Foll, *J. Electrochem. Soc.* **1996**, *143*, 385-390.

diameters are rather large (≥ 200 nm). Finally, porous anodic alumina (Figure 2) results from the electrochemical oxidation of aluminum in aqueous acidic solutions. Processes have been reported with and without lithographic pre-patterning that allow experimental access to pores of 20 to 400 nm diameter.[10-12]

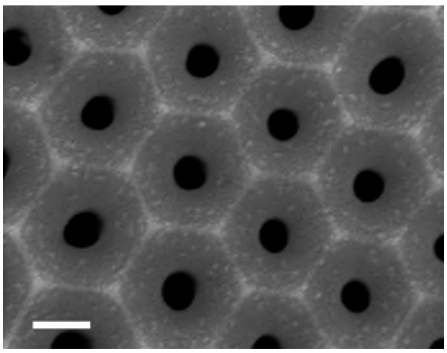

Figure 2. Top view of a sample of porous anodic alumina (scale bar: 200 nm).

D. Electrodeposition

A thick layer of conducting material deposited onto one side of a porous membrane serves as an array of nanoelectrodes placed at the bottom of each pore. Application of a suitable potential to the electrodes in a solution containing redox-active species (molecules or ions susceptible of being oxidized or reduced) can result in the precipitation of the reduced or oxidized species at the bottom of the pores. If the solid thus obtained is a sufficient electrical conductor, electrodeposition is not limited by the thickness deposited and it results in the growth of nanowires in the pores, of diameter set by the geometry of the template and of length determined by the total amount of current passed.

Ordered arrays of Ni nanowires obtained in this manner yield a very anisotropic magnetic response, and the quality of the hysteresis curve (remanence) strongly depends upon the wire diameter (Figure 3).[13-15]

Electrochemical techniques can be generalized to multisegmented wires, and such systems may give rise to interesting GMR effects.[16]

---

[10].H. Masuda, F. Hasegwa and S. Ono, *J. Electrochem. Soc.* **1997**, *144*, L127-L130.

[11].A. P. Li, F. Müller, A. Birner, K. Nielsch, U. Gösele, *Adv. Mat.* **1999**, *11*, 483-487.

[12].K. Nielsch, J. Choi, K. Schwirn, R. B. Wehrspohn and U. Gösele, *Nano Lett.* **2002**, *2*, 677-680.

[13]. K. Nielsch, F. Müller, A.-P. Li and U. Gösele, *Adv. Mater*. **2000**, *12*, 582-586.

[14].K. Nielsch, R. B. Wehrspohn, J. Barthel, J. Kirschner, U. Gösele U, S. F. Fischer and H. Kronmüller, *Appl. Phys. Lett.* **2001**, *79*, 1360-1362.

[15].K. Nielsch, R. B. Wehrspohn, J. Barthel, J. Kirschner, S. F. Fischer, H. Kronmüller, T. Schweinbock, D. Weiss and U. Gösele, *J. Magn. Magn. Mat.* **2002**, *249*, 234-240.

[16].L. Piraux, J. M. George, J. F. Despres, C. Leroy, E. Ferain, R. Legras, K. Ounadjela and A. Fert, *Appl. Phys. Lett.* **1994**, *65*, 2484-2486.

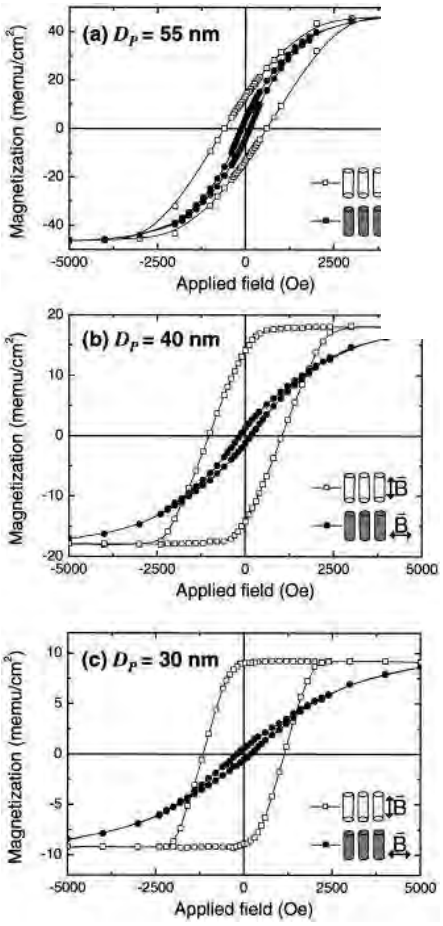

Figure 3. Magnetic characteristics of electrodeposited Ni nanowire arrays of three different outer diameters D_p (from Nielsch *et al.*).[14]

Figure 4. An array of Fe_2O_3 nanotubes in the porous anodic alumina matrix (scale bar: 200 nm; from Bachmann *et al.*).

E. Atomic layer deposition

Alternated exposure of a surface to two gaseous reactants that are thermally stable at the reaction temperature but very reactive towards each other results in the chemisorption of successive monolayers of each reactant (independently of the excess amount of reactants in the gas phase), in a self-limited growth mode called atomic layer deposition (ALD). The thickness of a solid film deposited by ALD only depends on the number of reaction cycles performed, not on other experimental parameters such as the vapor pressure of precursors. Therefore, employing excess amounts of precursors allows one to coat substrates of arbitrarily complex geometry, in particular very porous ones. These characteristics make ALD the only gas-solid deposition technique not limited to a flat substrate geometry, and thereby able to grow nanotubes in porous templates (as opposed to CVD for example).[1,1] ALD combined with porous anodic alumina templates has allowed magnetic nanotubes of Co, Ni and Fe_3O_4 to be obtained in ordered arrays and with well-controlled geometry (Figure 4).[1,1] Systematic tuning of their geometric parameters reveals different magnetization reversal modes depending on geometry.[1]

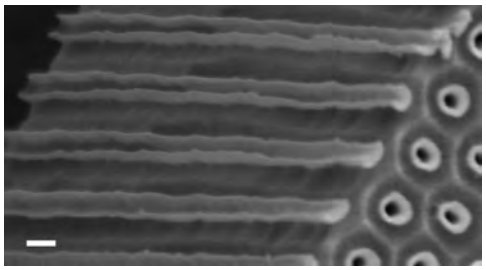

STUDIA UNIVERSITATIS BABEŞ-BOLYAI, PHYSICA, LII, 1, 2007

EXCHANGE BIAS, GIANT MAGNETORESISTANCE, TUNNEL MAGNETORESISTANCE AND MAGNETIC RANDOM ACCESS MEMORIES

J. M. DE TERESA*

The study of electrical transport in magnetic materials has a long history. However, since the discovery in 1988 of the so-called giant magnetoresistance (GMR) in metallic multilayers [1], the subject has generated a great deal of interest. This was important not only from the basic research point of view but also from the applied research point of view. In 1997 IBM introduced in the hard-disk technology magnetoresistive read heads based on the GMR effect, which has allowed the increase in the density of the stored information in hard disks at a rate much beyond previous technologies [2]. GMR can be considered to be the first paradigm of the so-called ***Spin Electronics***, where, in sharp contrast with semiconductor technology, the spin as well as the charge transport is taken into account. This field could be developed thanks to the fine nanometric control of thin films in the growth direction .

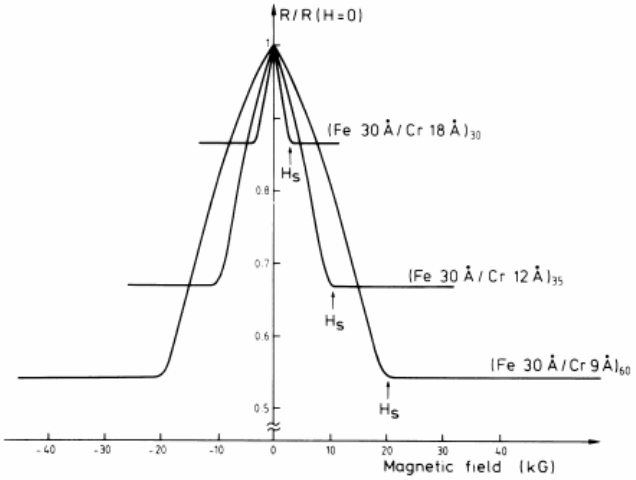

Figure 1. Original figure included in reference [1], where the GMR effect was first reported

* Instituto de Ciencia de Materiales de Aragón, Universidad de Zaragoza-CSIC, Facultad de Ciencias, 50009 Zaragoza, Spain.
E-mail: deteresa@unizar.es
Webpage: http://www.unizar.es/departamentos/fisica_mat_condensada/people/deteresa/

In my talk I will start by introducing the basic concepts to understand the transport properties in magnetic solids. From the form of the resistivity tensor that relates the electric field and the current in a solid [3], I will introduce the concepts of anisotropic magnetoresistance, the ordinary and extraordinary Hall effect and the planar Hall effect. I will show some experimental examples of these phenomena and discuss the microscopic origin where basic ingredients are the Lorentz force acting upon the carriers and the spin-orbit interaction.

A new perspective for new magnetoresistive phenomena in magnetic heterostructures was open after the discovery of GMR in the late eighties [1] as explained before. GMR was observed in multilayers composed of alternating magnetic and non-magnetic layers. Basic ingredients to understand this effect are the different bulk and interface scattering probability of spin-up and spin-down conduction electrons, the spin-diffusion length compared to the layers thickness, the magnetic exchange coupling between the magnetic layers, the spin-accumulation effects, etc [2, 4]. In my talk I will first discuss the basic experiments that allow the understanding of this effect such as the magnetoresistance as a function of the non-magnetic and magnetic layers thickness, the influence of interface doping, etc. I will also discuss the difference between the current-in-plane (CIP) and current-perpendicular-to-plane (CPP) GMR geometries. The GMR effect can be also observed in granular materials containing magnetic and non-magnetic materials [5] and I will also show some example in this kind of system.

In order for the GMR to be of practical use, some technological improvements have been required. In that sense, I will discuss the spin-valve concept, which was developed in the early nineties at IBM [6] and allows one to obtain the full GMR effect at low magnetic field. This technology requires only two ferromagnetic layers separated by one non-magnetic layer and the exchange-biasing of one of the ferromagnetic layers with an antiferromagnetic layer. As the spin-dependent process only takes place along a few layers in the spin-valve device, the magnetoresistance ratio at room temperature is typically below 20%. In some applications a linear response of the GMR effect as a function of the magnetic field is desired. Some strategies have been envisaged to obtain such a response but one of the most used technologies is the crossed geometry of the easy axes of the ferromagnetic layers in a spin-valve configuration [7].

Another important phenomenon leading to very large magnetoresistance ratios has attracted much interest in recent years: the tunnel magnetoresistance effect (TMR). The TMR effect was proposed by Jullière in 1975 [8] but it was not actually developed until the late nineties [9]. Basically it consists of two ferromagnetic layers (electrodes) separated by a thin nanometric insulating layer (barrier). The conduction proceeds via electron tunnelling and the electrical resistance of such a device is different if the ferromagnetic layers have parallel or antiparallel magnetizations.

The origin of this effect lies at the different tunnelling probability of spin-up and spin-down electrons.

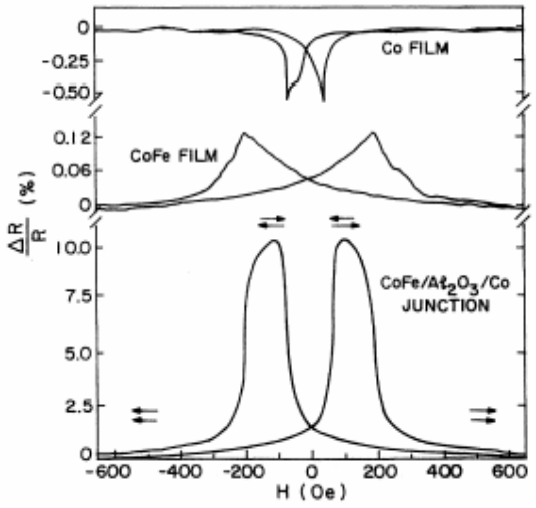

Figure 2. Original figure included in reference [9], where reproducible and large TMR values were first reported.

Jullière proposed that the TMR ratio only depends on the spin polarization at the Fermi level of the ferromagnetic materials (P_1, P_2): $TMR=100x(R_{AP}-R_P)/R_P=100xP_1P_2/(1-P_1P_2)$. The spin polarization at the Fermi level can be measured for example with the technique developed by Tedrow and Meservey [10]. By using CoFe ferromagnetic materials and Al_2O_3 barriers, high TMR ratios at room temperature (50%) have been achieved [11]. Motorola already announced in 2003 a 4-Mbit magnetic random access memory (MRAM) based on this kind of tunnel junctions implemented on the 180 nm CMOS technology and several companies are striving to place MRAM on the market [12]. The use of half-metallic ferromagnetic electrodes ($P=\pm1$) is very promising for getting the maximum TMR response. In fact, TMR ratios greater than 1000% were demonstrated at low temperature by using manganite electrodes but in these manganite-based junctions the response vanishes at room temperature [13]. An important step towards the understanding of the TMR came from experiments in junctions with one half-metal electrode ($La_{0.7}Sr_{0.3}MnO_3$), different barriers (Al_2O_3, $SrTiO_3$, Ce_xO_y) and interfaces, and a Co counter-electrode which showed that the TMR depends on bonding effects at the interface and can even give rise to inverse TMR (lower resistance in the antiparallel magnetic configuration of the electrodes) [14]. Definitely, this discovery fostered the use of new barriers and epitaxial junctions, where the

response can be enhanced with respect to traditional Al_2O_3–based junctions. One of the most promising systems is Fe/MgO/Fe, where very large TMR ratios were found at room temperature [15]. This finding has made MgO barriers the most promising ones for applications at room temperature (MR>350%) and is nowadays the leading technology in devices making use of magnetic tunnel effects [16].

REFERENCES

1. M. Baibich et al., Phys. Rev. Lett. 61, 2472 (1988)
2. "Spin dependent transport in magnetic nanostructures", edited by S. Maekawa and T. Shinjo. Advances in condensed matter science, volume 3, Taylor and Francis 2002.
3. I.A. Campbell and A. Fert, "Transport properties of ferromagnets", Magnetic Materials, Vol. 3, Holland Publishing Company, 1982.
4. A. Barthélémy et al., "Giant magnetoresistance in magnetic multilayers", Handbook of magnetic materials, vol. 12, edited by K.H.J. Buschow, Elsevier Science 1999.
5. A.E. Berkowitz et al., Phys. Rev. Lett. 68, 3745 (1992); J.Q. Xiao et al., Phys. Rev. Lett. 68, 3749 (1992); X. Batlle and A. Labarta, J.Phys. D: Appl. Phys. 35, R15 (2002)
6. B. Dieny et al., Phys. Rev. B 43, 1297 (1991)
7. T. Rijks et al., Appl. Phys. Lett. 65, 916 (1994)
8. M. Jullière, Phys. Lett. A 54, 225 (1975)
9. J. Moodera et al., Phys. Rev. Lett. 74, 3273 (1995)
10. R. Meservey and P.M. Tedrow, Phys. Rep. 238, 173 (1994)
11. M. Tsunoda et al., Appl. Phys. Lett. 80, 3135 (2002); S. Colis et al., Appl. Phys. Lett. 83, 948 (2003)
12. http://www.mram-info.com/
13. M. Bowen et al., Appl. Phys. Lett. 82, 233 (2003)
14. J. M. De Teresa et al., Phys. Rev. Lett. 82 (1999) 4288 and J. M. De Teresa et al., Science 286 (1999) 509
15. M. Bowen et al., Appl. Phys. Lett. 79, 1655 (2001); J. Faure-Vincent et al., Appl. Phys. Lett. 82, 4207 (2002); S.S.P. Parkin, Nature Materials 3, 862 (2004); S. Yuasa et al., Nature Materials 3, 868 (2004); D.D. Djayaprawira et al., Appl. Phys. Lett. 86, 092502 (2005)
16. S.S.P. Parking, MRS Bulletin 31, 389 (2006)

STUDIA UNIVERSITATIS BABEŞ-BOLYAI, PHYSICA, LII, 1, 2007

SENSORS AND ACTUATORS

J. M. DE TERESA*

Sensors have been used as detection elements for past decades. One simple and common example is the mercury thermometer used to measure the body temperature that relies on the Physical property called thermal expansion. In general, a sensor needs a **transducer** that transforms the measured magnitude in another one that is easier to interpret or visualize. Nowadays, most sensors require combination with electronic devices. The use of sensors has considerably increased in the last years due to the development of **electronic signal processing**. The domains of application of sensors cover fields such as medical instrumentation, automotive industry, industrial measurements, environment control, energy sources, safety, electrical appliances, chemical industry, etc.

"To sense" implies to detect properties such as the temperature, humidity, pressure, magnetic field, displacement, speed, chemical composition, light colour and intensity, etc. In order to accomplish its function, a sensor relies on a **Chemical or Physical effect**. Thus, a temperature sensor like a thermocouple makes use of the Seebeck effect that gives rise to a voltage difference between terminals at different temperature and a magnetic sensor such as a Hall sensor makes use of the Hall effect due to the Lorentz force acting on electrical carriers. The materials used to create sensors can be ceramic, organic, metallic, composite, etc. and can be realized in bulk form or in thin-film form. In the latter case, it is especially interesting the **integration** of the thin-film sensor with the electronics in a semiconductor-based integrated circuit, which brings about smaller and generally more efficient sensors. If the sensing takes place via the use of a biological recognition event, we talk about **biosensors**. Biosensors is a fast growing field because it can allow precise sensing of molecules and biomolecules. In combination with Nanotechnology, we would enter the realm of Nanobiosensors, which is presently a fancy topic.

In my talk I will start by giving general notions on sensors such as those described in the previous paragraphs and I will describe a few examples [1]. Afterwards, I will focus on **magnetic sensors**, which is the topic of interest in the School. In this context, I will describe **inductive sensors, Hall sensors, magnetoresistive sensors (AMR. GMR, TMR), SQUID sensors**, etc. These sensors have a wide range of

* Instituto de Ciencia de Materiales de Aragón, Universidad de Zaragoza-CSIC, Facultad de Ciencias, 50009 Zaragoza, Spain.
E-mail: deteresa@unizar.es
Webpage: http://www.unizar.es/departamentos/fisica_mat_condensada/people/deteresa/

applications in fields such as automotive industry, magnetic storage industry, aeronautic industry, industrial applications, magnetic field sensing, safety, magnetoencephalography, DNA biochips, etc [2-11].

Afterwards, I will focus on **magnetic biosensors**, which is a relatively new and very promising field. Two approaches can be realized depending if the biological recognition and the detection take place on the same platform (lab-on-a-chip technology) or on separate platforms. **Lab-on-a-chip** technology is generally preferred as allows integration with the electronics but it is somewhat complex to build when dealing with liquid samples. In such cases, **microfluidic** devices are normally realized. In many cases, magnetic biosensors require tagging the biological recognition event via **magnetic nanoparticles** and their functionalization. I will describe one kind of magnetic biosensor that we are developing in our Group in order to measure concentrations of a targeted analyte present in a solution via immunochromatographic (lateral-flow) tests. These kinds of biosensor are normally applied for clinical diagnosis. In our case, the detection of the functionalised magnetic nanoparticles has been carried out with inductive sensors and with magnetoresistive sensors [12].

In the last part of my talk, I will introduce the concept of "actuation". **Actuators** are devices that transform an input signal (mainly electrical) into motion. Typical examples are electrical motors, relays, piezoelectric actuators, etc. To meet the audience's interests, I will put emphasis on the description of **magnetic actuators**. In such systems, magnetic materials are used to produce a mechanical device that generates and controls motion. Input electrical energy in the form of voltage and current is converted to magnetic energy, which produces a magnetic force able to generate motion. Applications of magnetic actuators can be found in valves and fuel injectors in automotive and aeronautic applications, biomedical prosthesis (in hearts, limbs, ears), head positioners for computer disk drives, loudspeakers, relays, switchgears, sonars, etc.

Since computers have input and outputs that are electrical signals, magnetic actuators are ideal for computer control of motion. Motion control that was in the past accomplished by manual command is now increasingly carried out by computers with magnetic sensors as their input interface and magnetic actuators as their output interface. An area of increasing development is that of magnetic actuation at the micro- and nano-scales. In this sense, the maximum integration of the actuator with the electronics is desired in order to reach miniaturization and efficiency. The recent advancements in micro- and nano-fabrication techniques habilitate the progress in this field.

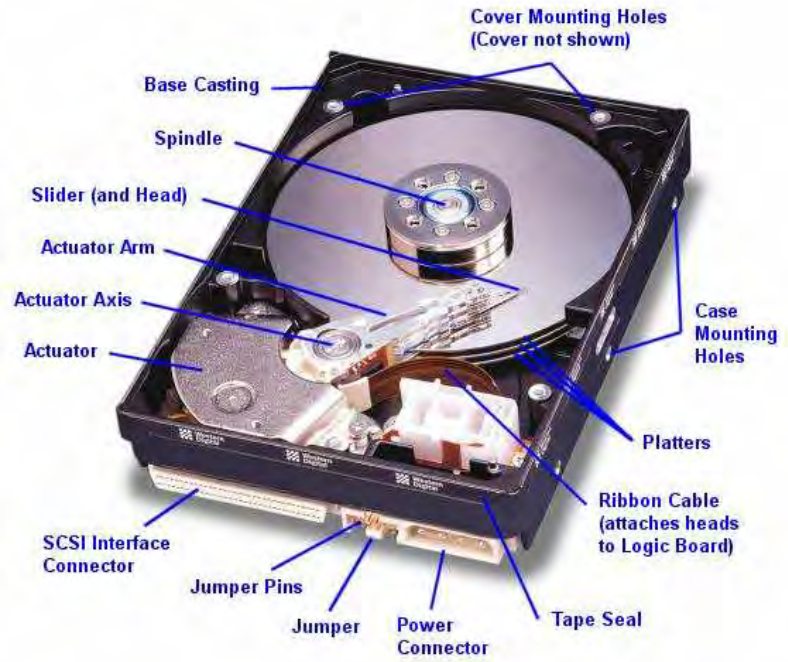

Figure 1. Disk drive picture. A **magnetic actuator** allows the positioning of the writing/reading head at the desired postion. The reading process takes place through the change in resistance produced by the stray magnetic fields arising from the magnetic bits on a **magnetoresistive sensor** located at the head tip. This is just one example of how magnetic sensors and actuators are integrated in today's technology.

REFERENCES

1. N. Ichinose and T. Kobayashi, "Guide Pratique des Capteurs", Masson, Paris 1990
2. F. Montaigne et al., Sensors and Actuators 81, 324 (2000)
3. H.A. Ferreira et al., J. Appl. Phys. 99, 08P105 (2006)
4. Li et al., J. Appl. Phys. 99, 08P107 (2006)
5. D.R. Baselt et al., Biosensors and Bioelectronics 13 (1998) 731
6. M.M. Miller et al., J. Magn. Magn. Mater. 225 (2001) 138
7. W. Shen et al., Appl. Phys. Lett. 86 (2005) 253901P.P Freitas et al., Europhysics News 34 (2003) 224
9. R. Ferreira et al., J. Appl. Phys. 99, 08K706 (2006)
10. M. Pannetier et al., Science 304, 1648 (2004)
11. A.H. Peruski et al., Clinical and Diagnostic Laboratory Immunology 10, 503 (2006)

12. J. M. De Teresa et al., manuscript in preparation. Patents: P200603259 and P200603262

STUDIA UNIVERSITATIS BABEŞ-BOLYAI, PHYSICA, LII, 1, 2007

INTRODUCTION TO MAGNETIC REFRIGERATION

E. BRÜCK*

Magnetic refrigeration, based on the magnetocaloric effect (MCE), has recently received increased attention as an alternative to the well-established compression-evaporation cycle for room-temperature applications. Magnetic materials contain two energy reservoirs; the usual phonon excitations connected to lattice degrees of freedom and magnetic excitations connected to spin degrees of freedom. These two reservoirs are generally well coupled by the spin lattice coupling that ensures loss-free energy transfer within millisecond time scales. An externally applied magnetic field can strongly affect the spin degree of freedom that results in the MCE. In the magnetic refrigeration cycle, depicted in fig. 1, initially randomly oriented magnetic moments are aligned by a magnetic field, resulting in heating of the magnetic material. This heat is removed from the material to the ambient by heat transfer. On removing the field, the magnetic moments randomise, which leads to cooling of the material below ambient temperature. Heat from the system to be cooled can then be extracted using a heat-transfer medium. Depending on the operating temperature, the heat-transfer medium may be water (with antifreeze) or air, and for very low temperatures helium. The cycle described here is very similar to the vapour compression refrigeration cycle: on compression the temperature of a gas increases, in the condenser this heat is expelled to the environment and on expansion the gas cools below ambient temperature and can take up heat from the environment. In contrast to a compression cycle the magnetic refrigeration cycle can be performed quasi static which results in the possibility to operate close to Carnot efficiency.

Therefore, magnetic refrigeration is an environmentally friendly cooling technology. It does not use ozone depleting chemicals (CFCs), hazardous chemicals (NH_3), or greenhouse gases (HCFCs and HFCs). The difference between vapour-cycle refrigerators and magnetic refrigerators manifests itself also is the amount of energy loss incurred during the refrigeration cycle. From thermodynamics it appears feasible to construct magnetic refrigerators that have very high Carnot efficiency compared to conventional vapour pressure refrigerators [1, 2]. This higher energy efficiency will also result in a reduced CO_2 release. Current research aims at new magnetic materials displaying larger magnetocaloric effects, which then can be operated in fields of about 2 T or less, that can be generated by permanent magnets.

* Van der Waals–Zeeman Instituut, Universiteit van Amsterdam, Valckenierstr. 65, 1018 XE Amsterdam, The Netherlands

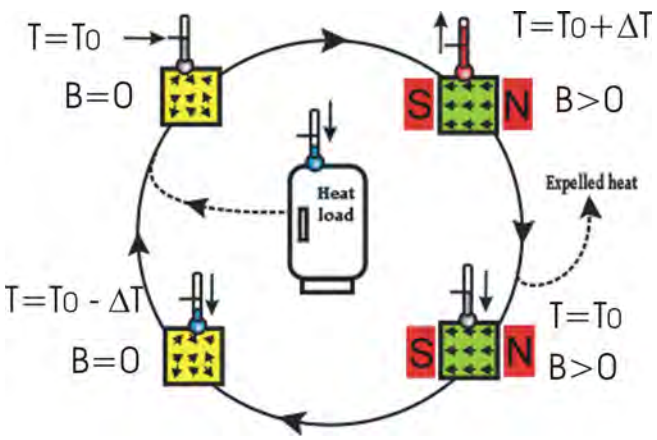

Figure 1. Schematic representation of a magnetic-refrigeration cycle, which transports heat from the heat load to the ambient. Left and right depict material in low and high magnetic field, respectively.

The heating and cooling described above is proportional to the change of magnetization and the applied magnetic field. This is the reason that, until recently, research in magnetic refrigeration was almost exclusively conducted on super-paramagnetic materials and on rare-earth compounds [3]. For room-temperature applications like refrigerators and air-conditioners, compounds containing manganese or iron should be a good alternative. Manganese and iron are transition metals with high abundance. Also, there exist in contrast to rare-earth compounds, an almost unlimited number of manganese and iron compounds with critical temperatures near room temperature. However, the magnetic moment of manganese generally is only about half the size of heavy rare-earth elements and the magnetic moment of iron is even less. Enhancement of the caloric effects associated with magnetic moment alignment may be achieved through the induction of a first order phase-transition or better a very rapid change of magnetisation at the critical temperature, which will bring along a much higher efficiency of the magnetic refrigerator. In combination with currently available permanent magnets [4], based on modern Rare-Earth Transition-metal compounds [5], this opens the path to the development of small-scale magnetic refrigerators, which no more rely on rather costly and service-intensive superconducting magnets. Another prominent advantage of magnetocaloric refrigerators is that the cooling power can be varied by scaling from milliwatt to a few hundred watts or even kilowatts. To increases the temperature span of the refrigerator, in comparison with the temperature change in a single cycle, all demonstrators or prototypes nowadays are based on the active magnetic regenerator design [6].

$Gd_5Ge_2Si_2$ type compounds

Following the discovery of a sub-room temperature giant-MCE in the ternary compound $Gd_5(Ge_{1-x}Si_x)_4$ ($0.3 \leq x \leq 0.5$)[7], there is a strongly increased interest from both fundamental and practical points of view to study the MCE in these materials [8, 9]. The most prominent feature of these compounds is that they undergo a first-order structural and magnetic phase transition, which leads to a giant magnetic field-induced entropy change, across their ordering temperature. We here therefore will discuss to some extend the structural properties of these compounds. At low temperatures for all x $Gd_5(Ge_{1-x}Si_x)_4$ adopts an orthorhombic Gd_5Si_4-type structure (Pnma) and the ground state is ferromagnetic[10]. However, at room temperature depending on x three different crystallographic phases are observed. For $x > 0.55$ the aforementioned Gd_5Si_4 structure is stable, for $x < 0.3$ the materials adopt the Sm_5Ge_4-type structure with the same space group (Pnma) but a different atomic arrangement and a somewhat larger volume, finally in between these two structure types the monoclinic $Gd_5Si_2Ge_2$ type with space group ($P112_1/a$) is formed, which has an intermediate volume. The latter structure type is stable only below about 570K where again the orthorhombic Gd_5Si_4-type structure is formed in a first-order phase transition[11]. As one may guess, the three structure types are closely related; the unit cells contain four formula units and essentially only differ in the mutual arrangement of identical building blocks which are either connected by two, one or no covalent-like Si-Ge bonds, resulting in successively increasing unit-cell volumes. The giant magnetocaloric effect is observed for the compounds that exhibit a simultaneous paramagnetic to ferromagnetic and structural phase-transition that can be either induced by a change in temperature, applied magnetic field or applied pressure[12, 13]. In contrast to most magnetic systems the ferromagnetic phase has a 0.4% smaller volume than the paramagnetic phase which results in an increase of Tc on application of pressure with about 3K/kbar. The structural change at the phase transition brings along also a very large magneto-elastic effect and the electrical resistivity behaves anomalous. The strong coupling between lattice degrees of freedom and magnetic and electronic properties is rather unexpected, because the magnetic moment in Gd originates from spherical symmetric s-states that in contrast to other rare-earth elements hardly couple with the lattice. First principle electronic structure calculations in atomic sphere and local-density approximation with spin-orbit coupling added variationally, could reproduce some distinct features of the phase transition [14]. Total energy calculations for the two phases show different temperature dependences and the structural change occurs at the temperature where the energies are equal. There appears a distinct difference in effective exchange-coupling parameter for the monoclinic and orthorhombic phase, respectively. This difference could directly be related to the change of the Fermi-level in the structural transition. Thus the fact that the structural and magnetic transitions are simultaneous is somewhat accidental as

the exchange energy is of the same order of magnitude as the thermal energy at the structural phase-transition. The electrical resistivity and magneto resistance of $Gd_5Ge_2Si_2$ also shows unusual behaviour, indicating a strong coupling between electronic structure and lattice. For several compounds of the series, next to a cusp like anomaly in the temperature dependence of the resistivity, a very large magnetoresistance effect is reported[15-18].

In view of building a refrigerator based on $Gd_5 (Ge_{1-x}Si_x)_4$, there are a few points to consider. The largest magnetocaloric effect is observed considerably below room temperature, while a real refrigerator should expel heat at least at about 320K. Because the structural transition is connected with sliding of building blocks, impurities especially at the sliding interface can play an important role. The thermal hysteresis and the size of the magnetocaloric effect connected with the first-order phase transition strongly depend on the quality of the starting materials and the sample preparation[19]. For the compounds $Gd_5 (Ge_{1-x}Si_x)_4$ with x around 0.5 small amounts of impurities may suppress the formation of the monoclinic structure near room temperature. These alloys then show only a phase transition of second order at somewhat higher temperature but with a lower magnetocaloric effect[11, 20, 21]. This sensitivity to impurities like carbon, oxygen and iron strongly influences the production costs of the materials which may hamper broad-scale application. Next to the thermal and field hysteresis the magneto-structural transition in $Gd_5 (Ge_{1-x}Si_x)_4$ appears to be rather sluggish[22, 23]. This will also influence the optimal operation-frequency of a magnetic refrigerator and the efficiency.

La $(Fe,Si)_{13}$ and related compounds

Another interesting type of materials are rare-earth - transition-metal compounds crystallizing in the cubic $NaZn_{13}$ type of structure. $LaCo_{13}$ is the only binary compound, from the 45 possible combinations of an rare-earth and iron, cobalt or nickel, that exists in this structure. It has been shown that with an addition of at least 10% Si or Al this structure can also be stabilized with iron and nickel[24]. The $NaZn_{13}$ structure contains two different Zn sites. The Na atoms at 8a and Zn^I atoms at 8b form a simple CsCl type of structure. Each Zn^I atom is surrounded by an icosahedron of 12 Zn^{II} atoms at the 96i site. In La (Fe,Si)13 La goes on the 8 a site, the 8b site is fully occupied by Fe and the 96i site is shared by Fe and Si. The iron rich compounds La $(Fe,Si)_{13}$ show typical invar behavior, with magnetic ordering temperatures around 200K that increase to 262K with lower iron content[25]. Thus, though the magnetic moment is diluted and also decreases per Fe atom, the magnetic ordering temperature increases. Around 200K the magnetic-ordering transition is found to be also distinctly visible in the electrical resistivity, where a chromium-like cusp in the temperature dependence is observed. In contrast to $Gd_5Ge_2Si_2$ this phasetransition is not accompanied by a structural change, thus above and below T_c the material is cubic. Recently, because of the extremely sharp magnetic ordering transition, the (La,Fe,Si,Al)

system was reinvestigated by several research groups and a large magnetocaloric effect was reported[26-28]. The largest effects are observed for the compounds that show a field- or temperature-induced phase-transition of first order. Unfortunately, these large effects only occur up to about 210 K as the magnetic sublattice becomes more and more diluted. When using standard melting techniques, preparation of homogeneous single-phase samples appears to be rather difficult especially for alloys with high transition metal content. Almost single phase samples are reported when, instead of normal arc melting, rapid quenching by melt spinning and subsequent annealing is employed[29-31]. Samples prepared in this way also show a very large magnetocaloric effect. To increase the magnetic ordering temperature without loosing too much magnetic moment, one may replace some Fe by other magnetic transition-metals. Because the isostructural compound $LaCo_{13}$ has a very high critical temperature substitution of Co for Fe is widely studied. The compounds La $(Fe,Co)_{13-x}Al_x$ and La $(Fe,Co)_{13-x}Si_x$ with $x \approx 1.1$ and thus a very high transition-metal content, show a considerable magnetocaloric effect near room temperature[32-35]. This is achieved with only a few percent of Co and the Co content can easily be varied to tune the critical temperature to the desired value. It should be mentioned however that near room temperature the values for the entropy change steeply drop.

Hydrogen is the most promising interstitial element. In contrast to other interstitial atoms, interstitial hydrogen not only increases the critical temperature but also leads to an increase in magnetic moment[27, 36-40]. The lattice expansion due to the addition of three hydrogen atoms per formula unit is about 4.5%. The critical temperature can be increased to up to 450K, the average magnetic moment per Fe increases from 2.0 μ_B to up to 2.2 μ_B and the field- or temperature-induced phase-transition is found to be of first-order for all hydrogen concentrations. This all results for a certain Si percentage in an almost constant value of the magnetic entropy change per mass unit over a broad temperature span.

From the materials cost point of view the La $(Fe,Si)_{13}$ type of alloys appear to be very attractive. La is the cheapest from the rare-earth series and both Fe and Si are available in large amounts. The processing will be a little more elaborate than for a simple metal alloy but this can be optimized. For the use in a magnetic refrigerator next to the magnetocaloric properties also mechanical properties and chemical stability may be of importance. The hydrogenation process of rare-earth transition-metal compounds produces always granular material due to the strong lattice expansion. In the case of the cubic $NaZn_{13}$ type of structure this does not seem to be the case. At the phase transition in La $(Fe,Si)_{13}$ type of alloys also a volume change of 1.5% is observed[41]. If this volume change is performed very frequently the material will definitely become very brittle and probably break in even smaller grains. This can have distinct influence on the corrosion resistance of the material and thus on the lifetime of a refrigerator. The suitability of this material definitely needs to be tested.

MnAs based compounds

MnAs exist similar to $Gd_5Ge_2Si_2$ in two distinct crystallographic structures[42]. At low and high temperature the hexagonal NiAs structure is found and for a narrow temperature range 307 K to 393 K the orthorhombic MnP structure exists. The high temperature transition in the paramagnetic region is of second order. The low temperature transition is a combined structural and ferro-paramagnetic transition of first order with large thermal hysteresis. The change in volume at this transition amounts to 2.2%[43]. The transition from paramagnetic to ferromagnetic occurs at 307K, the reverse transition from ferromagnetic to paramagnetic occurs at 317K. Very large magnetic entropy changes are observed in this transition[44, 45]. Similar to the application of pressure[46, 47] substitution of Sb for As leads to lowering of T_c[48, 49], 25% of Sb gives an transition temperature of 225 K. However, the thermal hysteresis is affected quite differently by hydrostatic pressure or Sb substitution. In Mn (As,Sb) the hysteresis is strongly reduced and at 5% Sb it is reduced to about 1 K. In the concentration range 5 to 40% of Sb T_C can be tuned between 220 and 320 K without loosing much of the magnetic entropy change[50, 51]. Direct measurements of the temperature change confirm a ΔT of 2K/T[52]. On the other hand MnAs under pressure shows an extremely large magnetic entropy change[53] in conjunction with large hysteresis.

The materials costs of MnAs are quite low, processing of As containing alloys is however complicated due to the biological activity of As. In the MnAs alloy the As is covalently bound to the Mn and would not be easily released into the environment. However, this should be experimentally verified, especially because in an alloy frequently second phases form that may be less stable. The change in volume in Mn (As,Sb) is still 0.7% which may result in aging after frequent cycling of the material.

Heusler Alloys

Heusler Alloys frequently undergo a martensitic transition between the martensitic and the austenitic phase which is generally temperature induced and of first order. Ni_2MnGa orders ferromagnetic with a Curie temperature of 376 K, and a magnetic moment of 4.17 μ_B, which is largely confined to the Mn atoms and with a small moment of about 0.3 μ_B associated with the Ni atoms[54]. As may be expected from its cubic structure, the parent phase has a low magneto-crystalline anisotropy energy (H_a = 0.15 T). However, in its martensitic phase the compound is exhibiting a much larger anisotropy (H_a = 0.8 T). The martensitic-transformation temperature is near 220 K. This martensitic transformation temperature can be easily varied to around room temperature by modifying the composition of the alloy from the stoichiometric one. The low-temperature phase evolves from the parent phase by a diffusionless, displacive transformation leading to a tetragonal structure, a = b =

5.90 Å, c=5.44 Å. A martensitic phase generally accommodates the strain associated with the transformation (this is 6.56% along *c* for Ni_2MnGa) by the formation of twin variants. This means that a cubic crystallite splits up in two tetragonal crystallites sharing one contact plane. These twins pack together in compatible orientations to minimize the strain energy (much the same as the magnetization of a ferromagnet may take on different orientations by breaking up into domains to minimize the magneto-static energy). Alignment of these twin variants by the motion of twin boundaries can result in large macroscopic strains. In the tetragonal phase with its much higher magnetic anisotropy, an applied magnetic field can induce a change in strain why these materials may be used as actuators. Next to this ferromagnetic shape memory effect, very close to the martensitic transition temperature, one observes a large change in magnetization for low applied magnetic fields. This change in magnetization is also related to the magnetocrystalline anisotropy. This change in magnetization is resulting in a moderate magnetic entropy change of a few J/molK, which is enhanced when measured on a single crystal[55, 56]. When the composition in this material is tuned in a way that the magnetic and structural transformation occurs at the same temperature, the largest magnetic entropy changes are observed[57-59].

For magnetocaloric applications the extremely large length changes in the martensitic transition will definitely result in aging effects. It is well known for the magnetic shape-memory alloys that only single crystals can be frequently cycled while polycrystalline materials spontaneously powderize after several cycles.

Fe_2P based compounds

The binary intermetallic compound Fe_2P can be considered as the parent alloy for an interesting type of materials. This compound crystallizes in the hexagonal non centre-symmetric Fe_2P type structure with space group $P\bar{6}2m$. In this structure Fe and P occupy four different crystallographic sites, Fe occupies the 3g and 3f sites and P the 1b and 2c sites. Thus one has a stacking of alternating P-rich and P-poor layers. Neutron diffraction revealed that the magnetic moment of Fe on the 3g sites is about 2 μ_B whereas the moment on the 3f sites is about 1 μ_B[60]. The Curie temperature of this compound is 216 K and the magnetic transition is of first order [61]. The magnetic-ordering transition from the paramagnetic state to the ferromagnetic state is accompanied by a discontinuous change of the volume of 0.05%. Thus, the ferromagnetic state has a higher volume than the paramagnetic one. This phase transition is found to be extremely sensitive to changes in pressure or magnetic field. Application of pressure first reduces the Curie temperature and at pressures exceeding 5 kbar antiferromagnetic ordering preceding the ferromagnetic ordering is observed [62]. Substitution of As, B or Si into the P sublattice results in an increase of the Curie temperature [63], which can easily be lifted to above room temperature for As or Si concentrations of 10% or by 4% of

B. Substitution of Mn for Fe on the 3g sites further increases the magnetic moment to about 4 μ_B. To stabilize the Fe_2P-type of structure, simultaneously to the Mn substitution also part of the P should be replaced.

The most extensively studied series of alloys is of the type MnFe (P,As). The magnetic phase diagram for the system MnFeP-MnFeAs [64] shows a rich variety of crystallographic and magnetic phases. The most striking feature is the fact that for As concentrations between 30 and 65% the hexagonal Fe_2P type of structure is stable and the ferromagnetic order is accompanied by a discontinuous change of volume. While the total magnetic moment is not affected by changes of the composition, the Curie temperature increases from about 150 K to well above room temperature. We reinvestigated this part of the phase diagram [65, 66] and investigated possibilities to partially replace the As [67-69].

The large MCE observed in Fe_2P based compounds originates from a field-induced first-order magnetic phase transition. The magnetisation is reversible in temperature and in alternating magnetic field. The magnetic ordering temperature of these compounds is tuneable over a wide temperature interval (200 K to 450K). The excellent magnetocaloric features of the compounds of the type MnFe (P,Si,Ge,As), in addition to the very low material costs, make it an attractive candidate material for a commercial magnetic refrigerator. However same as for MnAs alloys it should be verified that materials containing As do not release this to the environment. The fact that the magneto-elastic phase-transition is rather a change of c/a than a change of volume, makes it feasible that this alloy even in polycrystalline form will not experience severe aging effects after frequent magnetic cycling.

REFERENCES

1. G.V. Brown, *Journal of Applied Physics*. **47** (1976): p. 3673-3680
2. W.A. Steyert, *Journal of Applied Physics*. **49** (1978): p. 1216-1226
3. A.M. Tishin, *Magnetocaloric effect in the vicinity of magnetic phase transitions*, in *Handbook of Magnetic Materials*, K.H.J. Buschow, Editor. 1999, North Holland: Amsterdam. p. 395-524.
4. W. Dai, B.G. Shen, D.X. Li and Z.X. Gao, *Journal of Magnetism and Magnetic Materials*. **218** (2000): p. 25-30
5. H.R. Kirchmayr, *J. Phys. D: Appl. Phys.* **29** (1996): p. 2763-2778
6. J.A. Barclay and W. Steyert, *Active magnetic regenerator*, in *U.S. Patent*. 1981.
7. V.K. Pecharsky and K.A. Gschneidner, *Physical Review Letters.* **78** (1997): p. 4494-4497

8. W. Choe, V.K. Pecharsky, A.O. Pecharsky, K.A. Gschneidner, V.G. Young and G.J. Miller, *Physical Review Letters*. **84** (2000): p. 4617-4620
9. L. Morellon, J. Blasco, P.A. Algarabel and M.R. Ibarra, *Physical Review B*. **62** (2000): p. 1022-1026
10. A.O. Pecharsky, K.A. Gschneidner, V.K. Pecharsky and C.E. Schindler, *Journal Of Alloys And Compounds*. **338** (2002): p. 126-135
11. Y. Mozharivskyj, A.O. Pecharsky, V.K. Pecharsky and G.J. Miller, *Journal of the American Chemical Society*. **127** (2005): p. 317-324
12. L. Morellon, P.A. Algarabel, M.R. Ibarra, J. Blasco, B. Garcia-Landa, Z. Arnold and F. Albertini, *Physical Review B*. **58** (1998): p. R14721-R14724
13. L. Morellon, Z. Arnold, P.A. Algarabel, C. Magen, M.R. Ibarra and Y. Skorokhod, *Journal of Physics-Condensed Matter*. **16** (2004): p. 1623-1630
14. V.K. Pecharsky, G.D. Samolyuk, V.P. Antropov, A.O. Pecharsky and K.A. Gschneidner, *Journal of Solid State Chemistry*. **171** (2003): p. 57-68
15. L. Morellon, P.A. Algarabel, C. Magen and M.R. Ibarra, *Journal of Magnetism and Magnetic Materials*. **237** (2001): p. 119-123
16. E.M. Levin, V.K. Pecharsky, K.A. Gschneidner and G.J. Miller, *Physical Review B*. **64** (2001): p. 235103
17. H. Tang, V.K. Pecharsky, G.D. Samolyuk, M. Zou, K.A. Gschneidner, V.P. Antropov, D.L. Schlagel and T.A. Lograsso, *Physical Review Letters*. **93** (2004): p. 237203
18. L. Morellon, J. Stankiewicz, B. Garcia-Landa, P.A. Algarabel and M.R. Ibarra, *Applied Physics Letters*. **73** (1998): p. 3462-3464
19. A.O. Pecharsky, K.A. Gschneidner and V.K. Pecharsky, *Journal of Applied Physics*. **93** (2003): p. 4722-4728
20. V.K. Pecharsky and K.A. Gschneidner, *Journal of Magnetism and Magnetic Materials*. **167** (1997): p. L179-L184
21. V. Provenzano, A.J. Shapiro and R.D. Shull, *Nature*. **429** (2004): p. 853-857
22. A. Giguere, M. Foldeaki, B.R. Gopal, R. Chahine, T.K. Bose, A. Frydman and J.A. Barclay, *Physical Review Letters*. **83** (1999): p. 2262-2265
23. K.A. Gschneidner, V.K. Pecharsky, E. Brück, H.G.M. Duijn and E.M. Levin, *Physical Review Letters*. **85** (2000): p. 4190-4190
24. P.I. Kripyakevich, O.S. Zarechnyuk, E.I. Gladyshevsky and O.I. Bodak, *Z. Anorg. Chem*. **358** (1968): p. 90
25. T.T.M. Palstra, J.A. Mydosh, G.J. Nieuwenhuys, A.M. van der Kraan and K.H.J. Buschow, *J. Magn. Magn. Mater.* **36** (1983): p. 290-296
26. F.X. Hu, B.G. Shen, J.R. Sun and X.X. Zhang, *Chinese Physics*. **9** (2000): p. 550-553
27. S. Fujieda, A. Fujita and K. Fukamichi, *Applied Physics Letters*. **81** (2002): p. 1276-1278
28. F.X. Hu, B.G. Shen, J.R. Sun, A.B. Pakhomov, C.Y. Wong, X.X. Zhang, S.Y. Zhang, G.J. Wang and Z.H. Cheng, *Ieee Transactions on Magnetics*. **37** (2001): p. 2328-2330Part 1.

29. X.B. Liu, Z. Altounian and G.H. Tu, *Journal of Physics-Condensed Matter*. **16** (2004): p. 8043-8051
30. X.B. Liu, X.D. Liu, Z. Altounian and G.H. Tu, *Journal Of Alloys And Compounds*. **397** (2005): p. 120-125
31. O. Gutfleisch, A. Yan and K.H. Muller, *Journal Of Applied Physics*. **97** (2005): p. Part 3 10M305
32. F.X. Hu, B.G. Shen, J.R. Sun and Z.H. Cheng, *Physical Review B*. **6401** (2001): p. 012409012409.
33. F.X. Hu, J. Gao, X.L. Qian, M. Ilyn, A.M. Tishin, J.R. Sun and B.G. Shen, *Journal Of Applied Physics*. **97** (2005): p. Part 3 10M303
34. J.R. Proveti, E.C. Passamani, C. Larica, A.M. Gomes, A.Y. Takeuchi and A. Massioli, *Journal Of Physics D-Applied Physics*. **38** (2005): p. 1531-1539
35. J. Shen, Y.X. Li, F. Wang, G.J. Wang and S.Y. Zhang, *Chinese Physics*. **13** (2004): p. 1134-1138
36. A. Fujita, S. Fujieda, Y. Hasegawa and K. Fukamichi, *Physical Review B*. **67** (2003): p. 104416
37. K. Irisawa, A. Fujita, K. Fukamichi, Y. Yamazaki, Y. Iijima and E. Matsubara, *Journal Of Alloys And Compounds*. **316** (2001): p. 70-74
38. S. Fujieda, A. Fujita and K. Fukamichi, *Materials Transactions*. **45** (2004): p. 3228-3231
39. K. Mandal, O. Gutfleisch, A. Yan, A. Handstein and K.H. Muller, *Journal Of Magnetism And Magnetic Materials*. **290** (2005): p. 673-675
40. S.A. Nikitin, I.S. Tereshina, V.N. Verbetsky, A.A. Salamova and E.V. Anosova, *Journal Of Alloys And Compounds*. **367** (2004): p. 266-269
41. F.W. Wang, G.J. Wang, F.X. Hu, A. Kurbakov, B.G. Shen and Z.H. Cheng, *Journal of Physics-Condensed Matter*. **15** (2003): p. 5269-5278
42. L. Pytlik and A. Zieba, *J. Magn. Magn. Mater.* **51** (1985): p. 199-210
43. H. Fjellvag and K. A., *Acta Chem. Scand. A*. **38** (1984): p. 1
44. H. Wada and Y. Tanabe, *Applied Physics Letters*. **79** (2001): p. 3302-3304
45. C. Kuhrt, T. Schittny and K. Barner, *Phys. Stat. Sol. (a)*. **91** (`1985): p. 105-113
46. N. Menyuk, J.A. Kafalas, K. Dwight and J.B. Goodenough, *Physical Review*. **177** (1969): p. 942
47. H. Yamada, K. Terao, K. Kondo and T. Goto, *Journal Of Physics-Condensed Matter*. **14** (2002): p. 11785-11794
48. H. Wada, T. Morikawa, K. Taniguchi, T. Shibata, Y. Yamada and Y. Akishige, *Physica B-Condensed Matter*. **328** (2003): p. 114-116
49. H. Wada, K. Taniguchi and Y. Tanabe, *Materials Transactions*. **43** (2002): p. 73-77
50. H. Wada and T. Asano, *Journal Of Magnetism And Magnetic Materials*. **290** (2005): p. 703-705Part 1 Sp. Iss. SI.
51. T. Morikawa, H. Wada, R. Kogure and S. Hirosawa, *Journal of Magnetism and Magnetic Materials*. **283** (2004): p. 322-328

52. H. Wada, C. Funaba, T. Asano, M. Ilyn and A.M. Tishin, *Sci. Tech. Froid comptes rendus*. **2005-4** (2005): p. 37-46Part 1 Sp. Iss. SI.

53. S. Gama, A.A. Coelho, A. de Campos, A.M.G. Carvalho, F.C.G. Gandra, P.J. von Ranke and N.A. de Oliveira, *Physical Review Letters*. **93** (2004)

54. P.J. Webster, K.R.A. Ziebeck, S.L. Town and M.S. Peak, *Philosophical Magazine B*. **49** (1984): p. 295

55. F.X. Hu, B.G. Shen, J.R. Sun and G.H. Wu, *Phys. Rev*. **B 64** (2001): p. 132412

56. J. Marcos, A. Planes, L. Manosa, F. Casanova, X. Batlle, A. Labarta and B. Martinez, *Physical Review B*. **66** (2002): p. 224413

57. Y.K. Kuo, K.M. Sivakumar, H.C. Chen, J.H. Su and C.S. Lue, *Physical Review B*. **72** (2005): p. 054116

58. X.Z. Zhou, W. Li, H.P. Kunkel, G. Williams and S.H. Zhang, *Journal Of Applied Physics*. **97** (2005): p. Part 3 10M515

59. Y. Long, Z.Y. Zhang, D. Wen, G.H. Wu, R.C. Ye, Y.Q. Chang and F.R. Wan, *Journal Of Applied Physics*. **98** (2005): p. 033515046102.

60. H. Fujii, S. Komura, T. Katega, T. Okamoto, I. Y. and J. Akimitsu, *J. Phys. Soc. Jpn*. **46** ((1979)): p. 1616

61. H. Fujii, T. Hokabe, T. Komigaichi and T. Okamoto, *J. Phys. Soc. Jpn.* **43** ((1977)): p. 41

62. H. Kadomatsu, M. Isoda, K. Tohma, H. Fujii, T. Okamoto and H. Fujiwara, *J. Phys. Soc. Jpn.* **54** (1985): p. 2790

63. P. Jernberg, A. Yousif and L. Hägström, *J. Solid State Chem*. **53** (1984): p. 313

64. O. Beckmann and L. Lundgren, *Compounds of transition elements with nonmetals*, in *Handbook of Magnetic Materials*, K.H.J. Buschow, Editor. 1991, North Holland: Amsterdam. p. 181-287.

65. E. Brück, O. Tegus, X.W. Li, F.R. de Boer and K.H.J. Buschow, *Physica B-Condensed Matter*. **327** (2003): p. 431-437

66. O. Tegus, E. Brück, L. Zhang, Dagula, K.H.J. Buschow and F.R. de Boer, *Physica B*. **319** (2002): p. 174-192

67. O. Tegus, E. Brück, W. Dagula, X.W. Li, L. Zhang, K.H.J. Buschow and F.R. de Boer, *Journal Of Applied Physics*. **93** (2003): p. 7655-7657Part 3.

68. O. Tegus, B. Fuquan, W. Dagula, L. Zhang, E. Brück, P.Z. Si, F.R. de Boer and K.H.J. Buschow, *Journal Of Alloys And Compounds*. **396** (2005): p. 6-9

69. L. Zhang, O. Moze, K. Prokes, O. Tegus and E. Brück, *Journal Of Magnetism And Magnetic Materials*. **290** (2005): p. 679-681Part 1 Sp. Iss. SI.

STUDIA UNIVERSITATIS BABEŞ-BOLYAI, PHYSICA, LII, 1, 2007

MULTIFERROIC MATERIALS

KATHRIN DÖRR*

Table of Contents

ABSTRACT. Primary ferroic properties found in solids include ferromagnetism, ferroelectricity, ferroelasticity and ferrotoroidicity. Apart from the last, these properties are extremely important for our daily life: they are exploited in transformers, magnetic data storage, in position sensors, actuators, micromechanical applications and so on. In the sixties of the last century, research started to explore the requirements for a joined appearance of more than one ferroic property [1, 2 and reviews 3-7] and termed such materials „multiferroic“.

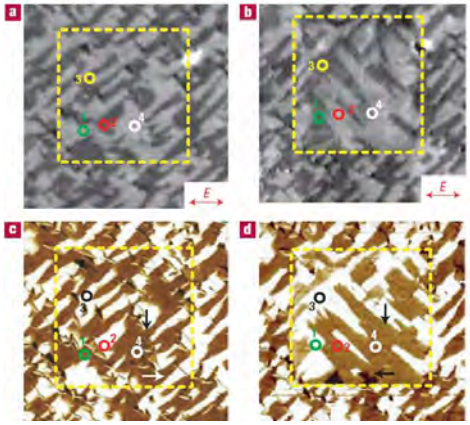

Fig. 1. Coupled switching of antiferromagnetic (upper panel) and ferroelectric (lower panel) domains in $BiFeO_3$ at ambient temperature. (T. Zhao et al., Nat. Materials 2006)

* IFW Dresden, Postfach 270116, 01171 Dresden, k.doerr@ifw-dresden.de

Multiferroics with coupled ferroic properties, sufficiently large polarization and appropriate working temperatures would widely enhance the choices to sense and control. One example is the manipulation of the magnetization by an electric field utilizing the magnetoelectric effect. In this lecture, the focus is on magnetic and ferroelectric multiferroics. Early investigated materials like Cr2O3 showed an extremely small effect. Modern methods of preparation (thin film and nanostructuring techniques), investigation (scattering techniques, non-linear optics and further) and theoretical modelling have opened ways toward discovery and design of strongly magnetoelectric materials. This has triggered a revival of research activities [3-7]. Current efforts are devoted to areas including the following: (i) discovery of new single-phase compounds (spin spirals and charge ordering as source of electric polarization), (ii) experimental detection of the coupling phenomena (e. g., of the different ferroic domains) and (iii) design of nanocomposites of magnetic and ferroelectric components (mostly in thin film structures [4 6, 8-10]). Whereas room-temperature single-phase multiferroics are very few (BiFeO3), composites promise a potential for application and substantial magnetoelectric responses have been reported [5,6,8]. However, there is a way to go, since thin film fabriaction has started few years ago and very little is known about dynamic properties of multiferroics.

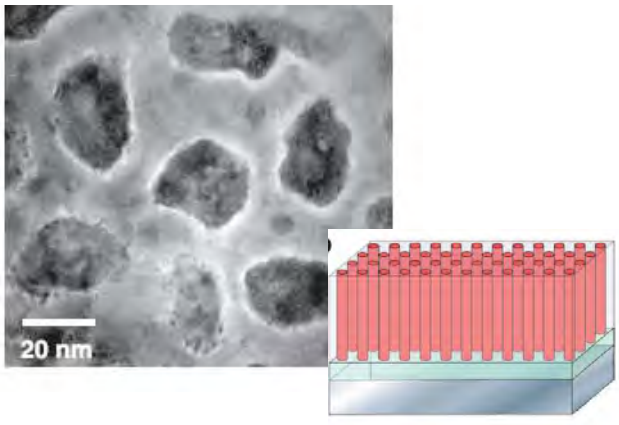

Fig. 2. Self-organized growth of epitaxial $BaTiO_3$- $CoFe_2O_4$ nanocolumnar structures in films grown by pulsed laser deposition (H. Zheng et al., Science 303, 661 (2004))

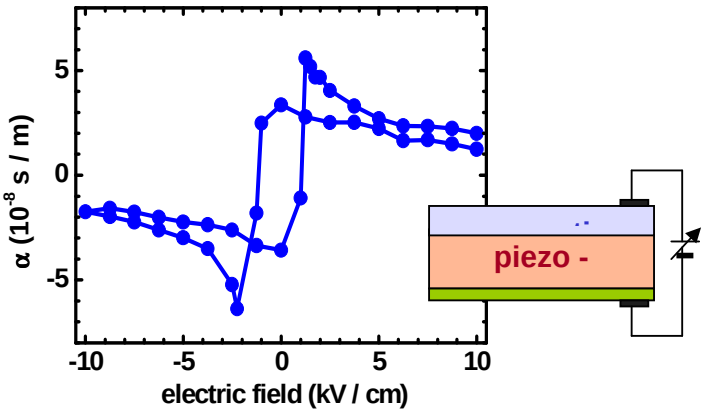

Fig. 3. Magnetoelectric coupling coefficient a = m0 dM/dE at 300 K with the magnetization M controlled by applied electric field E in an epitaxially grown $La_{0.7}Sr_{0.3}MnO_3$ film on PMN-PT(001) (Ref.8)

REFERENCES

1. P. Curie, J. de Physique (3rd series) 3, 393 (1894) First consideration of an intrinsic correlation of magnetic and electric properties in a solid
2. I. E. Dzyaloshinskii, Sov. Phys. – JETP 10, 628 (1959); D. N. Astrov, Sov. Phys. – JETP 11, 708 (1960) Prediction and first observation of the magnetoelectric effect in Cr2O3
3. M. Fiebig: Revival of the magnetoelectric effect. J. Phys. D 38, R123 (2005) (review)
4. W. Prellier, M. P. Singh, P. Murugavel: The single-phase multiferroic oxides – from bulk to thin film. J. Phys. Cond. Matter 17, R803 (2005) (review)
5. N. A. Spaldin, M. Fiebig: The renaissance of magnetoelectric multiferroics, Science 309, 391 (2005).
6. W. Eerenstein, N. D. Mathur, J. Scott: Multiferroic and magnetoelectric materials, Nature 442, 759 (2006).
7. D. I. Khomskii: Multiferroics – different ways to combine magnetism and ferroelectricity. J. Magn. Magn. Mater. 306 (2006)
8. C. Thiele, K. Dörr, O. Bilani, J. Rödel, L. Schultz: Influence of strain on the magnetization and magnetoelectric effect in La0.7A0.3MnO3/PMN-PT(001) Phys. Rev. B 75, 054408 (2007)
9. C. Thiele, K. Dörr, E. Beyreuther, L. Schultz, W.-M. Lin: Piezoelectrically induced resistance modulations in La0.7Sr0.3MnO3 / Pb(Zr,Ti)O3 field effect devices. Appl. Phys. Lett. 87, 162512 (2005)
10. M. Gajek, M. Bibes, S. Fusil, K. Bouzehouane, J. Fontcuberta, A. Barthelemy, A. Fert: Tunnel junctions with multiferroic barriers. Nature Materials (2007)

STUDIA UNIVERSITATIS BABEŞ-BOLYAI, PHYSICA, LII, 1, 2007

FERROFLUIDS
SYNTHESIS, PROPERTIES AND APPLICATIONS

LADISLAU VÉKÁS*

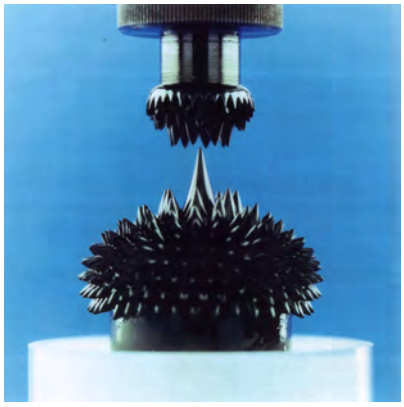

ABSTRACT. Ferrofluids (also called magnetic fluids or magnetic nanofluids) are a special category of nanomaterials which exhibit simultaneously liquid and superparamagnetic properties. The possibility of magnetic control over their properties and flow triggered both basic and application orientated researches. The talk will summarize results on ferrofluid synthesis, properties and ferrohydrodynamics, as well as on engineering and biomedical applications.

1. INTRODUCTION

Ferrofluids (known also as magnetic fluids) are a special category of smart nanomaterials, in particular magnetically controllable nanofluids [1]. These types of nanofluids are colloids of magnetic nanoparticles, such as Fe_3O_4, γ-Fe_2O_3, $CoFe_2O_4$, Co, Fe or Fe-C, stably dispersed in a carrier liquid [2]. Consequently, these nanomaterials manifest simultaneously *fluid* and *magnetic* properties. Macroscopically, the introduction of magnetic forces into the fundamental hydrodynamic equations for the quasihomogeneous magnetizable liquid medium

* Laboratory of Magnetic Fluids, Center for Fundamental and Advanced Technical Research, Romanian Academy-Timisoara Division, Timisoara, Romania; National Center for Engineering of Systems with Complex Fluids, University Politehnica Timisoara, Timisoara, Romania

gives rise to the magnetohydrodynamics of magnetic nanofluids (ferrofluids), known also as *ferrohydrodynamics* and opens up an entire field of new phenomena [3] and promising applications [4]. From a microscopic point of view, long-range, attractive van der Waals and magnetic forces are ubiquitous and therefore must be balanced by Coulombic, steric or other interactions to control the colloidal stability of dispersed nanoparticle system, even in intense and strongly non-uniform magnetic field, specific to most of the applications [5, 6].

Many of the envisaged applications, e.g., rotating seals or bearings, require magnetic fluids with high magnetization and at the same time, with long-term colloidal stability. These requirements are difficult to fulfill simultaneously and implies severe conditions on the stabilization procedures applied during the synthesis of magnetic nanofluids.

The composition, structure and properties of various types of ferrofluids will be presented, refering also to technological and biomedical applications envisaged for these nanofluids [2, 5].

2. SYNTHESIS OF FERROFLUIDS

The synthesis of ferrofluids has two main steps: (a) the preparation of nano-sized magnetic particles (2-15 nm) and (b) the subsequent dispersion/stabilization of the nanoparticles in various non-polar and polar carrier liquids. In what concerns the ferrite nanoparticles, the most efficient route is the chemical co-precipitation process [2]. Depending on the carrier properties and applications envisaged, different procedures of ferrofluid synthesis were developed, which will be shortly reviewed [5]. The stabilization mechanisms of magnetic nanoparticles in various kind of carrier liquids, which should prevent irreversible particle agglomerate formation even in intense and strongly non-uniform magnetic field, will be discussed.

3. CHARACTERIZATION

3.1. Structural investigations and colloidal stability In the case of sterically stabilized nanoparticles in various carrier liquids, the type and quality of surfactants used, as well as the temperature of the medium will determine the efficiency of particle surface covering and, consequently, the balance between attractive and repulsive interactions between particles. The attractive interactions, when preponderant, may lead to various types of agglomerates, usually in the shape of linear chains quasi-parallel to the applied magnetic field or drop-like aggregates [7]. The agglomeration processes are not desired in the case of magnetic fluids used in most of the applications; therefore the characterization methods are mainly focused on these processes and on their consequences in the macroscopic behaviour of the fluids.

One of the most efficient methods of nanostructural investigation is based on small angle neutron scattering (SANS) [8]. This method is applied to reveal structural features at the scale of 1-100 nm and it will be presented in detail, beside results of TEM, DLS and magnetogranulometric analyses.

3.2. Magnetic properties Magnetization curves can be extensively used for the study of both particle interactions and agglomerate formation, processes which strongly influence the rheological and magnetoheological behaviour of magnetic fluids. Saturation magnetization *(M_s)*, initial susceptivity *(χ_i)*, full magnetization curves (*M=M(H)* or *$M/M_s(H)$*, (*H*-intensity of applied magnetic field) and magneto-granulometric analysis (mean magnetic diameter $<D_m>$ and standard deviation σ), at various values of the volumic concentration of magnetic nanoparticles, give an insight on microstructural characteristics of various samples to be compared [9,10]. The dimension of the clusters can give a first hint about both the degree of particle dispersion and the strength of the interparticle interactions. Usually, it can be analyzed via optical methods (e.g. DLS). In spite of the clustering process, the net attractive inter-particle interactions (considered as dipole-dipole type) should be quite weak, due to the steric repulsion induced by the double coating layers. The attractive interactions are considered to induce only perturbations of the main anisotropy energy of the particles. *Temperature dependent Mössbauer spectroscopy* [11] is providing information on particle phase composition, local structure and symmetry, local magnetic interactions inside the particle and Néel-type relaxation phenomena.

3.3 Rheological and magnetorheological properties [12] depend especially on composition, particle volume fraction and degree of colloidal stability of ferrofluids, as well as on the intensity of applied magnetic field. Methodology of investigations on flow properties and main results will be reviewed, with strong emphasis on specially tailored ferrofluids for applications.

4. FERROHYDRODYNAMICS

Equations of ferrohydrodynamics, developed initially by Neuringer and Rosensweig [3], will be synthesized. First, the equations resulting for a quasihomogeneous ferrofluid in the quasistatic approximation will be presented, which correspond to a diluted ferrofluid, with pointlike magnetic dipoles and ideal Langevin behavior of magnetization in a slowly varying field. Next, the model of ferrofluids with internal rotations (Shliomis [13], Rosensweig [14]) taking into account the relaxation of magnetization by Néel or Brown type mechanism, will be shortly outlined.

5. TECHNOLOGICAL and BIOMEDICAL APPLICATIONS [1-6, 15-17]

Synthesis of new type of hybrid nanostructured materials: polymeric nanocomposites, magnetically controlled gels and emulsions; Dynamic sealing with magnetic fluids; Magnetic fluid bearings; Moving coil speakers with magnetic fluid damping and

cooling; Inertia dampers with magnetic fluids; Sensors and actuators; Magnetohydrostatic separation; Surface finshing techniques; Non-destructive testing; Domain pattern investigations; Multifunctional magnetic particles, magnetic nanobeads; Magnetic cell separation; Magnetic contrast agents, MRI; Hyperthermia of tumors; Magnetic drug delivery.

REFERENCES

1. S. ODENBACH (Editor), *Ferrofluids: Magnetically controllable fluids and their applications*, Lecture Notes in Physics, Springer-Verlag, 253 pags (2002).
2. S. W. CHARLES, The preparation of magnetic fluids, in: S. ODENBACH (Editor), *Ferrofluids: Magnetically controllable fluids and their applications*, Lecture Notes in Physics, Springer-Verlag, pp.3-18, 2002. See also: S. W. CHARLES, Preparation and magnetic properties of magnetic fluids, Rom. Repts. Phys., vol.47 (3-5), pp.249-264, 1995.
3. R.E. ROSENSWEIG, *Ferrohydrodynamics*, Cambridge Univ. Press, pp.344, 1985; see also J.L. Neuringer, R.E. Rosensweig, Phys. Fluids 7(1964)1927
4. B. BERKOVSKY, V. BASHTOVOI (Eds.), *Magnetic fluids and applications handbook*, Begell House, New York, pp.831, 1996.
5. L. VEKAS, D. BICA, M. V. AVDEEV, Magnetic nanoparticles and concentrated magnetic nanofluids: synthesis, properties and some applications, China Particuology, 2007 (to appear); see also: I. ANTON, I. DE SABATA, L. VEKAS, Application orientated researches on magnetic fluids, J. Magn. Magn. Mater., vol.85, pp.219-226, 1990.
6. K. RAJ, Magnetic fluids and devices: a commercial survey, in: B. BERKOVSKY, V. BASHTOVOI (Eds.), *Magnetic fluids and applications handbook*, Begell House, New York, pp.657-751 (1996)
7. V. CABUIL, J.C. BACRI, R. PERZYNSKY, YU. RAIKHER, Colloidal stability of magnetic fluids, in: B. BERKOVSKY, V. BASHTOVOI (Eds.), *Magnetic fluids and applications handbook*, Begell House, New York, pp.33-56 (1996).
8. M.V. Avdeev, V.L. Aksenov, M. Balasoiu, V.M. Garamus, A. Schreyer, Gy. Torok, L. Rosta, D. Bica,. L. Vekas, Comparative analysis of the structure of sterically stabilized ferrofluids on polar carriers by small-angle neutron scattering, J. Coll.Interface Sci., 295(2006)100-107; see also: M.V. Avdeev, Contrast variation in small-angle scattering experiments on polydisperse and superparamagnetic systems: basic function approach, J. Appl.Cryst., 40(2007)56-70.
9. M. RASA, D. BICA, A.P. PHILIPSE, L. VEKAS, Dilution series approach for investigation of microstructural properties and particle interactions in high-quality magnetic fluids, Eur. Phys. J. E (2002), vol.7, pp.209-220.

10. A. O. Ivanov, O. B. Kuznetsova, Interparticle correlations and magnetic properties of concentrated ferrocolloids, Collod J., vol.63, pp.60-67, 2001.
11. V. Kuncser, G. Schinteie, B. Sahoo, W. Keune, D. Bica, L. Vékás, G. Filoti, Magnetic interactions in water-based ferrofluids studied by Mössbauer spectroscopy. J. Phys.: Cond. Matter. (2007)19(1)016205-016221
12. S. Odenbach, Magnetoviscous effects in ferrofluids, Springer LNP m71 (Berlin, New York, 2002)
13. M.I. Shliomis, Ferrohydrodynamics: Retrospective and Issues, in: S. ODENBACH (Editor), *Ferrofluids: Magnetically controllable fluids and their applications*, Lecture Notes in Physics, Springer-Verlag, pp.85-110, 2002.
14. R. E. Rosensweig, Basic Equations for Magnetic Fluids with Internal Rotations, in: S. ODENBACH (Editor), *Ferrofluids: Magnetically controllable fluids and their applications*, Lecture Notes in Physics, Springer-Verlag, pp.61-84, 2002.
15. Turcu R., Pana O., Nan A. and Giurgiu L. M. Polymeric Nanostructures and Their Applications vol 1, ed. H.S. Nalwa (American Scientific Publishers) pp 337-99(2007); see also Eunate Goiti, Rebeca Hernández, , Ruy Sanz, Daniel López, Manuel Vázquez, Carmen Mijangos, Rodica Turcu, Alexandrina Nan, Doina Bica, Ladislau Vekas, Novel nanostructured magneto-polymer composites, Journal of Nanostructured Polymers and Nanocomposites 2(2006)5-12 .
16. Z. Varga, J. Feher, G. Filipcsei, M. Zrinyi, Smart nanocomposite polymer gels, Macromolecular Symposia, 200 (2003)93-100.] Z. Varga, G. Filipcsei, M. Zrinyi, Smart composites with controlled anisotropy, Polymer, 46(2005)7779-7787.
17. Neuberger, T., Schopf, B., Hofmann, H., Hofmann, M. & Rechenberg, B. Superparamagnetic nanoparticles for biomedical applications: Possibilities and limitations of a new drug delivery system. *J. Magn. Magn. Mater.*, 293(2005) 483-496.
18. Pankhurst, Q.A., Connolly, J., Jones, S.K. & Dobson J. , Applications of magnetic nanoparticles in biomedicine. *J. Phys. D: Appl.Phys.*, 36(2003) R167-R181.

STUDIA UNIVERSITATIS BABEŞ-BOLYAI, PHYSICA, LII, 1, 2007

(I) MAGNETOSTRICTIVE EFFECT
(II) MAGNETIC SHAPE MEMORY MATERIALS

KATHRIN DÖRR, SEBASTIAN FÄHLER*

Table of Contents

Magnetostriction is a property of magnetic materials that causes them to change their shape when subjected to a magnetic field. It was first observed in 1842 by J. Joule in a Ni sample. It is a manifestation of the spin-orbit coupling.
Magnetostrictive materials are used to convert magnetic into kinetic energy and vice versa, i. e. they are utilized in actuators and sensors. Key parameters for application are the achievable strain and stress, working field and temperature. Maximum ordinary magnetostriction reaches values of 0.2 % in a field of H = 2 kOe for Terfenol-D (TbxDy1-xFe2). However, strains can be in the range of several percent if the magnetic field drives a reorientation of the crystal structure (by moving twin boundaries like in a martensite) or even induces a different phase. Both mechanisms are found in magnetic shape memory alloys which show record strains up to 10 %.
This lecture introduces the fundamental mechanisms of magnetostriction and the resulting requirements for materials. Some of the currently studied magnetic shape memory alloys are discussed.

* IFW Dresden, Postfach 270116, 01171 Dresden, k.doerr@ifw-dresden.de, s.faehler@ifw-dresden.de

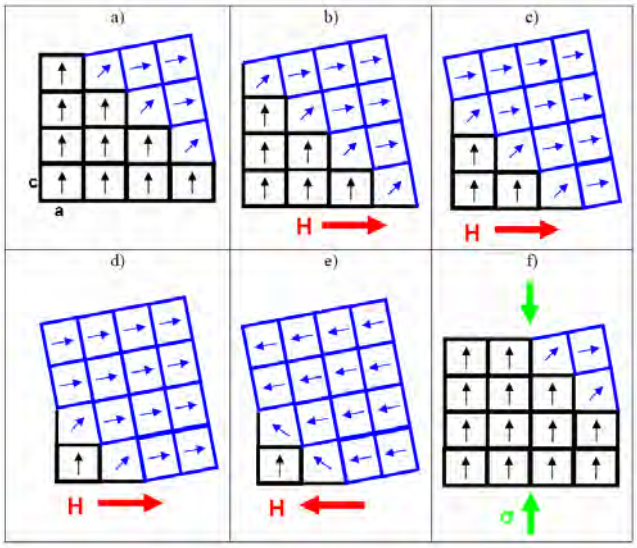

Fig. 1. a) to d) Magnetically induced structure reorientation in a magnetic shape memory alloy. Field-induced movement of a twin boundary causes strains up to 10 %. e) The field reversal is strain-free. f) Recovery of initial state by compressive stress.

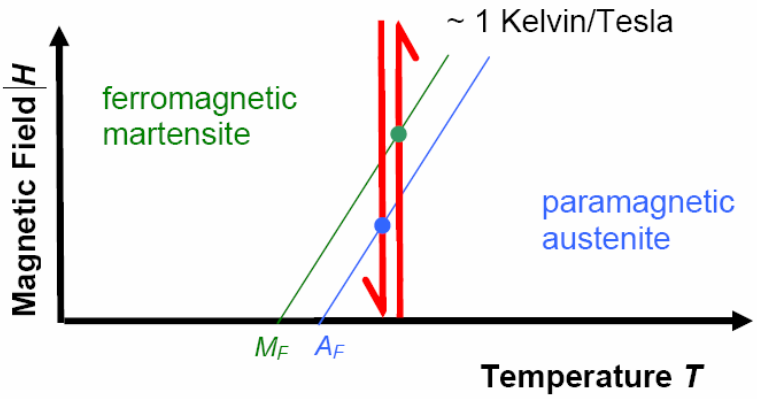

Fig. 2. Field-induced transition between a ferromagnetic martensitic and a paramagnetic austenitic phase during an actuation cycle of MIM (magnetically induced martensite) type. MF and AF mark the martensitic and austenitic finish temperature, respectively.

REFERENCES

1. M. Marioni, R. O'Handley, S. Allen, Appl. Phys. Lett. 83, 3966 (2003)
2. O. Heczko, L. Straka, J. Appl. Phys. 94, 7139 (2003)
3. M. Wuttig, L. H. Liu, K. Tsuchiya, R. D. James, J. Appl. Phys. 87, 4707 (2000)
4. P. J. Webster, K. R. A. Ziebeck, S. L. Town, M. S. Peak, Phil. Mag. B 49, 295 (1984)
5. K. Ullakko, J. K. Huang, C. Kantner, R. C. O´Handley, V. V. Kokorin, Appl. Phys. Lett. 69, 1966 (1996)
6. A. Sozinov, A. A. Likhachev, N. Lanska, K. Ullakko, Appl. Phys. Lett. 80, 1746 (2002)
7. A. N. Lavrov, S. Komiya, Y. Ando, Nature 418 (2002) 385
8. R. D. James, M. Wuttig, Phil. Mag. A 77 1273 (1998)
9. S. Raasch, M. Doerr, A. Kreyssig, M. Loewenhaupt, M. Rotter, J.-U. Hoffmann, Phys. Rev. B 73 064402 (2006)

STUDIA UNIVERSITATIS BABEŞ-BOLYAI, PHYSICA, LII, 1, 2007

MAGNETO-OPTICAL MICROSCOPY AND ITS APPLICATION

RUDOLF SCHÄFER*

The magnetic microstucture, i.e. the arrangement of domains and domain walls, forms the mesoscopic link between basic physical properties of a magnetic material and its macroscopic properties. Hysteresis phenomena, energy loss in inductive devises, noise in sensors, or the magnetoresistive properties of modern spintronic devices are decisively determined by the peculiarities of the underlying magnetic microstructure, especially by irreversibilities in the magnetization process. The development and optimization of magnetic materials therefore requires a solid knowledge of the underlying domains and their reaction to magnetic fields. In most cases, such knowledge can only be gleaned by direct imaging.

Although there has been considerable progress in magnetic imaging in recent years, culminating in the development of a variety of nanoscale imaging techniques, several technical assets inherent to the classical Kerr technique make it arguably the most versatile and flexible imaging technique. Kerr microscopy exploits the magneto-optical Kerr effect, i.e. the magnetization-dependent rotation of plane-polarized light upon reflection from a non-transparent magnetic sample (Fig. 1). By means of an analyser in an optical reflection polarization microscope this rotation is converted into a (in general weak) domain contrast that can be enhanced by digital image processing. When used in conjunction with an image processor, Kerr microscopy can extract domain contrast from the surface of virtually any ferro- or ferrimagnetic sample. Often no specific surface treatment is required and even some coatings may be allowed. The basic components of a Kerr-setup are shown in Fig. 2.

Magnetic fields of arbitrary strength and direction can be applied to the sample, making it possible to observe magnetization processes and to simultaneously measure the localized magnetization loops, governing those processes (Fig. 3). Magnetization dynamics can be studied at arbitrary frequencies, spanning the entire range between slow processes (as fast as the eye can follow), to excitations beyond the Giga-Hertz regime by employing time-resolved, stroboscopic imaging methods – see Figs. 4 and 5. An example of such a high-speed experiment is presented in Fig. 6.

Samples may be heated and cooled in optical heating stages and cryostats, respectively, so that magnetic phase transitions or other thermal effects on the magnetic microstructure can be investigated.

* IFW Dresden, Inst. f. Metallic Materials, Helmholtzstr. 20 , D-01069 Dresden, r.schaefer@ifw-dresden.de

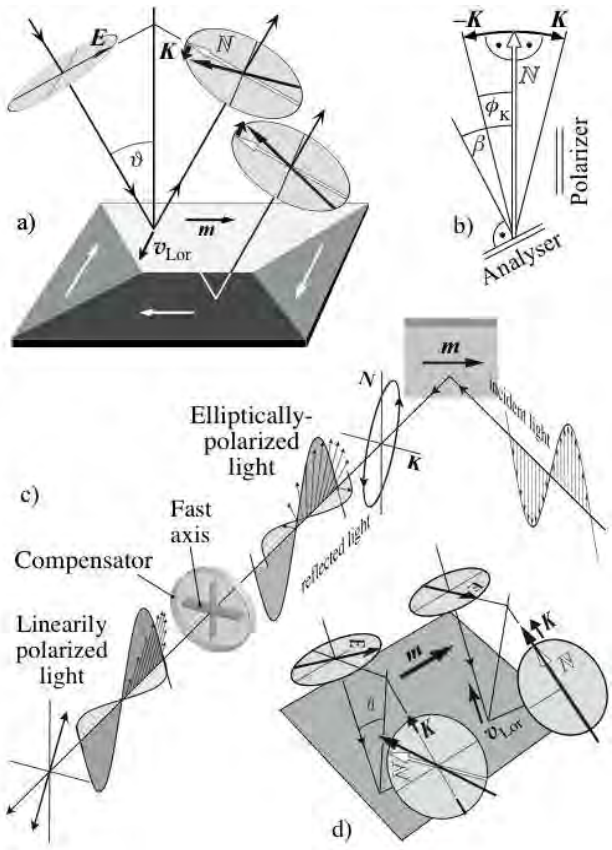

Fig. 1 (a) Illustration of the elementary magneto-optical interaction for the longitudinal Kerr effect. The sample with in-plane magnetization is illuminated using light that is polarized parallel to the plane of incidence. The electric field vector ***E*** of the incident light, together with the magnetization vector ***m***, generates a Lorentz movement of the electrons ("right-hand rule").

If the resulting Lorentz speed v_{Lor} is then projected onto the plane perpendicular to the direction of propagation of the reflected light, the magneto-optical amplitude ***K*** is obtained (a similar ***K***-component would also be generated if the light would be polarized perpendicular to the plane of incidence). The interference of the normally reflected component ***N*** and the Kerr component ***K*** results in magnetization-dependent light rotation by a small angle Φ_K, which, by using an analyser, leads to the domain contrast (b). The analyser should actually be set at the angle $\beta > \Phi_K$ to optimize the domain visibility. A compensator (c) converts elliptical light into a linear wave by shifting the two constituent, orthogonal wave components. The symmetry of the transverse Kerr effect is explained in (d). Only light of parallel polarization yields an effect, so that a Kerr rotation is only possible at 45° polarization

Mechanic sample deformation during domain observation is easily possible in a Kerr microscope, which makes the study of stress effects on domains possible. For low-anisotropy materials, the magnetization vector field on the sample surface can be quantitatively evaluated (Fig. 7). The information depth of Kerr microscopy is in the ten-nanometer regime for metallic materials, allowing the depth selective observation of magnetization distributions in layered sample systems (Fig. 8) as they are currently developed and investigated for spintronic applications. Such multilayer structures can also very favorably be investigated by applying the depth sensitivity of the magneto-optical Voigt- and Gradient effect two other effects that become visible in an optical polarization microscope. The difference between the effects in comparison with the (most commonly used) Kerr effect is demonstrated in Fig. 9.

Since the magnification is so easily varied by the mere changing of a microscope objective, the user can quickly go from overview observations in the centimeter regime, to detailed studies of samples with micrometer size. The lateral resolution of optical microscopy with visible light is limited to about 300 nm by the Raleigh criterion. This can be a drawback for the study of sub-micrometer patterned structures or for certain micromagnetic objects like vortices or stripe domains in very thin films. But for the imaging of most features of magnetic microstructure the resolution is sufficient (Fig. 10). In bulk samples only the magnetization of the surface region can be seen, but this limitation applies to most other imaging techniques as well. Nevertheless, in many cases the volume domains can indirectly be seen or at least guest by surface observations in applied magnetic fields.

There are rare cases of samples that do not provide sufficient Kerr contrast. An example is the NiMnGa magnetic shape memory alloy. Here polarization optics just reveals the crystalline microstructure. Domains can indirectly be imaged by applying indicator films on top of the surface (Fig. 11). Stray fields, emerging from the domains at the sample surface, induce a polar magnetization component in the active layer of the detector which is recorded by the polar Faraday effect.

Since the earliest applications of Kerr microscopy in 1951, continuous methodical developments have greatly enhanced the capabilities of the traditional Kerr technique. In this presentation we shall review the widespread capabilities of contemporary magneto-optical microscopy, as well as the physical and technological fundamentals that underlie the method. Numerous images on a great variety of novel magnetic materials will be shown to demonstrate the advantages and special features of the technique. Comprehensive reviews on domain imaging with emphasis on magneto-optical microscopy are given in [1, 2] where also an extended bibliography can be found.

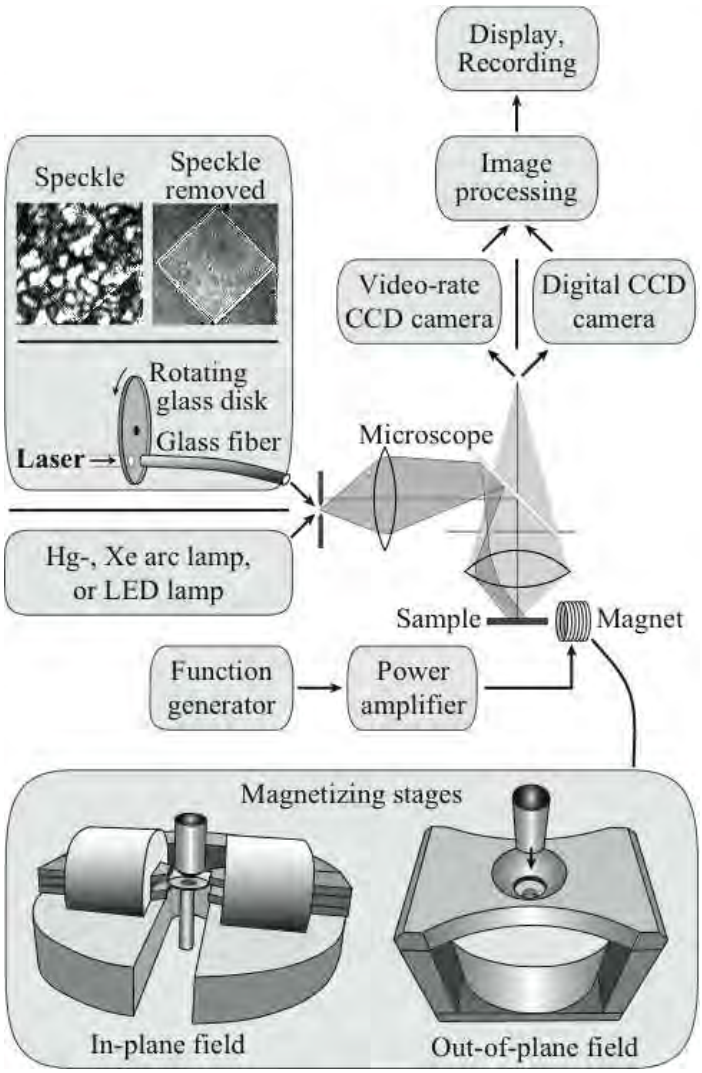

Fig. 2. Experimental setup for wide-field Kerr microscopy. Options are shown for illumination, video processing and magnetizing stages. Also shown is the presence and suppression of interference patterns by laser illumination with and without rotating glass disk, respectively, on a 28 by 28 μm^2 Permalloy thin film element

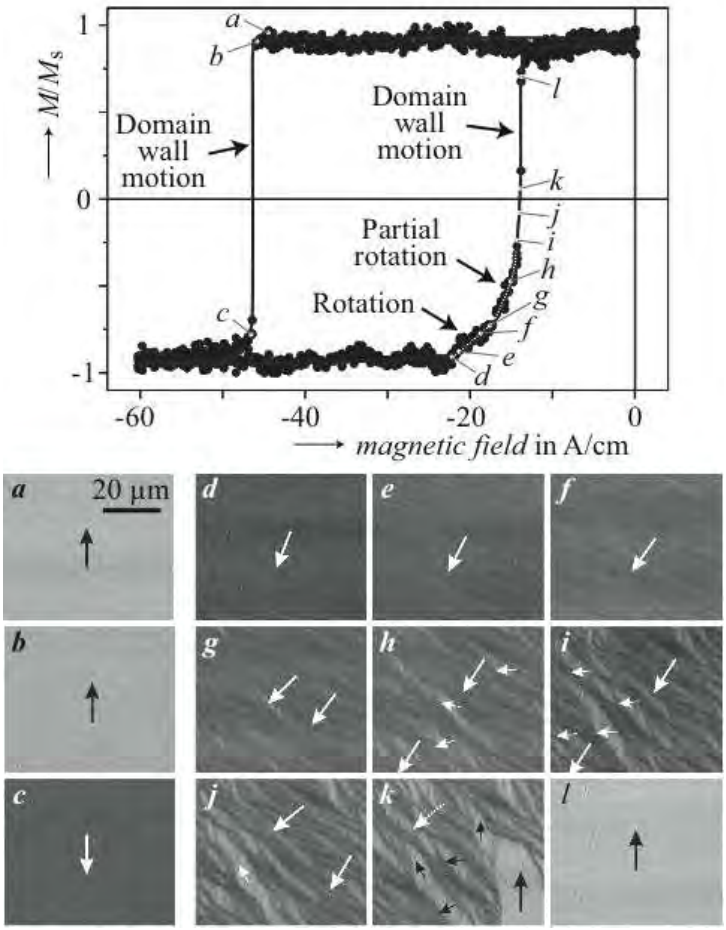

Fig. 3. Magneto-optical hysteresis curve, directly measured in a wide-field Kerr microscope, together with domain images on a CoFe (20 nm)/IrMn (10 nm) bilayer film. Shown are the domains in the ferromagnetic CoFe film, which is exchange coupled to the antiferromagnetic IrMn film that is responsible for the loop shift (exchange bias effect). The steep forward branch of the magnetization curve is caused by domain wall motion (a – c), while inhomogeneous rotational processes (d – k) are responsible for the rounded part of the recoil branch. The wall motion along the forward branch is so fast that it cannot be recorded by static images. The magnetization M is normalized to the saturation magnetization M_s in the plot [courtesy *J. McCord*]

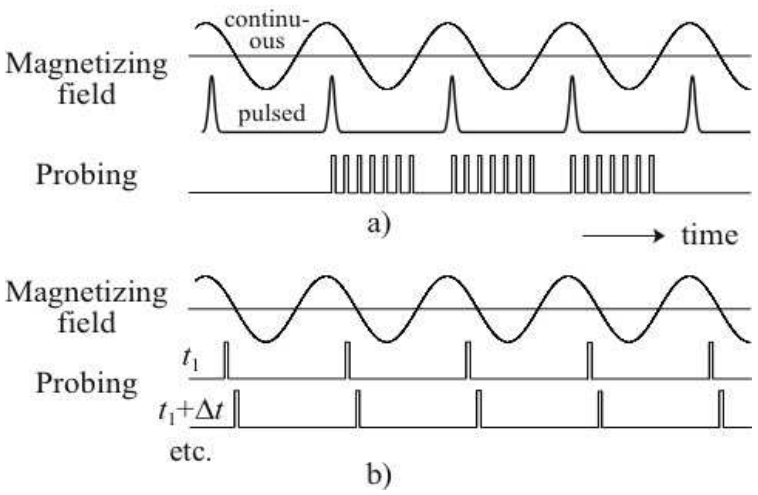

Fig. 4. Principle of time resolved imaging, (a) for an ideal single-shot experiment, and (b) in the stroboscopic mode. The sample is excited either by alternating magnetic fields or a by train of field pulses

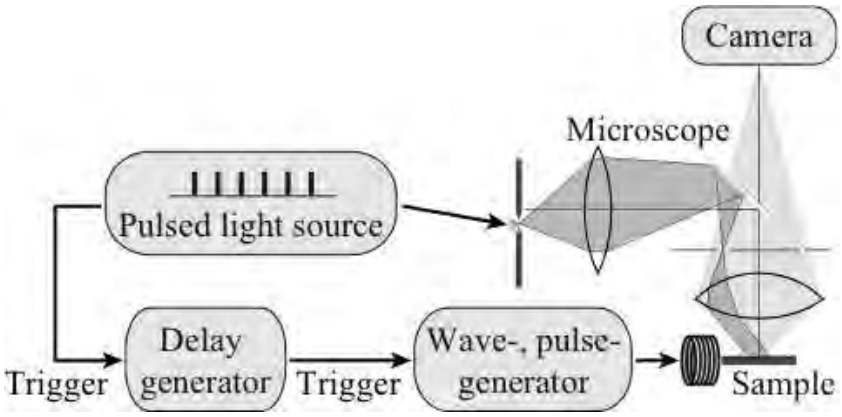

Fig. 5. Block diagram for light-based stroboscopic wide-field microscopy. A pulsed light source is employed for time-resolution

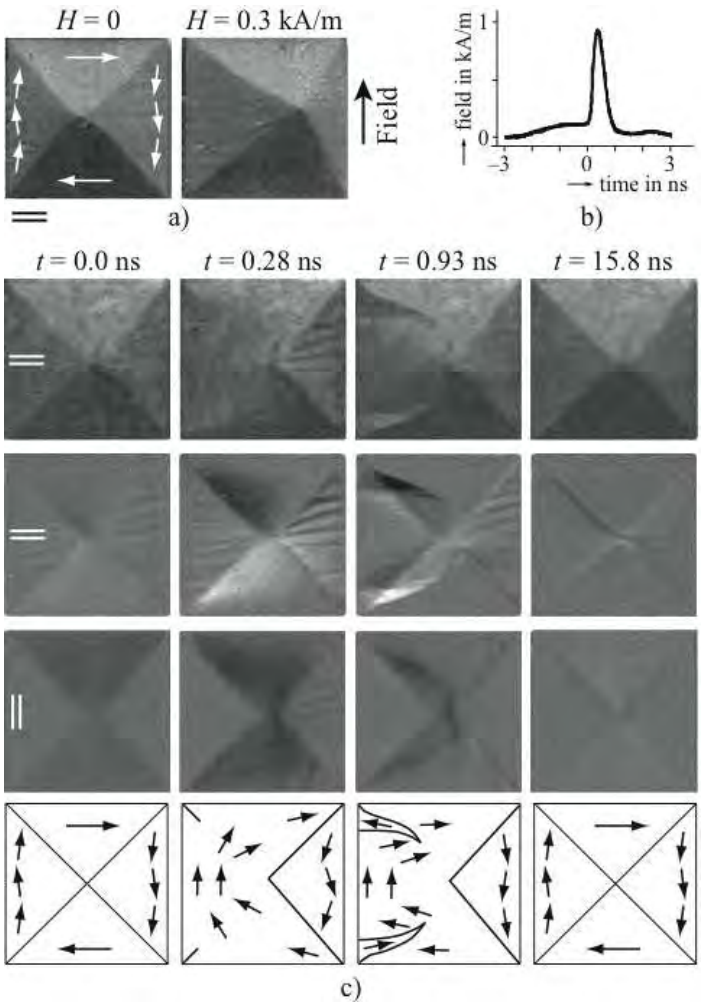

Fig. 6. Excitation of a Landau ground state in a permalloy thin film element (edge length 40 µm, thickness 50 nm) in magnetic fields parallel to the edge. (a) Quasistatic process. The dynamic process (c), excited by a sharp field pulse (b), is completely different. Shown are difference images: In the upper row of (c) an image of the saturated state was subtracted, while images of the Landau ground state were subtracted in the middle and lower row at different Kerr sensitivity directions as indicated, highlighting changes of the magnetization. Indicated are the time delays where the images have been captured in a stroboscopic way. The accumulation of some 10^6 single pictures, each of them obtained with a laser pulse of about 20 ps length, was necessary to obtain an image of sufficient contrast. [Together with *A. Neudert* and *J. McCord*]

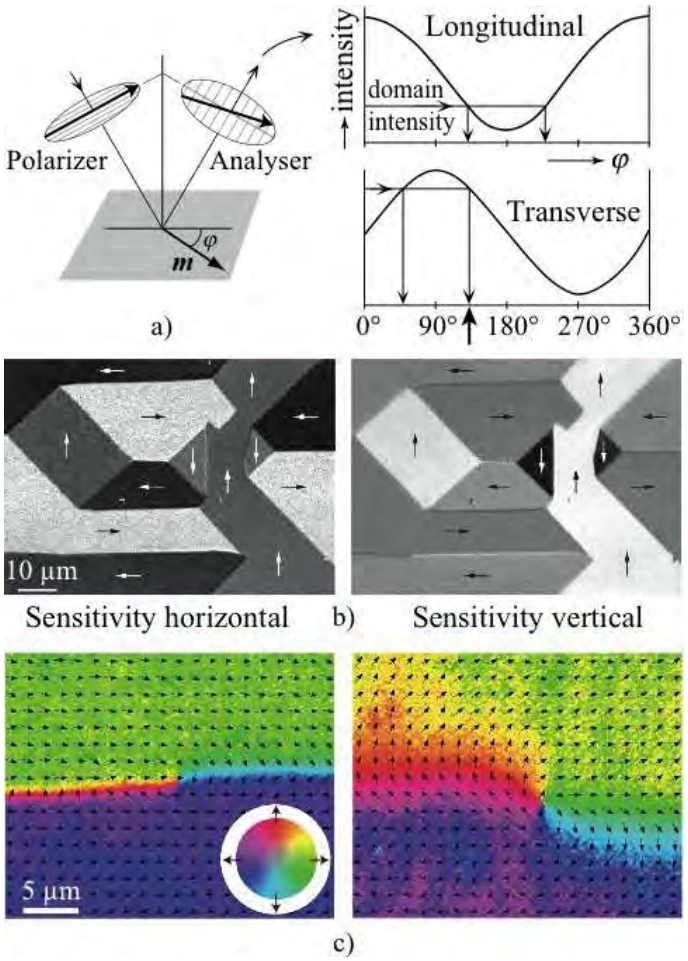

Fig. 7. Principle and application of quantitative Kerr-microscopy. (a) Calibration functions of the Kerr intensity at longitudinal and transverse sensitivity as a function of magnetization direction (schematically). The intensities of an unknown domain, measured under the same conditions, are compared with the calibration functions as indicated by arrows. (b) Domain pattern on iron-silicon [100] sheet, imaged under two complementary Kerr-sensitivities. (c) Quantitative images on a Co-rich amorphous ribbon. The domain wall width of the as-quenched state (left) is strongly enlarged (right) if residual anisotropies are reduced by annealing in a rotating magnetic field. A vector plot and color code can be used for presentation

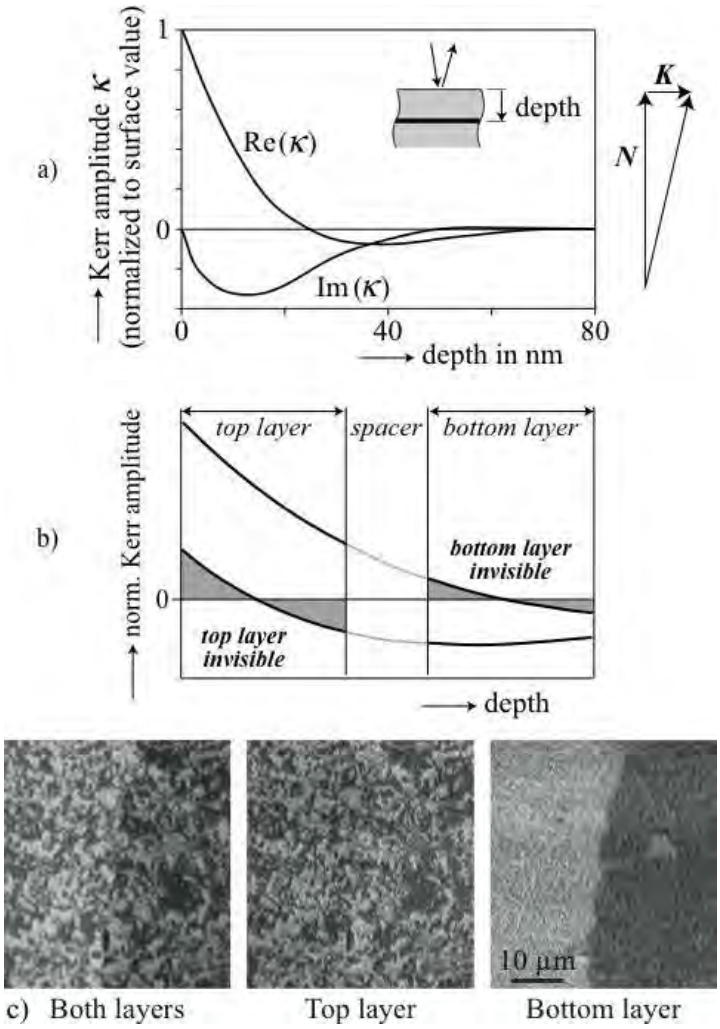

Fig. 8. (a) Depth-sensitivity of the normalized Kerr amplitude κ in iron. The relative phase of ***K*** and ***N*** was selected so that ***N*** is allowed to interfere with the ***K*** generated right at the surface. Proper phase selection (b – schematically) allows layer-selective Kerr imaging on thin-film sandwiches as demonstrated in (c) for a sputtered Co/Cu/$Ni_{81}Fe_{19}$ (5 nm/ 5 nm/ 50 nm) trilayer. [imaging courtesy *J. McCord*, IFW Dresden]

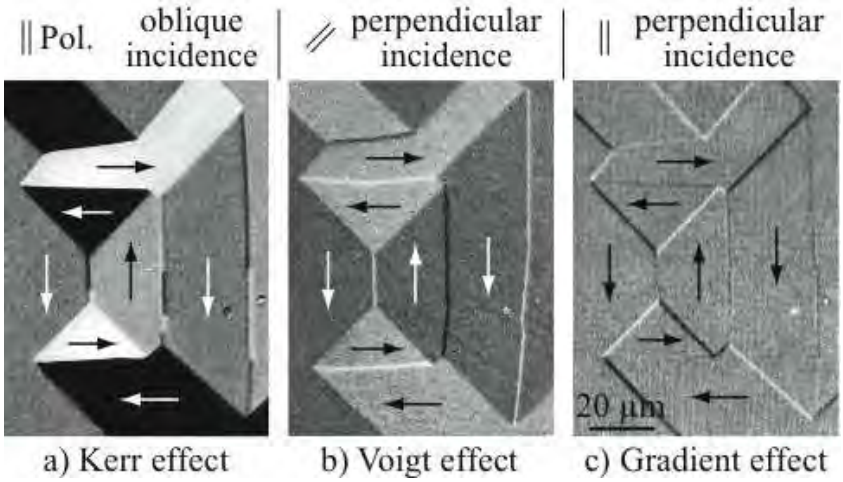

Fig. 9. Domains on a (100) surface of silicon-iron (Fe 3 wt% Si, sheet thickness 0.3 mm), imaged in the magneto-optical Kerr-(a), Voigt-(b) and Gradient-effect (c). The Kerr effect is linear in the magnetization vector, so the four domain phases in (a) show up in different colors. The same pattern imaged in the Voigt effect displays only two colors, one for each magnetization axis. This contrast is independent of the magnetization *direction* since the Voigt effect depends quadratically on the magnetization vector. The Gradient effect is sensitive to changes in magnetization. Therefore domain boundaries show up in this effect with a contrast depending on the relative magnetization directions of the neighboring domains. Both, Voigt and Gradient effect are strongest at perpendicular incidence of light and require a compensator for contrast adjustment.

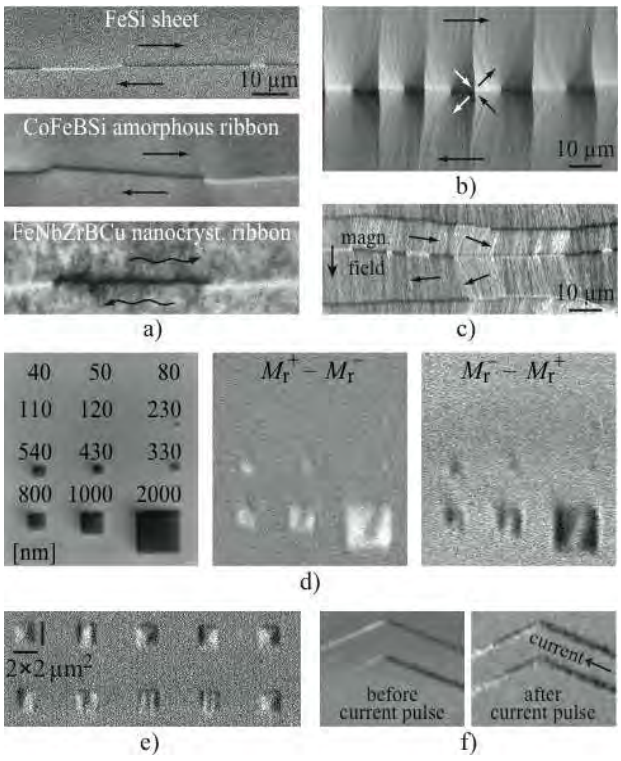

Fig. 10. High-resolution Kerr observations. (a) Domain wall imaging on different bulk samples. The surface wall width for the FeSi Goss sheet (300 nm thick) with (110) surface orientation is 150 nm, for the metallic glass (25 µm thick) it is 0.9 µm, and for the nanocrystalline ribbon (20 µm thick) a surface wall width of 1.6 µm is measured, as expected due to the decreasing anisotropy in the order of materials. The black-white contrast of the wall segments is caused by the rotation sense of magnetization (see also Figure 4a). (b) Cross-tie wall in a 40 nm thick Permalloy film, and (c) coexisting asymmetric Bloch- and Néelwalls in a 460 nm thick Permalloy film, the latter being characterized by a double-contrast. See ref. [1] for details. (d) Regular image (left) and difference images between the remanent states after positive and negative saturation (middle) and vice versa (right) on quadratic cobalt elements of various sizes. The saturation field was aligned vertically, indicated is the edge length of the elements in nanometer. (e) Domain patterns in an array of 2 µm wide Co elements after ac-demagnetization. In (f) the head-on domain walls in 500 nm wide NiFe stripes were shifted by current pulse injection. [(f) together with *J. McCord* and M. Kläui]

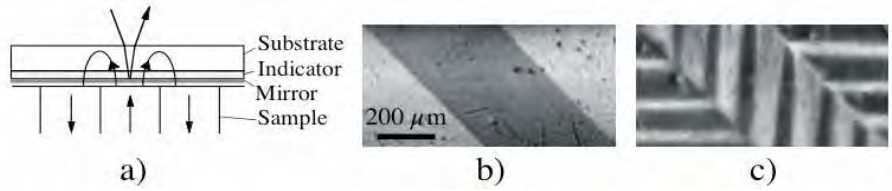

Fig. 11. (a) Schematics of the magneto-optical indicator film technique and application to a NiMnGa magnetic shape memory alloy: (b) structural contrast, showing two twin variants, (c) domain contrast, obtained by an indicator film on top of the surface [courtesy *Y. Lai and J. McCord*]

REFERENCES

1. A. Hubert and R. Schäfer: Magnetic Domains. The Analysis of Magnetic Microstructures. Springer Verlag, Berlin (1998)
2. R. Schäfer: *Investigation of domains and dynamics of domain walls by the magneto-optical Kerr effect*. In Handbook of Magnetism and Advanced Magnetic Materials. ed. by H. Kronmüller and S. Parkin, Wiley (2007)

STUDIA UNIVERSITATIS BABEŞ-BOLYAI, PHYSICA, LII, 1, 2007

COUPLING BETWEEN MICROMAGNETISM AND SPIN TRANSPORT

L.D. BUDA-PREJBEANU[1], D. GUSAKOVA[1,2], U. EBELS[1], A. VEYDYAV[1,2], J.-CH. TOUSSAINT[3]

The interaction between spin polarized current and magnetization is extensively studied by means of experimental and theoretical approaches. Up today the models used to describe the magnetization dynamic are based on the Landau-Lifshitz-Gilbert equation with an additional spin torque term proposed by Slonczewski [1]. Recently a macrospin approach was suggested [2] in which the spin-torque term is extract from transport diffusion equation. By this way structures with two or more magnetic coupled layers may be studied. Here we propose to generalize this approach by coupling full 3D micromagnetic computation and spin diffusion equation.

The possibility to induce, via spin momentum transfer, a steady state magnetization precession in the free layer of a spin valve structure, may serve to design RF oscillators [ ]. In this work we focus on spin current induced excitations for the perpendicular polarizer (POL)-planar free layer (FL) (Fig. 1). The detection of the magnetoresistive signal imposes the integration of a third magnetic layer with in-plane magnetization (AN). The sample POL-FL-AN is a circular cross-section nanopillar of 60nm of diameter. The presence of the AN layer can change the current polarization condition with respect to the case of bilayers POL-FL. In order to analyze the effect of this third magnetic layer the modified LLG equation is integrated:

$$\frac{\partial \mathbf{M}}{\partial t} = -\gamma_0 \left(\mathbf{M} \times \mathbf{H}_{\mathbf{eff}}\right) + \alpha\left(\mathbf{M} \times \frac{\partial \mathbf{M}}{\partial t}\right) + \left(\frac{\partial \mathbf{M}}{\partial t}\right)_{ST} \tag{1}$$

where different to [1] the spin torque term contains implicitly the cross product of magnetization M and spin-accumulation m vectors:

$$\left(\frac{\partial \mathbf{M}}{\partial t}\right)_{ST} = c\left(\mathbf{m} \times \mathbf{M}\right) \tag{2}$$

The prefactor is proportional to the injected current density and depends on the sample geometry and materials. From diffusion equation the spin-accumulation distribution is evaluated everywhere in the free layer.

[1] SPINTEC Laboratory CEA/CNRS URA2512, 17 Av Martyrs, 38054 Grenoble, France
[2] Moscow State University, Faculty of Physics, Moscow, 119992, Russia
[3] Institute Néel, CNRS-INPG-UJF, 25 rue des Martyrs, BP 166, 38042 Grenoble, France

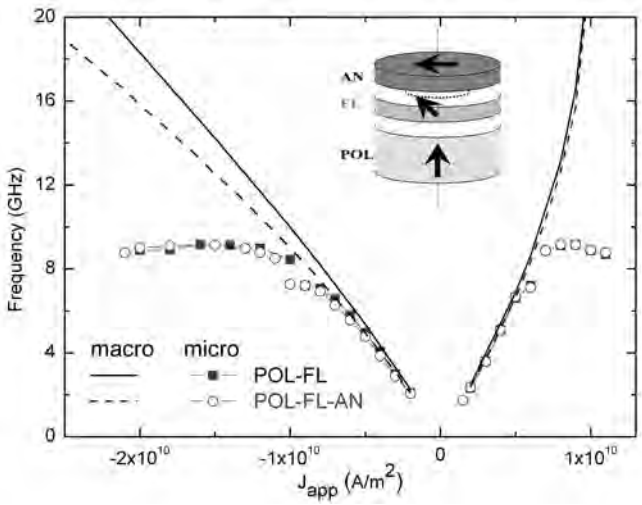

Fig. 1. Frequency versus injected current by macrospin and micromagnetic computation. The structure of the oscillator is presented in the inset.

In zero applied field when the injected current is large enough an out-of-plane precession is stabilized. The simulations reveal that in this case, the oscillation is controlled by the perpendicular polarizer POL and the role of the AN as planar polarizer is minor. Thus passing from a structure POL-FL to one POL-FL-AN, only smalls differences are noticed for the frequency dependence on the injected current (Fig1). Furthermore, experimentally, under in-plane externally applied field, an in-plane precession had been observed which in any case can not be explained only by the perpendicular polarizer POL By adding the spin torque term computed from transport equation this in-plane steady state is obtained also by modeling confirming qualitatively the experimental observations.

REFERENCES

1. J.C. Slonczewski, "Current-driven excitation of magnetic multilayers", J. Magn. Magn. Mater. 159, L1-L7 (1996)
2. D. Gusakova, A. Vedyayev, U. Ebels, 10th Joint MMM/INTERMAG Conference, January 7-11, p. 82, AW-11 (2007)
3. D. Houssameddine, et al. "Out of plane steady-state precession for the perpendicular polarizer free layer spin torque oscillator", Nature Materials **6,** 447-453 (2007)

STUDIA UNIVERSITATIS BABEŞ-BOLYAI, PHYSICA, LII, 1, 2007

NEW 3-D BULK SHAPED AND NANOCOMPOSITE MAGNETOSTRICTIVE MATERIALS

N. LUPU[1], H. CHIRIAC[1], M. VALEANU[2], T. BURUIANA[3], V. HARABAGIU[3], AND I. MIHALCA[4]

The fabrication of highly efficient integrated magnetostrictive sensors, actuators and transducers requires the availability of 3D-shaped magnetoelastic materials with high magnetostriction in low saturating fields. Up to now, Terfenol-D is the most used magnetostrictive material for magnetostrictive actuators and transducers, whereas magnetostrictive metallic glasses are preferred for sensors applications.
Very recently, 2 new alternatives appeared: Fe-(Ga,Al) alloys, as single crystals or melt-spun ribbons, and Ni-Mn-Al and Co-based magnetic shape memory alloys (MSMs).
This work focuses on design, preparation and characterization of novel 3-D shaped magnetostrictive materials either having new compositions or being for the first time prepared by conventional methods:

(i) 3-D shaped $Fe_{100-x}(Ga,Al)_x$ ($x = 13 \div 30$), $(Co,Ni)_2Mn(Ga,Al)$, $Fe_{70-x-y}Co_xSm_yB_{20}$ ($x = 10$; 20 and $y \leq 2.5$), and $Tb_{0.98}Fe_{1.96}B_{0.02}$ polycrystalline magnetostrictive alloys prepared by melt-spinning and mould casting techniques;

(ii) composite materials, consisting of nano- and micropowders of Fe(Ga,Al) $(Co,Ni)_2Mn(Ga,Al)$, (Fe,Co)-Sm-B and (Tb,Dy)-Fe-B) active magnetostrictive materials embedded into different resins and polymer matrices.

The main aim of these investigations was to understand the intrinsic mechanisms governing the magnetoelastic and magnetostrictive properties of these polycrystalline or composite materials without any distinct structural preferential direction.
The XRD patterns of Fe-(Ga,Al) as-quenched melt-spun ribbons and bulk shaped samples indicate the absence of any texture. In addition to the primary reflections at ~ 44^0 (110) and ~ 64^0 (200), none reflections corresponding to the DO_3 phase are observed. The thermomagnetic measurements confirm the existence of bcc Fe (A2 phase), with an additional magnetic transition around 500^0C for $Fe_{79}Ga_{21}$ melt-spun ribbons.

[1] National Institute of Research and Development for Technical Physics, Iasi, Romania
[2] National Institute of Materials Physics, Bucharest-Magurele, Romania
[3] "Petru Poni" Institute of Macromolecular Chemistry, Iasi, Romania
[4] Condensed Matter Research Institute, Timisoara, Romania

The saturation magnetization decreases from 180 emu/g to 100 emu/g, when the Al content increases from 17 to 30 at. %, respectively. The same behavior was observed for Fe-Ga samples, when the Ga content increases. The "hybrid" samples (containing both Ga and Al) exhibit average values for the magnetization of 150 emu/g. The magnetic permeability is following the same descendent trend with the increase of the non-ferromagnetic elements content, reaching a maximum of 1400 at 80 Hz, for 8 at. % Ga or Al.

The magnetostriction of Fe-(Ga,Al) magnetostrictive materials ranges between 30 and 100 ppm (Fig. 1), depending on samples composition (is higher for Fe-Al binary alloys) and the as-cast or annealed ($800 \div 1100^0$C) state of the measured sample (the magnetostriction increases slightly after annealing). Additionally, the magnetostriction measured for a single plate is changing the sign from positive to negative when the Al content increases from 0 to 30 at. %, passing through 0 for 10 at. % Al. The variation with the external field is of 10÷20 % when the applied field increases from 0.15 to 0.8 T.

But the most spectacular variation appears to be when 2 to 5 thin plates are stacked together, i.e. an increase of 1.5÷2 times compared with the magnetostriction of a thin plate, as shown in Fig. 2. The saturation induction of the samples varies between 0.9 and 1.7 T depending on the Al and Ga content.

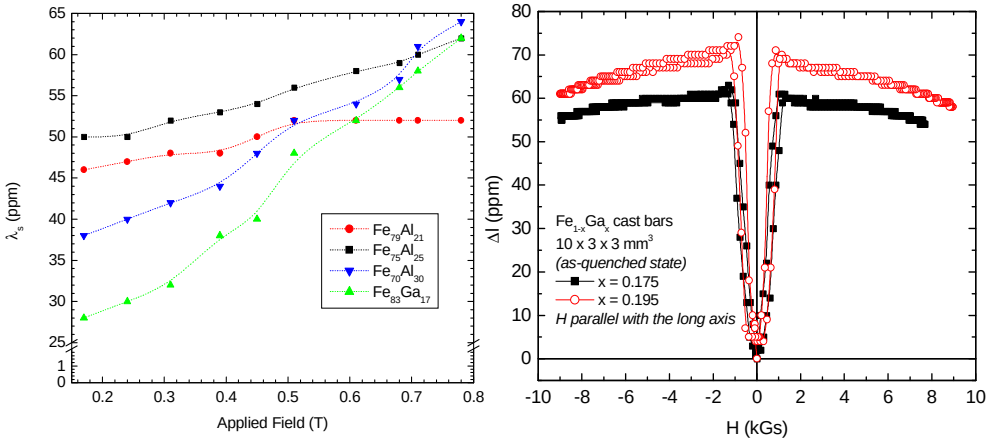

Fig. 1. Magnetostriction versus applied magnetic field for Fe-Ga and Fe-Al thin plates (12*6*0.5 mm^3) and cast bars (10*3*3 mm^3).

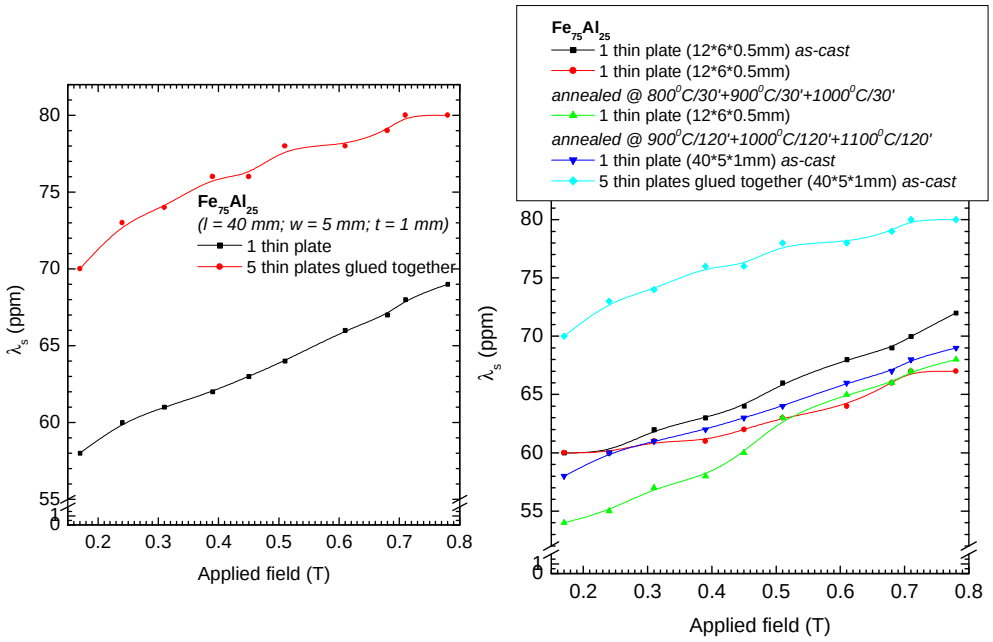

Fig. 2. Magnetostriction as a function of the number of thin plates measured at once.

Thus, the most of the Fe-(Ga,Al) samples are magnetically very soft, which is also confirmed by the λ-H measurements which indicated values of 60 and respectively 75 ppm for saturation magnetostriction constant of $Fe_{82.5}Ga_{17.5}$ and $Fe_{80.5}Ga_{19.5}$ cast bars of 3 x 3 x 10 mm^3, in the as-cast state. The magnetostriction constant increases up to 100 ppm after annealing the samples at 1000^0C for 72 h, followed by slow cooling to room temperature. No difference in the λ_s constant was observed after the annealing at 1000^0C for 72 h, slow cooling up to 800^0C, followed by rapid quenching to RT. Additionally, the value of λ_s increases gradually to 160÷180 ppm, depending on composition (the maximum value is smaller for higher contents of Ga), when applying an external compressive stress of 3÷5 MPa. Over this compressive stress value, the strain remains constant.

The magnetostriction of RE-based 3-D shaped bulk samples is larger compared with Fe-(Ga,Al) magnetostrictive polycrystalline materials, ranging between 50 and 350 ppm, depending on samples composition and shape (see Fig. 3).

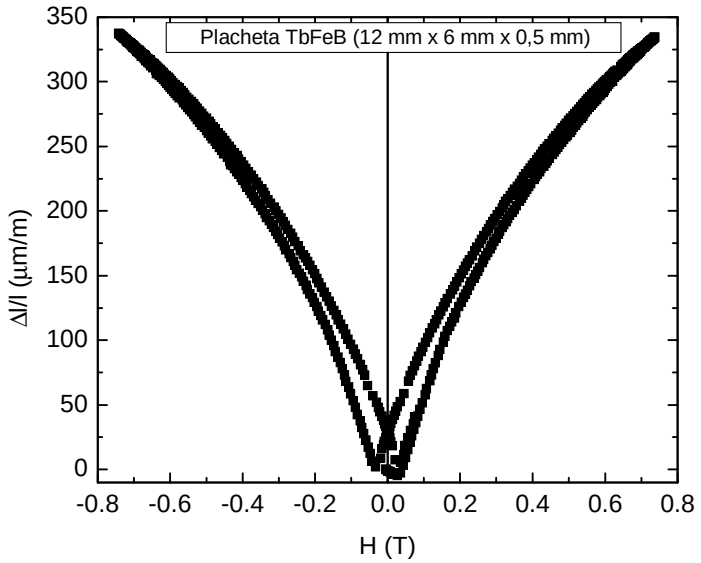

Magnetostriction vs. applied field for the TbFeB thin plate.

$Fe_{100-x}Ga_x$ (x = 17÷20) and $Fe_{100-x}Al_x$ (x = 20÷24) nanopowders (between 200 and 500 nm in diameter) have been prepared by arc-discharge method, then embedded in Poxipol® commercial resin (resistant to water, outdoor conditions and many corrosive agents), CTM polymer, electrostrictive polymers and polyurethane. Different concentrations (10 ÷ 30 wt. %) of metallic nanopowders have been embedded into the resin layer (t = 3 ÷ 5 mm). The magnetostriction of the composite layers with Poxipol® resin was found to vary between -20 ppm and +40 ppm, depending on Al and Ga content. When using CTM polymers as matrix the magnetostriction reaches -50 ppm, whilst for polyurethane in increases to -80 ppm for a composite with 20 wt. % $Fe_{80}Al_{20}$. All these aspects are still in progress now and will be reported lately.

Ni_2MnGa, Co_2NiGa and $Co_{38}Ni_{33}Al_{29}$ melt-spun ribbons of 25 μm thickness and 3 to 5 mm width, and cast thin plates of 12*6*0.5 mm^3 have been prepared. The magnetic behavior of all cast thin plates is not sensitive to the direction of the applied field, whereas the magnetostriction, which varies between +15 ppm and 50 ppm, strongly depends on the direction of the applied field, despite the fact that SEM images do not show any preferential direction of the grains. The magnetostrictive response is different for ribbons compared with the bulk plates. This might be the result of the different microstructure existent in melt-spun

ribbons (the grains are oriented perpendicular on the ribbons long axis) compared with the bulk shaped samples. For example, when H is parallel with the ribbons long axis λ_s ~ +50 ppm, decreases to +25 ppm when H is perpendicular on the ribbons long axis, and reaches a maximum of + 200 ppm when H is perpendicular on the ribbons plane, i.e. parallel with the direction of the grains. If one compares a thin plate of 0.5 mm thickness with 20 ribbons stacked together and having more or less the same total thickness, λ_s increases from +18ppm for the thin plate to +30 ppm for ribbons "package" having the nominal composition $Co_{38}Ni_{33}Al_{29}$.

Thus, to conclude, one can say that despite the moderate value of the λ_s constant, the magnetic softness of the studied materials and their mechanical hardness compared with Terfenol-D materials indicate them for different engineering applications. There are also other important facts which have to be considered for applications: the samples are not single crystals; they are prepared by conventional continuous casting methods (efficient and low cost); they are not fragile and brittle, and the magnetoelastic properties could still be improved by choosing the optimum composition and treatments. All these aspects will be discussed in detail with respect to the materials microstructure and macroscopic magnetic behavior, but considering also the advantages of using such materials in integrated hybrid sensors and actuators.

N. Lupu and H. Chiriac wish to acknowledge the financial support from the MESEMA project, funded under the 6th Framework Programme of the European Community (Contract N° AST3-CT-2003-502915). This work was partly done within the MAGSAT Project, funded under CEEX Programme of the Romanian Ministry of Education and Research – National Authority for Scientific Research (Contract N° 34/2005).

STUDIA UNIVERSITATIS BABEŞ-BOLYAI, PHYSICA, LII, 1, 2007

STM AND SPECTROSCOPY OF NANOSIZED FERROMAGNETIC STRUCTURES

GUILLEMIN RODARY*

After an introduction to the scanning tunneling microscopy (STM) and spectroscopy (STS) techniques, we will explain their application to magnetic nanostructures. The constant current mode allows a complete characterization of nanostructures up to atomic resolution. The growth mode of nanostructures, e.g. by self-organization can be studied with atomic resolution. Simultaneously to this topography acquisition, the spectroscopic mode draws a map of the electronic local density of states of the sample surface. We are thus sensible to localized or delocalized surface states that also give rise to electronic standing waves, as imaged by STS. Point mode spectroscopy is also sensitive to structural properties like the stacking sequence of atomic layers within a nanostructure.

To obtain local magnetic information of nanostructures, one powerful technique is nowadays the spin-polarized STM (SP-STM). By using a magnetic tip the STM is sensitive to the relative orientation between sample and tip magnetization, which leads to magnetic contrast. It is possible to image nanoscale magnetic domain wall with atomic resolution, spin structures at surface at an atomic level or to study the magnetic properties of a single atom. As an example we choose the system of Co nanoislands deposited on a Cu(111) surface. We will show that the SP-STM in magnetic field allows to measure an hysteresis loop of a single nanostructure. We determine the switching field and magnetic anisotropy of a well defined, single nanostructure. We also show that spin electronics studies, such as the tunnel magnetoresistance, can be investigated on single nanostructures.

* Matériaux et Phénomènes Quantiques,Unité Associée au CNRS et Universités Paris VI et Paris VII